

Modelling Semiconductor Pixel Detectors

Keith Mathieson



UNIVERSITY
of
GLASGOW

Department of Physics and Astronomy

*Thesis submitted for the degree of Doctor of Philosophy in the
subject of physics*

August 7, 2001

©K. Mathieson August 7, 2001



ProQuest Number: 13818891

All rights reserved

INFORMATION TO ALL USERS

The quality of this reproduction is dependent upon the quality of the copy submitted.

In the unlikely event that the author did not send a complete manuscript and there are missing pages, these will be noted. Also, if material had to be removed, a note will indicate the deletion.



ProQuest 13818891

Published by ProQuest LLC (2018). Copyright of the Dissertation is held by the Author.

All rights reserved.

This work is protected against unauthorized copying under Title 17, United States Code
Microform Edition © ProQuest LLC.

ProQuest LLC.
789 East Eisenhower Parkway
P.O. Box 1346
Ann Arbor, MI 48106 – 1346

GLASGOW
UNIVERSITY
LIBRARY:

12401

COPY 1

To my family.

Abstract

In this thesis the work will focus on the modelling of highly pixellated solid-state devices. Results are presented on the performance of a pixellated spectroscopic silicon detector - the Dash-E detector. The electronic noise is measured to be 228 eV with the system observed to be close to the Fano limit at room temperature. The characteristic X-rays of Mn-55, Cu, Rb, Mo, Ag and Ba have been used to examine the spectroscopic performance of the detectors. Good linearity over the required energy range 1 keV to 25 keV has been observed. A higher than expected background is evident in all of the spectra taken - approximately a 1:1 correspondence in the peak counts to background counts.

The modelled performance of a 3-D GaAs detector is analysed. The effect of the metallic column-like electrode structure on the particle interactions is simulated via the Monte Carlo code MCNP. The effective dead area due to these electrodes is reduced from 8 % to 4.5 % due to the secondary particle interactions. The modelled structure becomes depleted at 50 V with a slight over-depletion of 75 V necessary to minimise the inter-electrode low field regions. The principle benefit of these depletion voltages is that they remain constant for whatever detection thickness that fabrication allows. The charge transport in the devices are also examined, with the damage effects

of dry-etching included - a technique used to form the electrode holes in the GaAs material. Full charge collection can be expected after 200 ps in most cases. The effect of reducing the charge carrier lifetime and examining the charge collection efficiency has been utilised to explore how these detectors would respond in a harsh radiation environment. It is predicted that over critical carrier lifetimes (10 ps to 0.1 ns) an improvement of 40 % over conventional detectors can be expected. This also has positive implications for fabricating detectors, in this geometry, from materials which might otherwise be considered substandard.

An analysis of charge transport in CdZnTe pixel detectors has been performed. The analysis starts with simulation studies into the formation of contacts and their influence on the internal electric field of planar detectors. The models include a number of well known defect states and these are balanced to give an agreement with a typical experimental I-V curve. The charge transport study extends to the development of a method for studying the effect of charge sharing in highly pixellated detectors. The case of X-ray, as well as higher energy γ -ray, interactions are considered. The charge lost is studied for these interactions over a range of pixel sizes ($1\mu\text{m}$ to 10 mm). The aforementioned Dash-E detector has been used to obtain experimental data for comparison with the models developed, with close agreement being observed. The combination of MCNP and MEDICI is used to form a complete picture of photon interactions in semiconducting materials and also compares well with experiment. The models predict that the dominant term in the sharing of charge is due to diffusion and that the difference with photon energy is due to the energy given to the photoelectron.

Acknowledgements

I would firstly like to thank my supervisor, Professor Ken Smith. His help and guidance over the last few years has been invaluable. The assistance of Professor David Saxon, our head of group and department, is also appreciated.

Mahfuzur Rahman, my back-up supervisor, deserves a big thanks. His willingness to read and re-read some of these chapters is much appreciated. I'd also like to acknowledge the late Colin Raine who helped out at the beginning of my PhD. Thanks also to Val "have you finished yet?" O'Shea his constant pestering kept me going during the writing-up stage (even if I didn't use Word). Richard Bates and Spyros Manolopoulos were a great help during the 3 years of my PhD, my thanks to them. I couldn't have asked for better folk to share an office with than John Watt and Craig Whitehill, much appreciated lads.

Fred Doherty, Drew Meikle, John Melone, Pamela Thornton, Stephen Bryce, Derek Livingstone and the late Frank McDevitt all helped with their technical expertise over the years. Fred, Drew and John also provided much entertainment on the football front.

I'd also like to thank Steven Passmore who was always willing to discuss (argue) any problems I had. His help is very much appreciated. Thanks also

to his room mates Steven Devine and Patrick Roy for much amusement over the years.

My CASE sponsors BNFL helped support these studies and for that I'm very grateful, especially to Brian More and Karl Hughes who supervised me at BNFL. Paul Seller of the Rutherford Appleton Laboratories was also a great help, not only by building excellent pixel detectors but by patiently explaining everything about how they worked.

Professor Asen Asenov and Dr. Scott Roy of the device modelling group at the department of electronics and electrical engineering helped enormously throughout my PhD. Their assistance in allowing access to modelling codes and explaining the intricacies of device modelling was invaluable.

Thanks to Catherine MacIntyre for helping with all the travel arrangements, admin. and many other things.

My new office mates, Julien Marchal and David Davidson, deserve a couple of beers for putting up with me while I was writing up, I'll pay up one of these days. Also cheers to Liam for helping out when I was finishing this thing off.

Cheers to all the guys from undergraduate days - Dave P, Steve Hamill, Flisch, DC, Santa etc. Thanks also to all of my flat mates over the years Dave, Hillbill, Gary, Bruce, Henry, John K. Steve and Elaine, Tim and Neil. To all the lads up in Inverness - Colin, Jack, Jim, and Ian - thanks for all the good nights out.

I'd also like to thank all of my family - Mum, Ryan, Stuart, Siobhan and not forgetting Gran - for everything over the years. Biggest thanks of all to my late father who convinced me that this was all worthwhile.

Lastly thanks to Tracey for putting up with me.

Declaration

Except where explicit reference is made to the work of others, this dissertation is the result of my own work. None of this material has been submitted for any other degree at the University of Glasgow or any other institution.

Keith Mathieson

Contents

1	Introduction	33
2	Semiconductor physics	43
2.1	Introduction	43
2.2	Crystal structure	44
2.3	Energy bands	45
2.3.1	Effective Mass	49
2.4	Intrinsic and Extrinsic Semiconductors	49
2.4.1	Extrinsic Semiconductors	51
2.5	Carrier Transport in Semiconductors	55
2.5.1	Drift	56
2.5.2	Diffusion	57
2.5.3	Current Density Equations	58
2.6	Carrier Generation and Recombination in Semiconductors . .	61
2.6.1	Thermal Generation of Charge Carriers	61
2.6.2	Generation of Charge Carriers by Electromagnetic Ra- diation	62
2.6.3	Multiplication Processes	63
2.6.4	Recombination	64
		15

2.7	Carrier Transport with Generation and Recombination	70
3	Particle Interactions and Detection Techniques	73
3.1	Introduction	73
3.2	Particle Interactions in a semiconducting material	74
3.2.1	The interaction of X and γ rays	75
3.2.2	Electron interactions	80
3.2.3	Charge particle interactions	82
3.3	Detectors	84
3.3.1	Integrating detectors	85
3.3.2	Individual quantum pulse mode	86
3.3.3	Metal semiconductor contacts	87
3.3.4	Photoconductive detectors	90
3.3.5	Diode detectors	91
3.3.6	Materials	95
3.3.7	Aspects of charge transport	100
3.3.8	Position sensitive semiconductor detectors	104
4	The detector systems - ERD1 and Dash-E	107
4.1	Introduction	107
4.2	Description of devices	108
4.2.1	The detector	109
4.2.2	Bump bonding	109
4.2.3	The read-out electronics	110
4.3	Detector Characteristics	113
4.3.1	Linearity of Response	113

CONTENTS

- 4.3.2 Energy resolution 114
- 4.4 The Dash-E detector 117
 - 4.4.1 Energy Resolution 118
 - 4.4.2 Background Continuum 122
- 4.5 Discussion 123
- 5 Comparison of experimental and simulated results 125**
 - 5.1 Introduction 125
 - 5.2 Comparison of MCNP and experiment 126
 - 5.3 Comparison of MEDICI models 129
 - 5.3.1 Experimental work 130
 - 5.3.2 Modelling charge sharing with MEDICI 133
 - 5.3.3 Comparing experiment with simulation 136
 - 5.3.4 Predictions 138
 - 5.4 Discussion 142
- 6 3-D detector simulations 145**
 - 6.1 Introduction 145
 - 6.2 Motivation 146
 - 6.3 Detector Characteristics 148
 - 6.3.1 Monte Carlo simulation 149
 - 6.4 Electrical Simulation 150
 - 6.5 Charge transport and signal formation in 3-D detectors 153
 - 6.5.1 Charge transport in the low field region 157
 - 6.6 Etch induced sidewall damage 160
 - 6.7 Charge collection efficiencies (CCEs) 163

6.8	Discussion	165
7	Cadmium Zinc Telluride	167
7.1	Introduction	167
7.2	Background	168
7.3	Material Simulations	169
7.3.1	Defects and trapping centres	170
7.3.2	Experimental Comparison	172
7.4	Charge transport	175
7.4.1	Signal generation	175
7.4.2	Charge sharing	183
7.5	Summary	194
8	Conclusions and summary	197
A	Numerical Modelling	201
A.1	The Monte-Carlo method	201
A.2	Finite element modelling	202
B	Semiconductor parameters	203
C	Source information	205
D	Simulating electrical transport in dry-etched III-V devices	209
D.1	Introduction	209
D.2	Sidewall damage in III-V structures	210
D.2.1	Model details	212
D.2.2	Damage Profile	213

CONTENTS

D.3 Gate recessing in HEMTs 216

 D.3.1 Modelled structure 216

 D.3.2 Damage Profile 217

 D.3.3 Damage effects on gate characteristics 218

 D.3.4 Temporal response of HEMT 218

D.4 Discussion 220

E Trapping and de-trapping in MEDICI 223

 E.0.1 Model 223

 E.0.2 Trapping and de-trapping 223

List of Figures

- 1.1 Alpha particle tracks from Wilson’s cloud chamber and a re-
construction of a Z boson decay from the ALEPH detector at
CERN. 34
- 2.1 The diamond and zinc blende lattice structures respectively
(After Sze 1985, p. 5 Fig. 3). 45
- 2.2 The formation of energy bands (After Harrison 1980). 46
- 2.3 The energy levels of silicon atoms in a diamond structure (Af-
ter Sze 1985, p. 10 Fig. 8). 47
- 2.4 The band structure of insulators, semiconductors and metals
(After Sze 1985, p. 11 Fig. 9) 48
- 2.5 The intrinsic semiconductor : (a) the band structure, (b) den-
sity of states, (c) occupation probability and (d) the elec-
tron/hole densities (After Sze 1985, p.18 Fig. 15). 51
- 2.6 Arsenic as a n-type dopant in silicon (After Schockley 1950,
p. 13 Fig. 1-7) 52
- 2.7 Boron as a p-type dopant in silicon (After Schockley 1950, p.
14 Fig. 1-8) 54

LIST OF FIGURES

2.8 Energy band diagrams for extrinsic semiconductors, n-type and p-type respectively 55

2.9 Current conduction in a uniformly doped semiconductor (After Sze 1985, p. 36, Fig. 5) 59

2.10 Generation of electron and holes due to the absorption of electromagnetic radiation. The three cases of $E_{\text{photon}}=E_g$, $E_{\text{photon}} > E_g$ and $E_{\text{photon}} < E_g$ are shown (After Lutz 1999, p.22, Fig 2.13). . 63

2.11 Indirect generation - recombination processes at thermal equilibrium (Adapted from Sze 1985, p. 49 Fig. 13). 67

2.12 Carrier flow with generation and recombination (After Lutz 1999, p.35 Fig. 2.20). 71

3.1 The dominant processes for photon interactions (After Knoll 1989, p. 54, Fig. 2-20). 76

3.2 Schematic showing an X-ray interaction and the subsequent processes. 77

3.3 The angular dependence of photoelectrons for soft and hard X-rays. The circular shapes indicate the probability of photoelectron emission at that angle (After Compton and Allison 1949, p. 576, Fig. VII-25). 78

3.4 The Compton scattering effect. 80

3.5 Electron ranges in silicon, gallium arsenide and cadmium zinc telluride. Calculated using the ESTAR database (available from <http://physics.nist.gov/PhysRefData/>). 81

3.6 The Bragg curve for an alpha particle of several MeV initial energy (After Knoll 1989, p.33, Fig. 2-2). 84

LIST OF FIGURES

3.7 The metal semiconductor junction 88

3.8 The properties of a diode detector in equilibrium. 94

3.9 The absorption efficiencies of Si, GaAs and CdZnTe for com-
mon detector thicknesses. 96

3.10 Polarisation of the atoms of a dielectric by a pair of equal
positive charges (After Ramo, Whinnery, Van Duzer 1994, p.
7 Fig. 1.3c). 103

4.1 Photograph of the Energy Resolving Detector 1 with detector
and read-out highlighted. 108

4.2 The preamplifier array chip (PAC5). The readout chain (left)
is bump bonded to each individual pixel. 111

4.3 The secondary readout chain (SHAMROC) contains 128 chan-
nels. Two are wire bonded to each PAC5 chip. 112

4.4 Linearity plots for ERD1 Detector 114

4.5 A spectrum from the ERD1 detector with the corresponding
image 115

4.6 The variation of FWHM^2 with incident X-ray energy. The
noise of the system is dominated by the electronic contribution. 116

4.7 The Dash-E response to the characteristic X-rays of Mn-55,
Cu, Rb, Mo, Ag and Ba. 118

4.8 The variation of FWHM with incident X-ray energy. A Fano
factor of 0.23 is required if no other effects contribute. 120

4.9 The variation of FWHM with incident X-ray energy. A Fano
factor of 0.12 is assumed. 121

LIST OF FIGURES

4.10	The peak to background ratio for the 4 highest energy sources Rb, Mo, Ag and Ba.	123
5.1	MCNP geometry of the Dash-E detector.	126
5.2	A comparison of a Barium spectrum from a modelled Dash-E detector and the experimental output.	129
5.3	The charge shared data from the Mo dataset, showing the raw data and the spectrum adjusted for charge sharing (clustered). The raw data corresponds to data in which a charge shared event has occurred but no correction has been performed. The clustered data is the same data but this time the charge shar- ing correction has been included.	132
5.4	Charge shared as a function of threshold energy for the Dash-E detector	133
5.5	The modelled detector - the charge density should be below that where plasma effects are evident. The modelled width should be sufficiently wide so that no charge is reflected at the Neumann boundaries.	135
5.6	The normalised charge distributions for each source after trans- port through modelled Dash-E detector.	136
5.7	Illustration of method for the calculation of charge sharing . .	138
5.8	Comparison of simulated and experimental results of charge sharing, as a function of energy threshold, for the Dash-E de- tector.	139

LIST OF FIGURES

- 5.9 The amount of charge shared in a 300 μm thick Si detector, 80 V reverse bias, with 300 μm square pixels, neglecting the diffusion process. 140
- 5.10 New imaging detectors plan to use 55 μm square pixels on 300 μm thick silicon. The models indicate a substantial amount of charge will be shared with neighbouring pixels. 143
- 5.11 The dependence of charge sharing on pixel size for a 300 μm thick silicon detector operated at 80 V. 144
- 6.1 Pixel detectors with co-axial electrode structure. Left the unit cell and right the simulated cross section from MEDICI. The heavily shaded circular electrodes are held at a different potential than the lightly shaded electrodes. Points A and B are charge generation points discussed later in the text. 148
- 6.2 Point source of 60 keV photons scanned from electrode to electrode in 1 μm steps. The circular point is the energy deposited in the detection medium when a 5 μm radius electrode is uniformly illuminated. All data are normalised to the average energy deposited in 200 μm GaAs for 60 keV photons. 151
- 6.3 The simulated depletion regions in steps of 10 V, from 0 V to 40 V. Full depletion can be seen to occur at 50 V. 153
- 6.4 Potential profiles for 50 V and 75 V respectively. The low E-field can be seen in the inter-electrode region. 154

LIST OF FIGURES

6.5	The modelled I-V characteristics for the 3-D detector structure. The reversed bias leakage current is approximately 1 nA per pixel and the device breaks down after an applied voltage of 230 V.	155
6.6	The total current pulse split into its 3 component parts. . . .	156
6.7	The total charge pulse split into its 3 component parts. . . .	157
6.8	Comparison between charge pulses for the generation points A and B seen in figure 6.1.	158
6.9	Contour plots of electron concentration for two different applied biases. For the 50 V bias case some charge can be seen to be trapped in the inter-electrode space. At an increased bias (75 V) the electrons can be seen to drift to their collection electrode and be fully collected within 31 ps.	159
6.10	Distribution of defects caused by etching process.	161
6.11	Comparison of charge pulses with (dashed line) and without (solid line) sidewall damage.	162
6.12	Comparison of charge collection efficiencies, as a function of charge carrier lifetime, in 3D detectors and a planar structure.	164
7.1	Comparison of experimental and simulated current-voltage characteristics with different contacts and the trap concentrations of table 7.2.	173
7.2	Electric field profiles for the two simulated contact conditions.	174
7.3	The simulated potential profiles for the two contact cases . . .	175

LIST OF FIGURES

7.4 Positions of charge generation. Point A is 3 μm from the cathode, point B is exactly in the centre of the detector and point C is 3 μm from the anode. 177

7.5 The total current and charge pulses, for both contacts, split into their component parts. Here the charge is generated 3 μm from the cathode. 178

7.6 The total current and charge pulses, for both contacts, split into their component parts. Here the charge is generated in the middle of the detector. 180

7.7 The total current and charge pulses, for both contacts, split into their component parts. Here the charge is generated 3 μm from the anode. 182

7.8 Schematic representation of method for determining the distribution of a charge cloud at the anode contact. 184

7.9 The Gaussian distributions for the Schottky contact case. Three thicknesses of detector are shown. 185

7.10 The sigma of the Gaussian distributions for the different charge generation points (see figure 7.4) and electric field conditions (see figure 7.2). The single line (denoted Model) corresponds to the variation of the sigma given by equation 7.1. 186

7.11 The radial distribution, after charge transport, rotated around the charge generation point. 188

7.12 Integration of charge response over pixel width and length for a square pixel of 500 μm side. 189

LIST OF FIGURES

7.13	The charge collected at ohmic pixels as a function of the pixel size, for soft X-rays on CdZnTe.	190
7.14	The charge collected at Schottky pixels as a function of the pixel size, for soft X-rays on CdZnTe.	191
7.15	The averaged response of 2 million 662 keV photons in 2mm CdZnTe, from MCNP simulation.	192
7.16	Radial distributions for the charge cloud generated by the γ -ray interaction before and after charge transport, for the case of ohmic contacts.	193
7.17	The charge collected at a pixel as a function of the pixel size, for 662 keV photons on 2 mm thick CdZnTe.	194
7.18	The charge collected as a function of detector thickness for the various cases considered (square pixels, pitch is fixed at 100 μm). The term X-ray in the legend corresponds to the generation of 1000 e-h pairs in a volume of 1 μm^3 near the collecting electrode.	195
D.1	Modelled 2DEG structure, highlighting the important aspects of the structure.	212
D.2	The electron concentration over a section of the modelled 2DEG. The 2DEG can be seen to be depleted away from the etched surface.	214

LIST OF FIGURES

D.3 The trap density as a function of distance from the etched sidewall. The solid curve shows the effect of channelling on the defect profile as a function of distance from the etched sidewall. The light grey shading indicates the filled traps. The dashed curve shows the reduced trap density when channelling effects are neglected. The darker grey shading indicates the filled traps for this no channelling distribution. The inset shows how the depletion distance of the 2DEG from the sidewall for both cases. 215

D.4 The modelled HEMT structure. 217

D.5 Modelled gate characteristics of the HEMT illustrating the effect of dry-etch damage. 219

D.6 The time response of the drain current after the drain voltage is pulsed with 0.5 V, for varying etch times. All etch curves lie on top of one another indicating no change in temporal response as a function of etch time. 220

E.1 Time evolution of electron clouds 225

LIST OF FIGURES

List of Tables

- 5.1 Source definition data for barium 127
- 5.2 A breakdown of charge sharing effects for the Dash-E detector
for the case of no threshold. 141
- 6.1 The material parameters, with references, used in the simula-
tion packages MEDICI and MCNP to model GaAs. 152
- 7.1 The material values used to model CdZnTe. 170
- 7.2 Defect levels incorporated into simulations. 172
- B.1 Semiconductor parameters for Si, GaAs and CdZnTe 203
- C.1 Source definition data for Mn 205
- C.2 Source definition data for Cu 206
- C.3 Source definition data for Rb 206
- C.4 Source definition data for Mo 207
- C.5 Source definition data for Ag 207
- C.6 Source definition data for Ba 208

LIST OF TABLES

Chapter 1

Introduction

Many detector technologies have their roots in particle physics, due to the constant need for higher performance detectors. One of the first particle tracking detectors to be built was the cloud chamber, for which C. T. R. Wilson recieved the Nobel prize in 1927. He used a supersaturated volume of air which would form droplets of water in the presence of an electric charge, in order to study the particle tracks from alpha, beta and X-rays.

Nowadays, investigations into the fundamental nature of particles and their interactions require international collaborations of physicists and engineers to build and operate the huge detectors, such as the CERN experiments in Geneva, the Fermilab facility in Chicago and the Super Kamiokande collider in Japan.

Figure 1.1 shows alpha particle tracks from a model of Wilson's cloud chamber next to an event reconstruction of a Z^0 boson decaying to an electron positron pair ¹. These two figures illustrate how far the technology has developed in the intervening years.

¹Taken from <http://alephwww.cern.ch/DALI>



Figure 1.1: Alpha particle tracks from Wilson's cloud chamber and a reconstruction of a Z boson decay from the ALEPH detector at CERN.

Particle physics experiments have proved over the years to be an important driving force in the development of detector technologies, many of which have been commercialised and found application in other areas of science and medicine [1]. In 1974-1977, the discovery of charm particles, beauty/bottom particles and tau leptons (with lifetimes of 10^{-13} - 10^{-12} s) necessitated the move for precision particle detectors [2]. The detectors would require micron-level resolution, be placed close to the interaction point and have a small amount of detection material to minimise multiple scattering, which may affect the outer detectors. Silicon diode detectors were chosen to fulfil this role. Silicon and germanium detectors have existed as radiation detectors for over 50 years now [3].

Advances in other areas have also led to improvements in detection techniques, perhaps the most important being the explosion in the electronics industry over the past three decades. This has seen the fabrication of integrated circuits, which are custom designed for detector read-out. These ASICs (*Application Specific Integrated Circuits*) have allowed smaller de-

tection elements required for imaging, higher rates for application in particle physics experiments and lower electronic noise, which has benefits across a wide range of applications.

The challenges which face semiconductor pixel detectors vary from application to application and quite often contradict one another. Particle physics experiments, for example, require a thin detection layer to minimise the multiple scattering of the particles as they pass through to the outer detectors, while spectroscopic detectors need thick layers to ensure a high interaction probability over a range of incident particle energy. The requirements for semiconductor pixel detectors may be split into two categories; detection material, and readout electronics.

The detector material would ideally have good charge collection properties, be able to operate at room temperature and give a large signal for a small amount of energy deposited in the crystal. Good uniformity of response to radiation over a large area is a condition which at the moment is only satisfied by silicon and germanium detectors and is necessary for many applications. The need for high atomic numbered semiconductors (in comparison to silicon) to extend the useful range for the interaction of high energy gamma rays is also apparent. The detection material should be able to survive in a harsh radiation environment, a requirement almost specific to particle physics, such as that created at the particle colliders mentioned previously.

A high readout rate, increased pixel functionality, low electronic noise, a large dynamic range, good yield, uniformity between electronic channels and a high tolerance to radiation are just some of the requirements for the electronic readout of pixel detectors. Many of these have been solved by the

move to sub-micron fabrication techniques. The smaller component size permits a reduction of pixel size or an increase in the number of components per pixel - sometimes both. The devices exhibit greater radiation tolerance though pixel uniformity remains an issue.

In terms of imaging applications, devices require a large (sometimes 100 cm^2) spatially resolving array with small pixel sizes ($\sim 50\mu\text{m}$ pitch). Pixel arrays have been fabricated with $38\text{ }\mu\text{m}$ cells [4], which satisfy many of the criteria discussed above, though not on the scales useful as a large area imager. Detectors such as the LAD1 [5] tile the readout chips in order to increase the size of the imaging plane. This approach, though costly, offers an immediate solution.

The problem of radiation hardness is being addressed by efforts such as the ROSE collaboration [6], where semiconductor defect engineering is expected to extend the useful lifetime of silicon detectors. Material purity is also being improved upon not only by research groups [7], but also commercial suppliers [69].

There currently exists a wide variety of semiconductor pixel detectors, the most common being the *Charge Coupled Device* (CCD), due to its applicability in commercial products. These have found use as particle detectors [9], space borne spectroscopic imagers [10] and in video cameras, as well as many other applications. Other types include hybrid pixel sensors and monolithic pixel detectors. The hybrid pixel detector [11] offers high rate electronics, which are developed separately from the detection material and coupled at a later stage. This means the electronics may be made using standard CMOS fabrication techniques, a big advantage in improving yield

and reducing cost. Unfortunately, the interconnect stage is not yet a reliable process.

The continued move to improve spatial resolution has naturally led to smaller pixel elements. This can result in a new set of problems. As pixel size is reduced it becomes increasingly likely that charge generated under one pixel will be shared with the neighbouring pixels. For particle physics applications this is sometimes desired, since fitting to a cluster of ‘hit’ pixels can improve the accuracy of the position resolution. However, in spectroscopy this sharing of charge degrades the quality of the obtainable spectra. Medical imaging devices also suffer since more incident particles can be rejected if too much charge is shared. This could lead to an increase in the radiation dose to a patient, something which is clearly not desirable.

The first step in approaching these problems is often through computer modelling, where the electronics industry has developed advanced software packages to accurately model devices under development. These simulation packages are ideally suited to modelling semiconductor detectors, though much of the previous work in this field uses non-commercial software [12], [13] and [14]. One of the current limitations of detector modelling is forming a complete picture of the particle interaction and the subsequent transport of charge. Often, only one of these physical processes is performed. The fact that particle interactions are a statistical process means that many particles have to be simulated, and for each of the interactions a device simulation would have to be carried out. This leads to a prohibitive amount of computing time and so other approaches have to be considered. Here an attempt has been made to solve this problem by partially combining a Monte-Carlo

particle transport code with a finite element electrical device simulator.

This thesis concentrates on the detection of X-rays by semiconductor pixel detectors and addresses some of the limitations, through modelling, listed above. Chapter 2 outlines some of the fundamental semiconductor physics contained in one of the modelling packages, namely MEDICI [15]. Specific emphasis is placed upon charge transport in the latter part of the chapter, since it has relevance throughout this work. The next chapter, chapter 3, describes the interactions of particles in a semiconductor device and the resultant physical processes. The physics contained here is included within the Monte Carlo code MCNP (*Monte-Carlo N-Particle*) [16], which has been utilised throughout chapters 4, 6 and 7. Detection techniques are also discussed in this chapter, with reference to state of the art pixel detectors of the type studied here.

Chapter 4 details the characteristics of two silicon pixel detectors intended for spectroscopy - the ERD1 and its successor the Dash-E detector. These detectors were designed and built by Paul Seller and the microelectronics group at the Rutherford Appleton Laboratories. This chapter introduces the detectors, so that an understanding of the devices can be developed before the results are compared with the models.

Next, the focus switches to the simulation of a novel pixellated detector structure, which has the potential to solve many of the limiting factors listed above. The so-called 3-D detector has a geometry that lends itself to an increased radiation hardness. Additionally a thick detection layer may be realised without compromising charge carrier extraction. The fabrication steps are, however, more complex and an aspect of this fabrication is studied

through modelling.

Chapter 7 explores the charge transport properties of a material, Cadmium Zinc Telluride (CdZnTe), which could extend the application of pixellated detectors to higher energy X and γ -rays - above 100 keV. A model is also developed here to analyse the sharing of charge between adjacent pixel elements.

The penultimate chapter (chapter 5) is concerned with the comparison of the theoretical models using the Dash-E detector. The predictions of the models are also examined in the latter sections of this chapter. The work concludes with a discussion of the main results.

Publications

Main Author

- K. Mathieson et al., "Simulation of GaAs 3-D pixel detectors", Presented at the 2nd International Workshop on Radiation Imaging Detectors, Freiburg Germany Jun. 2000, *submitted to Nucl. Instr. Meth. A*.
- K. Mathieson et al., "The Simulation of Charge Sharing in Semiconductor X-ray pixel detectors", *Proc. of the 5th International Conference on Position-Sensitive Detectors 1999*, To be published in Nucl. Instr. Meth. A.
- K. Mathieson et al., "Simulated and Experimental Results from a Room Temperature Silicon X-ray Pixel Detector", *Nucl. Instr. Meth. A*

460(1)(2001)

Named Author

- M. Rahman et al., “Quantum electron beam probe of sidewall dry-etch damage”, *Microelectron. Eng.* **53**, (2000) 371-374.
- M. Rahman and K. Mathieson, “Topographic effects in low-energy radiation damage”, *Appl. Phys. Lett.*, **77** (9) (2000).
- S. Manolopoulos et al., “Developments in GaAs Pixel Detectors for X-ray Imaging”, *IEEE Trans. Nucl. Sci.*, **45** (3) 1998.
- R. Bates et al., “Development of low pressure vapour-phase epitaxial GaAs for medical imaging”, *Nucl. Instr. Meth. A* **434**(1) (1999), 1-13.
- J. Watt et. al., “Application of pixellated GaAs X-ray detectors in a synchrotron radiation beam”, *Nucl. Instr. and Meth A* **460**(1)(2001) 185-190.
- G. Iles et al. “Large-area pixellated photon counting X-ray imaging system”, *Nucl. Instr. Meth. A* **438** (1) (2001) 427-430.
- M.S. Passmore et al., “Characterisation of a Single Photon Counting Pixel Detector”, Presented at the 2nd International Workshop on Radiation Imaging Detectors, Freiburg Germany Jun. 2000, *submitted to Nucl. Instr. and Meth A*.

-
- P. Seller et al., “Two approaches to hybrid X-ray pixel array read-out”, *SPIE* **3774**, Detectors for Crystallography and Diffraction Studies at Synchrotron Sources, 1999.
 - P. Seller et al., “Performance of an energy resolving X-ray pixel detector”, *Proc. of the 5th International Conference on Position-Sensitive Detectors*, To be published in Nucl. Instr. and Meth A. 1999.

Chapter 2

Semiconductor physics

2.1 Introduction

The semiconductor has had a profound effect on many areas of science and industry. Their earliest applications were as low frequency rectifiers, which were first made in 1886 by C.E. Fritts using selenium. Since then focus has shifted to other semiconducting materials, with silicon and germanium becoming the best documented. The fabrication of the solid-state transistor in 1948 revolutionised the electronics industry, which underwent a further revolution with the advent of integrated circuits. Advances such as these have meant that complex systems like the desktop computer have been realised. The effect that semiconductor research has had on the current communications explosion - from mobile phones to miniature laptops - also cannot be underestimated. Other devices such as the solar cell, infra-red photo detectors and the solid state laser have made significant impacts in both fundamental research and industry.

The aim of this chapter is to introduce the basic semiconductor principles

which will allow an understanding of the work in the subsequent chapters. The concepts of crystal structure and energy bands, and the properties of various semiconductors will be discussed. Details of carrier transport will also be introduced and the chapter will conclude with the important equations of device modelling.

Many books and review articles have been written on the properties of semiconductors, with one of the most popular being, “Physics of Semiconductor Devices” by Sze [17]. Others used in this chapter are “Semiconductors” by R.A. Smith [18] and “Semiconductor Radiation Detectors” by G. Lutz [19]. Figures have also been taken from W. Shockley’s “Electrons and Holes in Semiconductors” [20], which contains much of the pioneering work carried out in this field.

2.2 Crystal structure

The majority of semiconductors that have found use as detectors are of the single crystal variety. This means that the atoms are arranged in a periodic three-dimensional structure known as a lattice. The two most common elemental materials, Si and Ge, possess a diamond lattice structure, while the compound materials such as GaAs and CdZnTe have the zinc blende lattice type. These lattices can be seen in figure 2.1 where their unit cells are highlighted.

Both lattices can be described as a composite of two face centred cubic (fcc) sublattices, displaced by a quarter of the unit cell size along the diagonal of the cube. For the diamond structure all atoms are of the same type, while for the zinc blende lattice the atoms of the two fcc sublattices differ. Each of

2.3 Energy bands

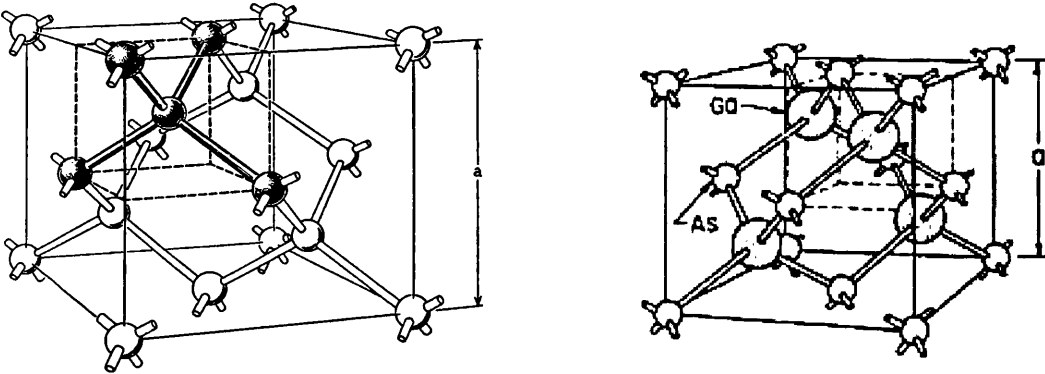


Figure 2.1: The diamond and zinc blende lattice structures respectively (After Sze 1985, p. 5 Fig. 3).

the constituent atoms has four nearest neighbours which belong to the other fcc sublattice. They form a tetrahedral structure and share their four valence electrons with these neighbouring atoms. This forms the covalent bonding structure, with a slight ionic component in the compound semiconductors, that holds the periodicity of the lattice.

2.3 Energy bands

When this lattice structure is extended it forms a representation of a single crystal. The valence electrons which hold the lattice together remain in this bound state. These bonds can be broken however and the resultant electron and the 'hole' it has left behind are free to conduct. The formation of an electron-hole pair can be caused, for example, by thermal energy or by the passage of ionising radiation. An enhancement of this picture can be formed if the crystal is considered in terms of single atoms.

A single atom has well known quantised energy states in which the orbiting

electrons can exist. When two identical atoms are separated by a large distance, they have no influence on each other and their electrons exist in their degenerate states. However as these atoms move closer together the energy levels split into two due to the interaction between the atoms. If N atoms are considered instead of two, the energy levels will split into N distinct, closely spaced levels which are more easily considered as a continuous band of energy.

This is illustrated in figure 2.2 where the isolated atoms are brought closer

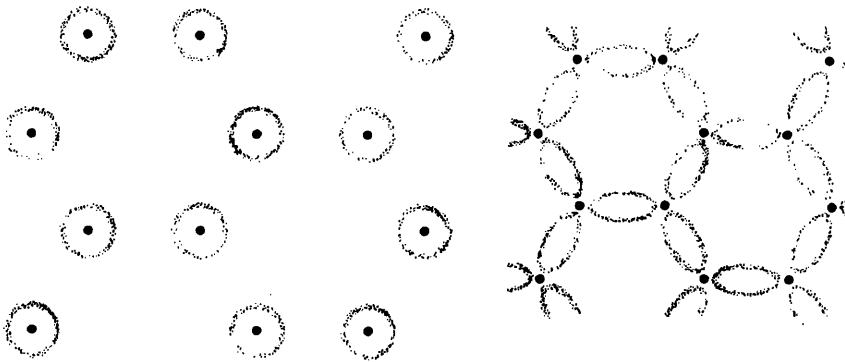


Figure 2.2: The formation of energy bands (After Harrison 1980).

together allowing the valence electrons to form bonds and fixing the atoms' position in space. A schematic representation of this process is shown in figure 2.3. Here the changes that the atomic energy levels of silicon undergo as it forms a diamond structure with other silicon atoms are shown. On the far right of the diagram two distinct states can be seen, in which the orbiting electrons can exist. As the distance between atoms is reduced the interactions between the electrons start, the allowed energy states cease to

2.3 Energy bands

be distinct and the formation of bands begin. As the atoms move still closer the bands merge and become one. The atoms, being of like charge, feel a repulsive force which counteracts the attractive force, due to the electron proton interactions, and the atoms settle into an equilibrium position. Where this equilibrium position is in terms of lattice spacing determines whether the material is metal, semiconductor or insulator. The bands then split into two allowed energy states for electrons. Between these states is a forbidden region where no electrons can exist. This is known as the band gap and is perhaps the most important parameter in semiconductor physics.

All solids can be described by this energy band model. In figure 2.4 the

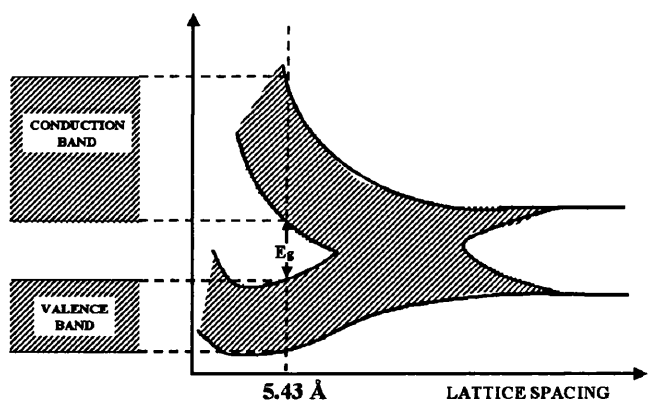


Figure 2.3: The energy levels of silicon atoms in a diamond structure (After Sze 1985, p. 10 Fig. 8).

band structures for the three cases insulator, semiconductor and conductor are shown. The semiconductor has an equilibrium spacing of atoms that leads to a band gap that is of the order of 1 eV. This means that at room

temperature some of the bonds can be broken by thermal vibrations, leading to electrons in the conduction band and holes in the valence band which are free to conduct.

This gives a semiconductor its lightly conducting properties, which are ab-

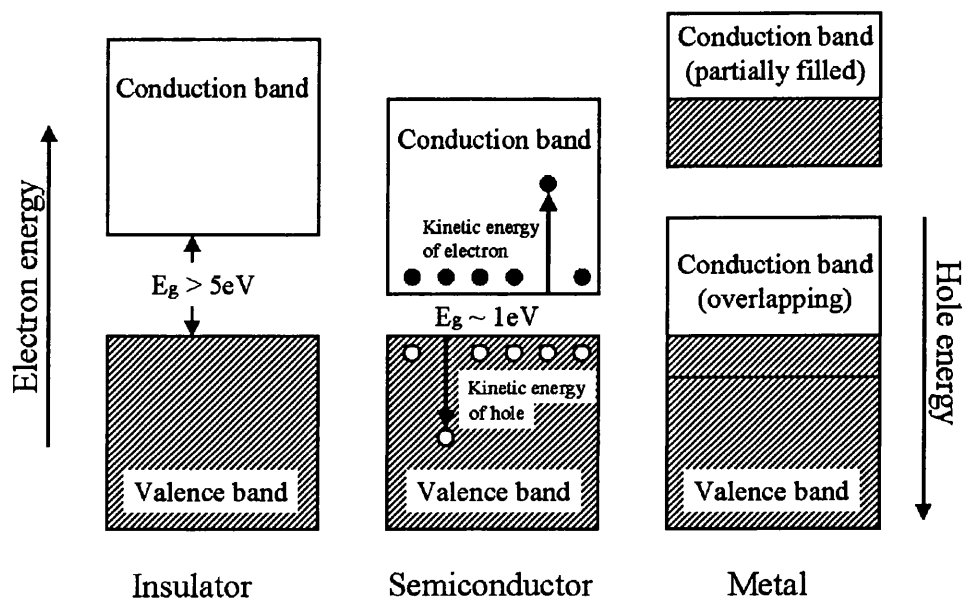


Figure 2.4: The band structure of insulators, semiconductors and metals (After Sze 1985, p. 11 Fig. 9)

sent when the thermal energy is lower than that of the band gap. In these conditions semiconductors behave as insulators, where the band gap is too large for any conduction to take place. Conductors exhibit a partially filled conduction band or overlapping valence and conduction bands and so conduct at all temperatures above zero Kelvin.

2.4 Intrinsic and Extrinsic Semiconductors

2.3.1 Effective Mass

The kinetic energy of a free electron is given by equation 2.1 where p is the particle momentum and m_o is the free-electron mass.

$$E = \frac{\vec{p}^2}{2m_o} \quad (2.1)$$

An electron in the conduction band can be considered as a free particle, however because of the periodic potential of the nuclei the effective mass of the electron differs. The energy-momentum relation for a conduction electron is shown in equation 2.2.

$$E = \frac{\vec{p}^2}{2m_n} \quad (2.2)$$

Here \vec{p} is the crystal momentum and m_n is the effective mass of the conduction electron in the crystal. A similar equation for holes can be expressed by replacing the mass term with m_p , the effective mass of a hole in the valence band. This concept of effective masses allows the particles to be viewed as classical charged particles.

2.4 Intrinsic and Extrinsic Semiconductors

Semiconductors can be broken down into 2 categories - intrinsic and extrinsic. The definition of an intrinsic semiconductor is one which contains no impurities. In practice they will always contain some defects, but these will be few in comparison with the number of thermally generated electrons and holes. If the electron density, $n(E)$, in an intrinsic semiconductor is considered it will give an indication as to what concentrations of defects can be tolerated in an 'intrinsic' material. The electron density is given by the

product of the density of allowed energy states per unit volume $N(E)$, and the probability $F(E)$ of occupying that energy range $d(E)$. The electron density in the conduction band can then be found by integrating over the conduction band, expressed mathematically as :

$$n = \int_{E_C}^{E_{top}} n(E) dE = \int_{E_C}^{E_{top}} N(E) F(E) dE \quad (2.3)$$

The probability that an electronic state is occupied by an electron, $F(E)$, is given by a fundamental equation of statistical mechanics. This is known as the Fermi-Dirac distribution function and is shown below in equation 2.4

$$F(E) = \frac{1}{1 + e^{\frac{(E-E_F)}{kT}}} \quad (2.4)$$

Here E_F is the Fermi energy and is defined as the the energy at which the probability of an electron occupying a possible state is exactly one half, k is the Boltzmann constant and T the absolute temperature. These parameters can be represented schematically - and the band structure, density of states, occupation probability and the electron/hole densities are shown for an intrinsic semiconductor in figure 2.5. It can be seen from 2.5 (d) that the number density of holes is equal to the number density of electrons i.e. $n = p = n_i$ where n_i is the intrinsic carrier density. This equation can be expressed in the more general form of the mass action law :

$$np = n_i^2 \quad (2.5)$$

This equation holds for intrinsic and extrinsic semiconductors so long as they are in thermal equilibrium. For extrinsic materials the increase of one type of carrier leads to a decrease in the number density of the other type of carrier,

2.4 Intrinsic and Extrinsic Semiconductors

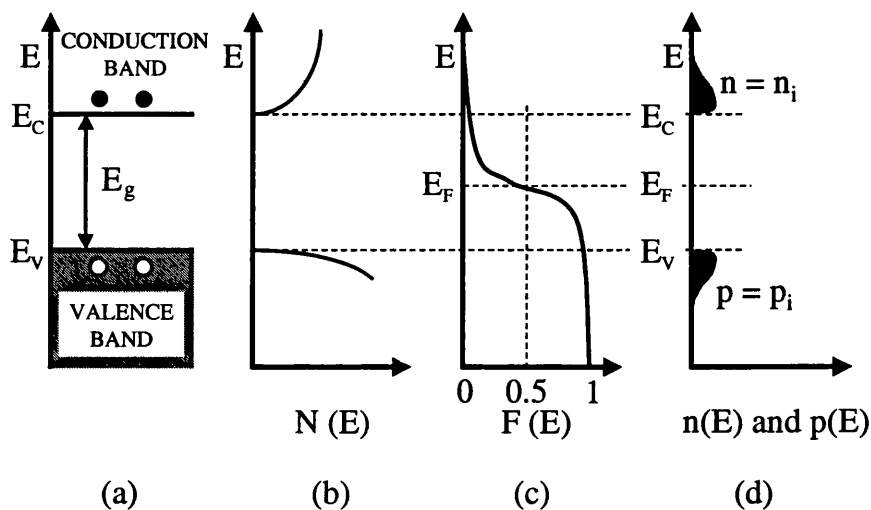


Figure 2.5: The intrinsic semiconductor : (a) the band structure, (b) density of states, (c) occupation probability and (d) the electron/hole densities (After Sze 1985, p.18 Fig. 15).

through recombination mechanisms (see section 2.6.4). This means that although n and p vary their product remains constant at a given temperature.

2.4.1 Extrinsic Semiconductors

Extrinsic semiconductors contain impurities which are generally placed there intentionally. The fact that purity is not such an issue with these semiconductors means that they have found more applications than their intrinsic counterparts. Device characteristics can be controlled by the addition of a small amount of impurities in a process known as doping. These can be incorporated during the crystal growth procedures or can be placed in specific

areas later on in the processing steps. Differing impurity atoms can have dramatically different effects on the electrical behaviour of the semiconductor. Two types of doping are possible: n-type, where additional electrons are introduced into the conduction band, and p-type where free holes are available for conduction in the valence band. These two cases can be seen for silicon in figures 2.6 and 2.7, where arsenic is used as a n-type dopant and boron is used as a p-type dopant.

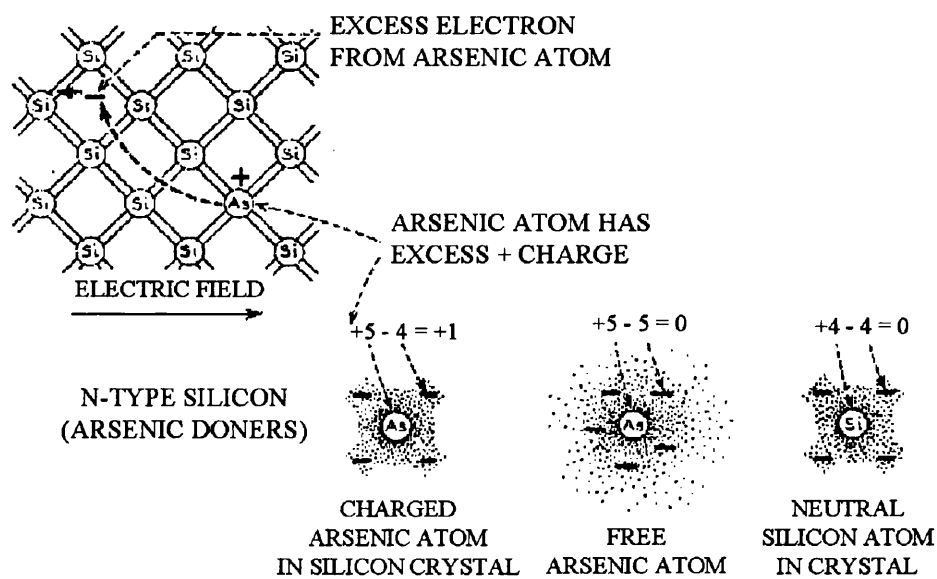


Figure 2.6: Arsenic as a n-type dopant in silicon (After Schockley 1950, p. 13 Fig. 1-7)

The conductivity in silicon, for the n-type arsenic doping, arises from the

2.4 Intrinsic and Extrinsic Semiconductors

presence of these arsenic impurity atoms. The arsenic atom has a core which contains a +5 charge and 5 valence electrons which balance this charge. The arsenic atom displaces a silicon atom in the lattice and forms four covalent bonds with the neighbouring silicon atoms. This leaves one unbound electron which can be considered as a localised, *mobile* negative charge. The arsenic atom is then considered as an *immobile* positive charge, since the +5 core has not been neutralised by the 4 valence electrons participating in the covalent bonding. The charge neutrality of the crystal is maintained however, since the positively charged arsenic atom exactly balances the excess electron. These negative electrons are attracted to the positive arsenic atoms and at low temperatures become bound to them. However at room temperature thermal agitation shakes them off and the electrons are free to conduct.

The converse of this effect is p-type doping, and in silicon boron is a commonly used dopant. It has three valence electrons and so cannot complete the covalent bonds. There exists a hole in one of the bonds to the boron atom, which can be filled by an electron from an adjacent bonding site, allowing the hole in effect to migrate away. It can therefore be seen as a localised, *mobile* positive charge. The boron atom, since it has accepted an electron to complete its bonds, can be regarded as a negative charge, which is localised and *immobile*. Due to the symmetry between the behaviour of electrons and holes, the situation shown in figure 2.7, can be described in terms of the negative boron atom attracting the positive hole. Again at low temperatures the hole will become associated with this site. At higher temperatures, such as room temperature, the thermal agitation liberates the hole allowing con-

duction.

If these effects are examined using the band model, it can be seen that

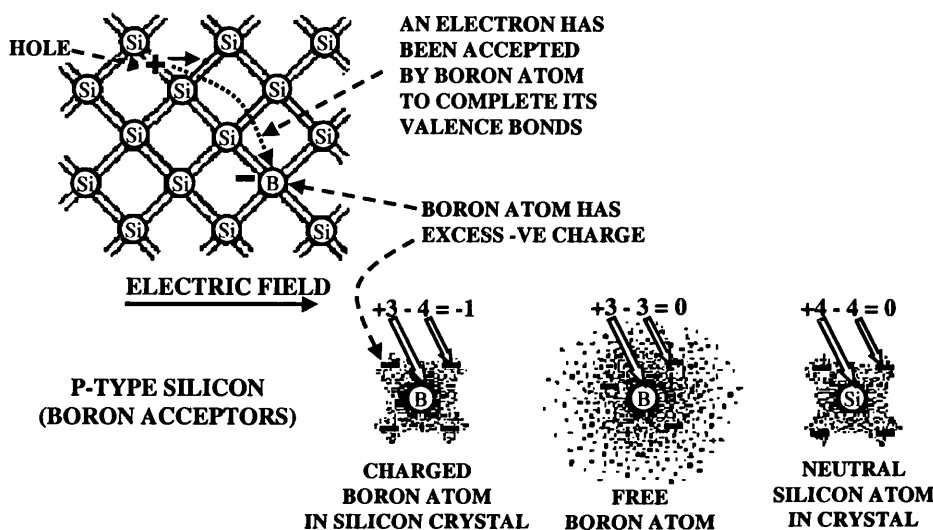


Figure 2.7: Boron as a p-type dopant in silicon (After Schockley 1950, p. 14 Fig. 1-8)

replacing the native atom with an impurity atom, creates localised energy levels in the band gap. The energy levels can be donors or acceptors, denoted (E_D) and (E_A) in figure 2.8. If the donor levels are located close to the conduction band then it takes very little energy to excite their electrons into this band. These donor centres will therefore, at room temperature, be mostly ionised. An example of this kind of donor atom, in silicon, is arsenic which creates a level located 0.054 eV below the conduction band. The same

2.5 Carrier Transport in Semiconductors

effects are true for acceptor atoms. If they sit just above the valence band then they will easily accept electrons becoming ionised and leaving a hole in the valence band. Boron is such an atom in silicon contributing a level located 0.045 eV above the valence band.

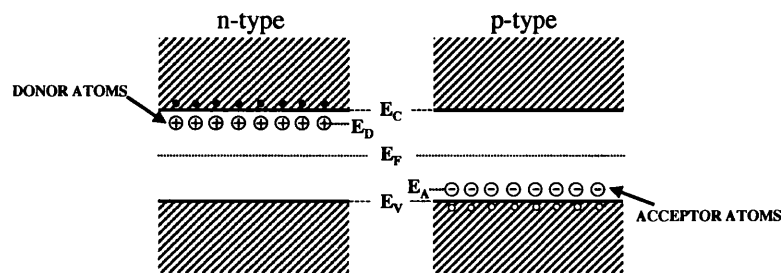


Figure 2.8: Energy band diagrams for extrinsic semiconductors, n-type and p-type respectively

2.5 Carrier Transport in Semiconductors

The previous sections dealt with semiconductors in their natural equilibrium state. No external voltages were considered, the charge distribution was homogeneous and no carriers were created or destroyed. These cases will be analysed in this section. The processes of drift (movement of charge carriers due to the presence of an electric field) and diffusion (whereby an uneven distribution of charges rearranges itself to achieve an equilibrium condition) are examined. Firstly some aspects of charge carrier movement in general must be discussed.

Electrons in the conduction band and holes in the valence band can be essentially considered as free particles. They have a mean kinetic energy of $\frac{3}{2}kT$,

which leads to a thermal velocity of the order of 10^7 cm/s. These free carriers scatter off any imperfections in the lattice periodicity, whether these be donors, acceptors, defects or quantised thermal lattice vibrations (phonons). They have a typical mean collision time, τ_c , of 10^{-12} s, giving a mean free distance of around 10^{-5} cm.

2.5.1 Drift

The thermal energy given to electrons in a semiconductor crystal leads to the charge carriers being in constant motion. This motion will however, be random resulting in no net displacement. When an electric field, E is applied each electron will feel a force equal to $-qE$ and will move in the opposite direction to that of the electric field vector. The charge will still undergo collisions but will suffer a displacement due to the electric field. If the momentum given to an electron by the electric field, during the time between collisions, is equated with the momentum gained then (2.6) is found.

$$-qE\tau_c = m_n\nu_n \quad (2.6)$$

Which yields the more useful expression of equation (2.7).

$$\nu_n = -\left(\frac{q\tau_c}{m_n}\right)E = -\mu_n E \quad (2.7)$$

This equation shows that the electron drift velocity is directly proportional to the applied electric field. The constant of proportionality is known as the mobility of the carrier and is denoted μ_n , it has units of $\text{cm}^2/\text{V}\cdot\text{s}$. The corresponding equation for holes has the same form, with m_p and μ_p substituting the electron terms. The mobility is an important parameter for charge transport in semiconductor devices. It depends upon two terms, the effective mass

2.5 Carrier Transport in Semiconductors

of the carrier considered and the scattering time, τ_c . This time depends upon scattering from thermal vibrations upsetting the periodicity of the lattice and any Coulomb interactions with ionised donor or acceptor states. There are two principle effects to be considered here - as the temperature increases the thermal velocity increases which means the time the charge has to interact with any ionised state is reduced. This leads to an initial increase of mobility with temperature. However as the temperature rises still further, the mobility begins to decrease due to the onset of scattering from thermal vibrations. On the other hand an increase in doping concentration will, in general, lead to a decrease in the mobility simply due to scattering from these sites. It should be noted that equation 2.7 becomes invalid at high values of electric field. The values of mobility become non-linear and the drift velocities saturate. At still higher fields the process of impact ionisation starts. This is where the carriers gain enough energy from the field, that they can excite additional electron-hole pairs. Typical fields where deviations from linearity occur are $\approx 10^4$ V/cm in silicon and around 2×10^3 V/cm in GaAs.

2.5.2 Diffusion

Diffusion is the process which describes the movement of charge carriers from a region of high concentration to a region of low concentration. This effect has nothing to do with any electrical fields or Coulomb interactions. It arises solely due to the fact that it is more probable that a carrier in a high concentration area will move into an area of lower concentration, since there are more carriers available to do so. It can be expressed mathematically by

the diffusion equation (2.8).

$$\begin{aligned} F_n &= -D_n \nabla n && \text{for electrons and} \\ F_p &= -D_p \nabla p && \text{for holes.} \end{aligned} \quad (2.8)$$

F_n and F_p are the flux of electron and holes respectively and $\nabla n, \nabla p$ are their carrier concentration gradients. The diffusion constant D_n (and similarly D_p) can be related to the carrier mobility by the Einstein equation shown in (2.9).

$$D_n = \left(\frac{kT}{q} \right) \mu_n \quad (2.9)$$

The diffusivity of a material then depends upon the temperature of the sample, the impurity levels present and the effective mass of the charge carriers.

2.5.3 Current Density Equations

These two effects, drift and diffusion, both deal with the movement of the charge carriers. Whether this movement is the result of an electric field or an inhomogeneous carrier concentration, it will result in a conduction current. The current resulting from the drift of electrons or holes can be derived if the net flow through a surface is examined. Here the case of electrons only will be taken, however the argument holds for holes also. Taking a uniformly doped semiconductor of cross sectional area A and length L , with an electron concentration of n (cm^{-3}) the electron current density can be easily deduced. This is shown schematically in figure 2.9. An electric field E is applied across the sample causing the electrons to drift and resulting in a current through area A . This electron current density, J_n , is simply a sum over n of the product of the charge on the electron and its velocity, ν_n .

2.5 Carrier Transport in Semiconductors

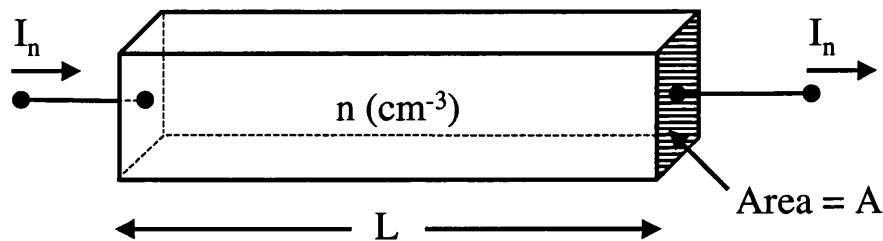


Figure 2.9: Current conduction in a uniformly doped semiconductor (After Sze 1985, p. 36, Fig. 5)

$$J_n = \frac{I_n}{A} = \sum_{i=0}^n (-q\nu_i) = -qn\nu_n = qn\mu_n E \quad (2.10)$$

Here I_n is the electron current flowing out of both sides of the semiconductor sample. A similar expression for holes can be derived by following a similar argument. The two contributions combine to give the total current flowing due to the electric field.

$$J = J_n + J_p = (qn\mu_n + qp\mu_p)E \quad (2.11)$$

The term in (2.11) contained within the parentheses is known as the conductivity, σ , of the semiconductor. The reciprocal of the conductivity is the resistivity, ρ . For the case of extrinsic semiconductors one term dominates since there are orders of magnitude differences in the carrier densities. This leads to the shortened form of the resistivity equation shown below.

$$\rho = \frac{1}{qn\mu_n} \quad \text{or} \quad = \frac{1}{qp\mu_p} \quad (2.12)$$

for n and p-type semiconductors respectively. The current that arises due to diffusion occurs since there is a flux F of electrons with charge $-q$ moving in the sample. This can be written as :

$$J_n = -qF_n = qD_n \nabla_n \quad (2.13)$$

using equation 2.8. These two electron currents, arising from the drift and diffusion of the charge carriers, can be combined into one equation giving a general form for the conduction current.

$$J_n = qn\mu_n E + qD_n \nabla_n \quad (2.14)$$

with the corresponding equation for holes being :

$$J_p = qp\mu_p E - qD_p \nabla_p \quad (2.15)$$

The opposing sign has been used in the diffusion term of (2.15) since holes will diffuse in the opposite direction to that of their positive concentration gradient. The electron and hole contributions can be summed to give the total conduction current :

$$J_{cond} = J_n + J_p \quad (2.16)$$

These last three equations form the current density equations, which are valid for electric fields that are below the saturation conditions outlined in subsection 2.5.1. These equations are extremely useful for the analysis of device behaviour under these conditions.

2.6 Carrier Generation and Recombination in Semiconductors

The generation of charge in a semiconductor can occur due to three processes, namely :

- thermal processes
- optical excitation
- the passage of ionising radiation.

These processes are all capable of providing enough energy to excite an electron from the valence band to the conduction band, thus creating an electron hole pair. They will be discussed in the following section along with the complementary process of recombination.

2.6.1 Thermal Generation of Charge Carriers

Thermal generation can occur either directly (band to band) or indirectly (via energy levels in the forbidden region). For the transition to occur directly, at room temperature, the band gap of the semiconductor has to be small enough that the thermal voltage, $\frac{kT}{q} = 0.0259$ V, has a large enough effect on the occupation probability of the conduction band. In germanium, which has a band gap of 0.67 eV, the thermal voltage has a pronounced effect, leading to large leakage currents at room temperature. These currents, or more precisely the fluctuations in their values, destroy the excellent

energy resolution inherent in germanium detectors. They impose a cryogenic temperature of ≈ 77 K on the use of these devices. Silicon, gallium arsenide, cadmium telluride and cadmium zinc telluride all have band gaps that permit the room temperature operation of these materials as radiation detectors. However defect states and impurity levels in the band gap in all of these materials lead to thermal excitation indirectly through the resultant intermediate states. These defect levels degrade the detection properties of the materials to such an extent that some of the most extensive research currently being carried out in this field is in material improvement.

2.6.2 Generation of Charge Carriers by Electromagnetic Radiation

When electromagnetic radiation interacts in a semiconductor crystal it can impart enough energy to the lattice that it causes some bonds to be broken. In the band theory of solids this is equivalent to raising an electron from the valence band into the conduction band leaving a hole behind. This electron hole creation by photon interactions is the basis of photodetectors and solar cells. The three principal processes are shown in figure 2.10 where a photon can either :

- give just enough energy to the lattice to excite an electron to the bottom of the conduction band.
- impart more energy than is necessary and the electron and hole occupy empty states higher in their respective bands. The carriers then make their way to the band edges by losing energy via phonon interactions.

2.6 Carrier Generation and Recombination in Semiconductors

- lose energy with the involvement of a localised state. The energy of the photon is not enough to allow a band to band transition but is enough to excite an electron to the empty defect state. This leads to the creation of a hole and an ionised state in the forbidden region.

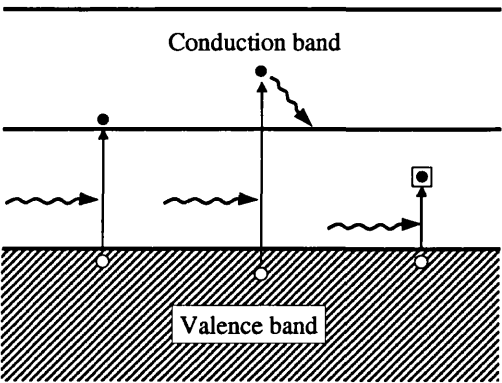


Figure 2.10: Generation of electron and holes due to the absorption of electromagnetic radiation. The three cases of $E_{\text{photon}} = E_g$, $E_{\text{photon}} > E_g$ and $E_{\text{photon}} < E_g$ are shown (After Lutz 1999, p.22, Fig 2.13).

The generation of electron hole pairs due to the passage of charged particles is described by the Bethe-Bloch formula and will be covered later in section 3.2.

2.6.3 Multiplication Processes

Multiplication of charge carriers takes place in areas of a semiconductor where the electric field is sufficient to give a carrier enough kinetic energy to liberate another carrier when it collides with a lattice site. This phenomenon

is sometimes known as impact ionisation. It can lead to breakdown in a detector whereby the leakage current of the device becomes so large that it degrades its detection properties. This effect can also be put to good use, as in avalanche detectors. Here the electric field is high enough to allow the migrating electrons to create secondary electrons. This increases the gain of the detector but with the charge multiplication factor being a strong function of the electric field, small non-uniformities in the detection material cause non homogeneous detection properties. This limits the size of the detectors to a few mm².

2.6.4 Recombination

Once the generation of charge has occurred the mechanism that returns the semiconductor back to an equilibrium state is *recombination*. The minority charge carriers (electrons in p-type material or holes in n-type material) combine with the majority charge carriers in this recombination process. This tendency to return to equilibrium differs substantially for direct and indirect semiconductors. The two cases are dealt with separately in the following sections and are considered in terms of their carrier lifetimes. This parameter, along with the mobility, is the most important variable where detector grade material is concerned.

Direct recombination

When a semiconductor is said to be in equilibrium it does not mean that all physical processes within the semiconductor have reached a stationary state. The semiconductor will instead be in a state of continual recombination and

2.6 Carrier Generation and Recombination in Semiconductors

generation. Put simply, the generation rate G is equal to the recombination rate, R , and both are proportional to the electron and hole concentrations.

$$R = \beta np \quad (2.17)$$

Where β is the proportionality factor. In thermal equilibrium equation 2.17 becomes :

$$R_{th} = G_{th} = \beta n_0 p_0 = \beta n_i^2 \quad (2.18)$$

leading to the definition of excess recombination rate U as :

$$U = R - R_{th} = \beta(np - n_i^2) \quad (2.19)$$

If a sample is then illuminated with light so that the thermal equilibrium conditions are upset, then the electron and hole concentrations will be increased by the same amount Δn - since the carriers are produced in pairs. This increases the recombination rate to

$$R = \beta(n_0 + \Delta n)(p_0 + \Delta n) \quad (2.20)$$

If the illumination is constant then the additional generation rate (G_L) is given by

$$G_L = \beta \Delta n_L (p_0 + n_0 + \Delta n_L) \quad (2.21)$$

and is equal to the excess recombination rate of equation 2.19, where Δn_L is the excess minority carriers generated by the incident light. If the injected carrier concentration is much less than the majority carrier concentration then the previous equation simplifies to :

$$G_L = \frac{\Delta n_L}{\tau_r} \quad (2.22)$$

where

$$\tau_r = \frac{1}{\beta p_0} \quad \text{for p-type materials}$$

and

$$\tau_r = \frac{1}{\beta n_0} \quad \text{for n-type materials} \quad (2.23)$$

If the light incident upon the semiconductor is removed, then the material will return to equilibrium with a time constant of τ_r . This parameter is known as the recombination lifetime and these equations hold for direct semiconductors such as GaAs. A direct semiconductor is one in which the minima of the conduction band is aligned with the maxima of the valence band in momentum space. This means that there does not have to be a transfer of momentum for a charge carrier to move from one band to another.

Indirect recombination and trapping

For indirect semiconductors such as silicon and germanium, the probability of a band to band transition is very low. This is because the holes at the top of the valence band have a different crystal momentum to the electrons at the bottom of the conduction band. The recombination process instead occurs with the help of localised states in the band gap. These states are the results of imperfections in the crystal lattice and are sometimes referred to as trapping centres. They can affect the charge collection of a detector by trapping the carriers and, if the levels are deep enough in the band gap, can hold onto the charge for a significant length of time. A defect state can undergo four basic transitions, and these are shown in figure 2.11. Here the possible evolution of a single defect level is displayed. The level can be neutral and become negatively charged by accepting an electron from the conduction

2.6 Carrier Generation and Recombination in Semiconductors

band. This is shown in a) and is known as electron capture. Electron emission is shown in b) and consists of a negatively charged state emitting an electron into the conduction band and becoming neutral. In c) the process of hole capture can be seen. A hole in the valence band recombines with an electron from a charged trapping centre. The final mechanism, hole emission, is shown in d). An electron is excited into the defect level creating a free hole and an occupied trapping site.

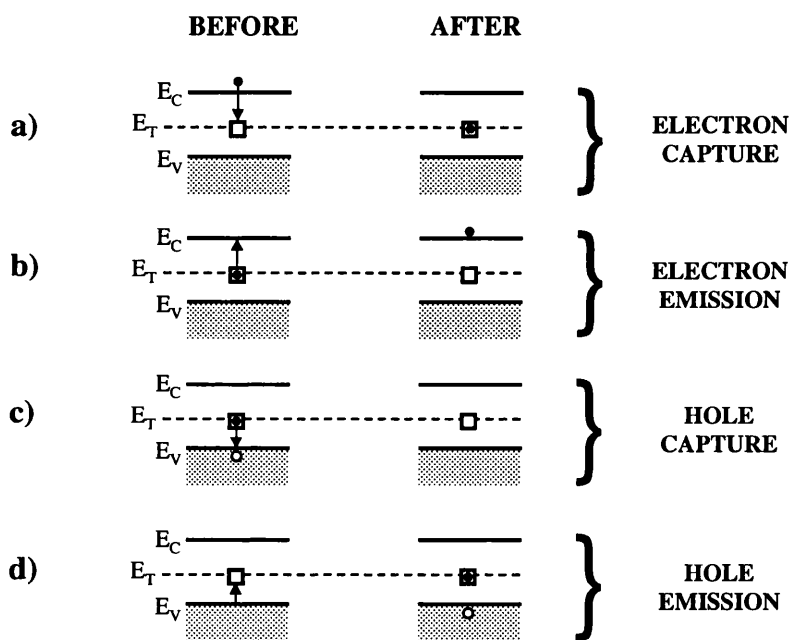


Figure 2.11: Indirect generation - recombination processes at thermal equilibrium (Adapted from Sze 1985, p. 49 Fig. 13).

These four processes can be combined to give important recombination/generation processes. For example, steps a) and c) together give electron hole recombination and coupling steps a) and b) gives the process of trapping and

de-trapping - an important effect when discussing the charge collection properties in semiconductor detectors. It is therefore important to know the time development of these trapping states and these are often studied in terms of capture cross sections and emission probabilities. If n and p are the electron and hole concentrations, N_T is the trap concentration and P_t is the occupation probability, then the rates of the four processes shown in figure 2.11 are given by :

$$\begin{aligned}
 R_{c,n} &= \nu_{th,n} \sigma_n n N_t (1 - P_t) \\
 R_{\epsilon,n} &= \epsilon_n N_t P_t \\
 R_{c,p} &= \nu_{th,p} \sigma_p p N_t P_t \\
 R_{\epsilon,p} &= \epsilon_p N_t (1 - P_t)
 \end{aligned} \tag{2.24}$$

The four rates are electron capture, $R_{c,n}$, electron emission, $R_{\epsilon,n}$, hole capture, $R_{c,p}$ and hole emission, $R_{\epsilon,p}$. The thermal velocity, ν_{th} , capture cross sections, σ , and emission probability, ϵ also play their role in these equations. In thermal equilibrium the emission and capture rates for the same carrier have to be equal, since the electron and hole concentrations and the average defect occupation probability do not change. This probability, P_t , is governed by the Fermi function at the defect energy level, E_t :

$$R_{c,n} = R_{\epsilon,n} \tag{2.25}$$

$$R_{c,p} = R_{\epsilon,p} \tag{2.26}$$

$$P_t = F(E_t) = \frac{1}{1 + e^{\frac{E_t - E_F}{kT}}} \tag{2.27}$$

If the above equations are combined with equations 2.24 and the law of mass action (2.5) then the following expressions for emission probabilities

2.6 Carrier Generation and Recombination in Semiconductors

are obtained :

$$\epsilon_n = \nu_{th,n} \sigma_n n_i e^{\frac{E_t - E_i}{kT}} \quad (2.28)$$

$$\epsilon_p = \nu_{th,p} \sigma_p n_i e^{\frac{E_i - E_t}{kT}} \quad (2.29)$$

If the stationary non-equilibrium case is considered then the net recombination rate, U , is the difference between the capture and emission rates. The recombination rate will be the same for electrons and holes since the average occupation rate of the defects remains constant. This is expressed mathematically in equation 2.30.

$$\begin{aligned} U &= R_{c,n} - R_{\epsilon,n} = N_t \nu_{th,n} \sigma_n [n(1 - P_t) - n_i e^{\frac{E_t - E_i}{kT}} P_t] \\ &= R_{c,p} - R_{\epsilon,p} = N_t \nu_{th,p} \sigma_p [p P_t - n_i e^{\frac{E_i - E_t}{kT}} (1 - P_t)] \end{aligned} \quad (2.30)$$

Using the above equation the following terms for the occupation probability can be found :

$$P_t = \frac{\nu_{th,n} \sigma_n n + \nu_{th,p} \sigma_p n_i e^{\frac{E_i - E_t}{kT}}}{\nu_{th,p} \sigma_p p + \nu_{th,n} \sigma_n n_i e^{\frac{E_t - E_i}{kT}} + \nu_{th,n} \sigma_n n + \nu_{th,p} \sigma_p n_i e^{\frac{E_i - E_t}{kT}}} \quad (2.31)$$

$$1 - P_t = \frac{\nu_{th,p} \sigma_p p + \nu_{th,n} \sigma_n n_i e^{\frac{E_t - E_i}{kT}}}{\nu_{th,p} \sigma_p p + \nu_{th,n} \sigma_n n_i e^{\frac{E_t - E_i}{kT}} + \nu_{th,n} \sigma_n n + \nu_{th,p} \sigma_p n_i e^{\frac{E_i - E_t}{kT}}} \quad (2.32)$$

Combining equations 2.31 and 2.32 with 2.30 gives the net excess recombination rate for indirect semiconductors :

$$U = \frac{N_t \nu_{th,n} \sigma_n \nu_{th,p} \sigma_p (np - n_i^2)}{\nu_{th,n} \sigma_n \left[n + n_i e^{\frac{E_t - E_i}{kT}} \right] + \nu_{th,p} \sigma_p \left[p + n_i e^{\frac{E_i - E_t}{kT}} \right]} \quad (2.33)$$

Using equation 2.19 the above equation yields the constant of proportionality as:

$$\beta = \frac{N_t \nu_{th,n} \sigma_n \nu_{th,p} \sigma_p}{\nu_{th,n} \sigma_n \left[n + n_i e^{\frac{E_t - E_i}{kT}} \right] + \nu_{th,p} \sigma_p \left[p + n_i e^{\frac{E_i - E_t}{kT}} \right]} \quad (2.34)$$

allowing the recombination time constants to be found for n-type (2.35) and p-type (2.36) semiconductors.

$$\tau_{r,n} = \frac{1}{\beta n_0} \approx \frac{1 + \frac{n_i}{n_0} \left[\frac{\nu_{th,p} \sigma_p}{\nu_{th,n} \sigma_n} e^{\frac{E_i - E_t}{kT}} + e^{\frac{E_t - E_i}{kT}} \right]}{\nu_{th,p} \sigma_p N_t} \quad (2.35)$$

$$\tau_{r,p} = \frac{1}{\beta p_0} \approx \frac{1 + \frac{n_i}{p_0} \left[\frac{\nu_{th,n} \sigma_n}{\nu_{th,p} \sigma_p} e^{\frac{E_t - E_i}{kT}} + e^{\frac{E_i - E_t}{kT}} \right]}{\nu_{th,n} \sigma_n N_t} \quad (2.36)$$

Here n_0 and p_0 are the majority carrier concentrations and are usually much greater than the intrinsic carrier concentration.

The generation lifetime is defined as the ratio of intrinsic charge density to initial generation rate. For a fully depleted semiconductor with $n = p = 0$ the relevant generation rate can be found from equation 2.33 and is :

$$G_{th} = -U = \frac{N_t \nu_{th,n} \sigma_n \nu_{th,p} \sigma_p n_i}{\nu_{th,n} \sigma_n e^{\frac{E_t - E_i}{kT}} + \nu_{th,p} \sigma_p e^{\frac{E_i - E_t}{kT}}} \quad (2.37)$$

This leads to the generation lifetime τ_g , in a fully depleted indirect semiconductor, as :

$$\tau_g = \frac{n_i}{G_{th}} = \frac{1}{N_t} \left[\frac{1}{\nu_{th,p} \sigma_p} e^{\frac{E_t - E_i}{kT}} + \frac{1}{\nu_{th,n} \sigma_n} e^{\frac{E_i - E_t}{kT}} \right] \quad (2.38)$$

2.7 Carrier Transport with Generation and Recombination

The equations which unite all of the previous work are the continuity equations and Poisson's equation. The continuity equations can be described

2.7 Carrier Transport with Generation and Recombination

simply if the one-dimensional case is examined. If we have a volume of area A and thickness dx , then the movement of electrons through this volume can be described as :

$$\frac{\delta n}{\delta t} A dx = \Phi_n(x) A - \Phi_n(x + dx) A + (G_n - R_n) A dx \quad (2.39)$$

Here Φ_n is the electron flux, with G_n and R_n being the generation and recombination rates. This is shown schematically in figure 2.12 If $j_n = -q\phi_n$ substi-

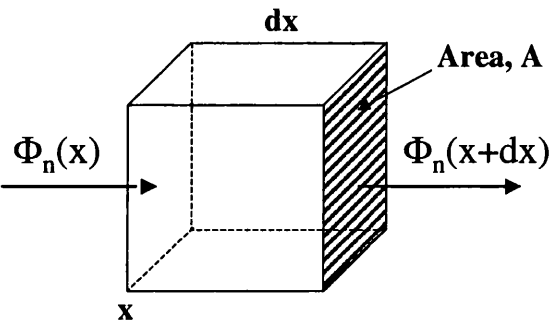


Figure 2.12: Carrier flow with generation and recombination
(After Lutz 1999, p.35 Fig. 2.20).

tutes the flux term and the situation is generalised to the three-dimensional case, the continuity equations are found, and shown below in (2.40) for electrons and holes respectively.

$$\begin{aligned} \frac{\delta n}{\delta t} &= \frac{1}{q} \nabla J_n + G_n - R_n \\ \frac{\delta p}{\delta t} &= -\frac{1}{q} \nabla J_p + G_p - R_p \end{aligned} \quad (2.40)$$

Incorporating equations 2.14 and 2.15, all of the contributions can be more clearly seen.

$$\begin{aligned}\frac{\delta n}{\delta t} &= \mu_n n \nabla E + D_n \nabla^2 n + G_n - R_n \\ \frac{\delta p}{\delta t} &= -\mu_p p \nabla E + D_p \nabla^2 p + G_p - R_p\end{aligned}\tag{2.41}$$

The first term is due to drift, the second arises due to diffusion the third is the generation term with the last being the recombination contribution. The final equation which is of relevance is Poisson's equation. It relates the electric field to the space charge distribution as follows:

$$\nabla E = \frac{\rho}{\epsilon \epsilon_0}\tag{2.42}$$

where $\rho = q(p - n + N_D - N_A + \sum_i N_{t_i} f_i) - \rho_s$ and is the space charge density. The $\sum_i N_{t_i} f_i$ term is the trap concentration for the i th energy level, while surface charge effects are accounted for by the ρ_s term. The continuity equation and Poisson's equation form the starting equations for device analysis using modelling packages. They follow from Maxwell's equations and their derivation from these fundamental equations is shown in Selberherr [21].

Chapter 3

Particle Interactions and Detection Techniques

3.1 Introduction

Semiconductor radiation detectors have found application in many fields. They are used as imaging tools in medicine, as particle detectors in high energy physics and as spectroscopic devices in industry. Their wide ranging applicability is due in part to their fast response, high efficiency and impressive spatial resolution. These traits are a result of a combination of fundamental semiconductor properties, material development and continued improvement in electronic design. This chapter will examine the important aspects of detector physics. It can be split broadly into two parts - particle interactions and detector principles. The starting point is the basics of particle interactions in semiconducting materials. The intention is to introduce the physics contained within the Monte-Carlo code MCNP, without going into the specifics of the code (appendix A briefly outlines the Monte-Carlo

method).

With these principles asserted the focus will move to the three main detection materials for pixellated devices, namely silicon, GaAs and CdTe/CdZnTe. Signal generation and carrier transport is also included for completeness and the chapter ends with a discussion of current highly pixellated devices.

Many of the topics discussed here are covered more broadly in books such as G. F. Knoll's "Radiation Detection and Measurement" [22] and "Semiconductor Radiation Detectors" by G. Lutz [19].

3.2 Particle Interactions in a semiconducting material

The response of a detector is dictated by the manner in which the incident radiation interacts with the detection material. This radiation can be classified into two categories :

- Charged radiations (such as alpha particles and fast electrons) - whereby the particles interact via the Coulomb force.
- Uncharged radiations (neutrons and X/ γ rays) - where the radiations undergo a partial or complete transfer of energy to the nuclei or electrons of the detection material.

These two classes of interactions are not distinct and sometimes one will result from the other. For example, neutron detection is sometimes accomplished by coating the semiconductor with a material which will produce secondary charged particles. The semiconductor will then detect the result-

3.2 Particle Interactions in a semiconducting material

ing recoil charged particle. X and γ -rays also liberate secondary electrons whose interactions are closely linked to those of a beta particle.

3.2.1 The interaction of X and γ rays

Three principle types of interactions that are prevalent when the interaction of photons is considered. These are :

- the photo-electric effect
- Compton scattering
- pair production.

This thesis will concentrate on the interaction of photons whose energy is usually between 10 and 100 keV, though some cases where the incident energy is above 600 keV will also be considered. Of the three effects listed above, the dominant process over these energies is the photo-electric effect and so it will form the largest section. However Compton scattering becomes significant when the energies rise above 70 keV in the materials considered. Pair production is an interaction mechanism that can be ignored since in these materials it only becomes relevant when the photon energies are above ~ 5 MeV. The relationship between the interaction cross-sections at a given incident photon energy and the Z of the absorber is shown schematically in figure 3.1.

The Photo-electric effect

The photoelectric effect was first postulated by Einstein to account for the emission of electrons from the surface of a metal after illumination by light.

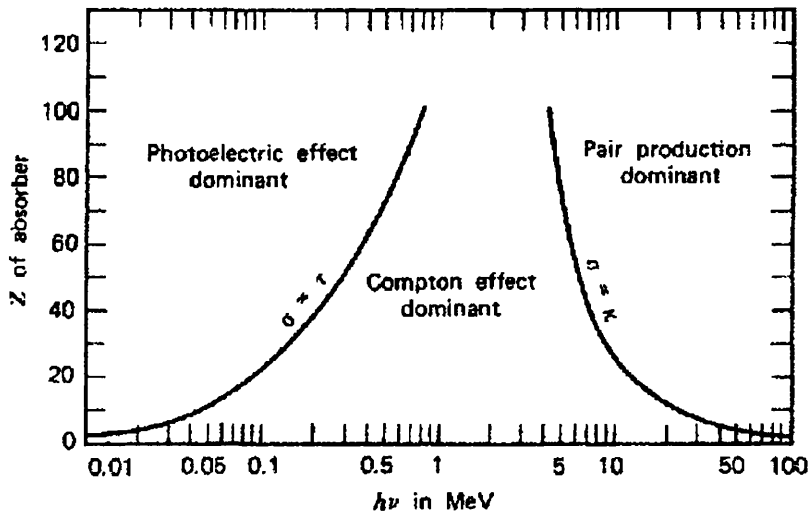


Figure 3.1: The dominant processes for photon interactions
(After Knoll 1989, p. 54, Fig. 2-20).

He described how the photon could be considered as a quantum of light and how each particular material surface has a work function equal to the amount of energy needed to liberate an electron. For the energy ranges relevant here the work function can be considered negligible and the interactions with electrons in the inner orbital shells become important. Since it is impossible for a photon to be absorbed by a free electron (it can only be scattered) the most probable interactions are with the tightest bound electron, located in the K-shell. X-ray detection in materials such as Si, GaAs and CdZnTe is therefore described by the following steps, for the energy range 0 - 100 keV. Figure 3.2 shows diagrammatically the interaction process.

The incident X-ray

3.2 Particle Interactions in a semiconducting material

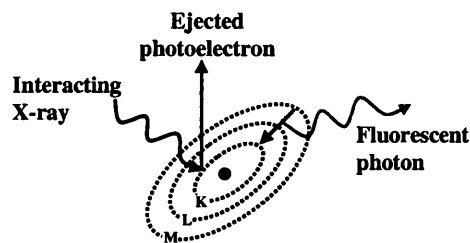


Figure 3.2
Schematic showing an X-ray interaction and the subsequent processes.

Photon interactions are localized, so when they pass through a medium, photons will traverse a certain distance unaffected, until depositing energy by photoelectric absorption. The probability of undergoing an interaction is an exponential function of distance. The fraction of photons that suffer this interaction, after traversing a distance x , is $f = 1 - e^{-\mu x}$ where μ is a linear absorption coefficient, (usually expressed in cm^{-1}). This absorption coefficient is equal to the product of the photoelectric cross section (σ) and the number of atoms per unit volume (n). The absorption can be parameterized more generally by the mass attenuation coefficient μ/ρ , expressed in cm^2g^{-1} , since the cross section is independent of the density or physical state of the absorber.

The photoelectron

The X-ray interacts with an atom in the lattice and liberates a photoelectron, with an energy given by $E_{\text{photoelectron}} = E_{\gamma} - E_{\text{binding}}$, where E_{γ} is the energy of the incident photon and E_{binding} is the binding energy of the electron with

its associated atom. The photoelectron then undergoes multiple scattering in the surrounding material where it loses energy by 2 principal processes. One is electron-phonon scattering where the electron scatters off a lattice ion which is oscillating, due to its thermal energy, around its zero energy point. The other process occurs when the photoelectron collides with an electron in the valence band and excites it over the forbidden band, creating an electron-hole pair in the process.

The direction of emission of the photoelectron is predominantly at right angles to the incident photon, and in the main is determined by the direction of the electric field in the incident radiation. However at higher photon energies the photoelectron acquires a forward component of momentum as required by conservation of momentum.

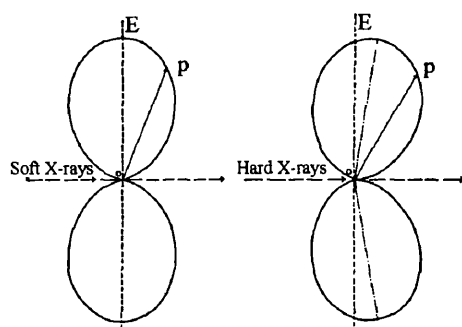


Figure 3.3

The angular dependence of photoelectrons for soft and hard X-rays. The circular shapes indicate the probability of photoelectron emission at that angle (After Compton and Allison 1949, p. 576, Fig. VII-25).

Fluorescent photons and Auger electrons

3.2 Particle Interactions in a semiconducting material

The emission of the photoelectron results in a space being left behind in the electron orbital in which the absorption process occurred. The subsequent rearrangement of the orbital electrons results in the release of energy as an electron from a more loosely bound orbital “falls down” to replace the photoelectron. The resultant energy can appear in two ways; through the emission of a fluorescent (characteristic) photon or through the emission of a less tightly bound Auger electron.

The fluorescence photons are emitted isotropically with an energy equal to the difference in binding energy of the photoelectron and its replacement. There will also be some residual energy left which is dissipated by further Auger processes.

The Compton Effect

Another process which becomes important at higher energies, and is still relevant for the energies discussed here, is the Compton effect. This can be considered in terms of the incident photon scattering off a free electron, taking into account the conservation of momentum. It is an illustration of the particulate nature of photons, since Compton started from the assumption that photons had the mechanical property of momentum.

Here we consider the mechanism whereby the incident X-ray scatters off of a free electron, transferring some momentum in the process. The electron can be considered free since most interactions of this type are with the outer electron orbitals. The energy of the scattered photon, $h\nu'$, is given by :

$$h\nu' = \frac{h\nu}{1 + \frac{h\nu}{m_0c^2}(1 - \cos\theta)} \quad (3.1)$$

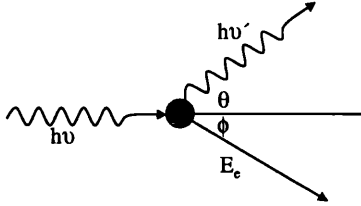


Figure 3.4

The Compton scattering effect.

where $h\nu$ is the energy of the incident photon, m_o is the mass of the electron and the other terms are shown in figure 3.4.

Pair Production

At higher energies (above $2m_o c^2$) γ -rays can interact in a third way. This entails the absorption of a photon and the creation of an electron-positron pair. It can be explained by the Dirac theory, where a continuum of electrons with negative energy states is assumed at an energy of $< -m_o c^2$. The more familiar positive energy levels occur at $> m_o c^2$. Thus, in order for the antiparticle pair to be created, a gap of energy $2m_o c^2$ has to be bridged. When this energy has been supplied to the material an electron appears and the corresponding hole in the negative continuum, which has the same properties as the electron with the exception of the charge, is called a positron. For a more detailed description of pair production see [23].

3.2.2 Electron interactions

The total path length travelled by an electron during the slowing down process is known as the integrated path length. This distance is appreciably shorter than the distance the electron will travel from its creation point to

3.2 Particle Interactions in a semiconducting material

its resting point, due to the multiple scattering of the electron as it undergoes the Coulomb interactions which characterise its energy loss. In most cases the distance travelled by the electron in a material is found by the continuous slowing down approximation (CSDA). This takes the integral over energy of the stopping power from a final to an initial value. The other range value which is perhaps of more relevance here, is the extrapolated range. If a source of electrons was placed in front of a thin absorber and the thickness of the absorber increased, then the thickness at which the rate of change of transmitted electrons is at a maximum would be the extrapolated range. This is a more useful number for the range of an electron in a material since it is closer to the average distance travelled from the electron creation point to its rest point. These two quantities are graphed in figure 3.5 over the relevant energy range (0 - 100 keV). It should be noted that at these energies, which

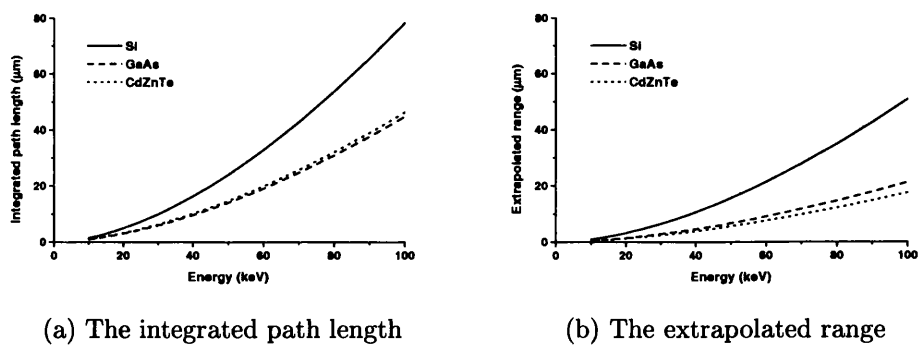


Figure 3.5: Electron ranges in silicon, gallium arsenide and cadmium zinc telluride. Calculated using the ESTAR database (available from <http://physics.nist.gov/PhysRefData/>).

are relatively low compared to most common cases cited in the literature, there are significant errors in the range values [24]. The values quoted here are intended to give an approximate value for the range of the photoelectron over these energies and are not intended to be precise. For more accurate ranges Monte Carlo Methods such as those employed in MCNP are applicable. Though the methods are more advanced the same initial principles, such as the CSDA technique, are employed. For a more comprehensive account of electron transport in MCNP see [25].

3.2.3 Charge particle interactions

The interactions of a charged particle as it passes through a material were first described classically by Bohr. Later Bethe, Bloch and Landau outlined more comprehensive quantum mechanical theories.

The most probable interaction, and the dominant one where detectors are concerned, is between the charged particle and the material's orbital electrons. When the particle enters the detection medium it simultaneously interacts with several electrons via the Coulomb force. The transfer of energy between the charged particle and the electrons leads to the electrons gaining energy and the charged particle slowing down. The electrons can either be raised into a higher orbital shell (leaving the atom in an excited state) or they can be removed completely from the atom creating an electron hole pair in a process known as ionisation. The particle is involved in many of these collisions and so is continuously slowing down until it comes to rest.

3.2 Particle Interactions in a semiconducting material

Stopping Power

The consequence of these interactions is that a charged particle of a given energy has a characteristic range in a particular material. The linear stopping power, S , of the absorber is defined as the differential energy loss (dE) divided by the differential path length (dx):

$$S = -\frac{dE}{dx} \quad (3.2)$$

This rate of energy loss over an incremental distance is given by :

$$-\frac{dE}{dx} = \frac{4\pi e^4 z^2}{m_0 v^2} NB \quad (3.3)$$

where v is the velocity of a particle of charge ze , interacting in an absorber which has a number density N and an atomic number Z . The electrons in this material have a charge e and a rest mass of m_o . B is given approximately as :

$$B = Z \left[\ln \frac{2m_0 v^2}{I} - \ln \left(1 - \frac{v^2}{c^2} \right) - \frac{v^2}{c^2} \right] \quad (3.4)$$

where c is the speed of light and I the average excitation and ionisation potential of the absorber. These equations are known as the Bethe-Bloch formula.

The Bragg Curve

The plot of specific energy loss along the track of a charged particle as it traverses the detection medium, is known as the Bragg curve. It illustrates graphically equation 3.3 and shows that charged particles lose energy in a manner differing from the previously discussed case of photons. Figure 3.6 shows the energy loss for a single alpha particle and a beam of particles. The

difference is due to energy straggling, which is an effect from the statistical nature of the interactions.

The specific energy loss curve for an electron is similar except that the curve

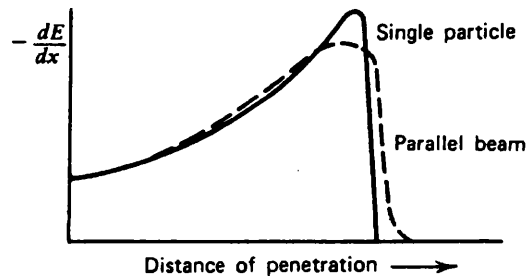


Figure 3.6: The Bragg curve for an alpha particle of several MeV initial energy (After Knoll 1989, p.33, Fig. 2-2).

follows the tortuous path of the electron as it multiple scatters through the detection material.

3.3 Detectors

The previous section outlined the interaction of radiation in materials. This section will focus on the properties of semiconductor detectors.

There are two broad modes of operation for the type of detector discussed here : integrating and individual quantum pulse (photon counting) mode.

3.3 Detectors

3.3.1 Integrating detectors

These detectors can be current or charge integrating. They find applications as imaging detectors and are useful for determining dose rates in radiation environments.

Current Integrating

A detector operating in the current integration mode would measure the direct current averaged over the response time of the device. The response time in some cases can be a significant fraction of a second. This leads to the possibility of many quanta of radiation being measured over one time period. The measured current at the output is then the sum of contributions from all the individual particles. The energy deposited per particle is therefore lost and spectral analysis is not possible. However the measured current in many cases is proportional to the rate of energy deposition and the absorbed dose rate can be determined. Imaging detectors can also be used in this mode and the following mode, where the image quality improves with integration time.

Charge Integrating

The induced current in a detector can be integrated across a capacitor to give the resultant charge over the measurement time. This allows measurements to be taken where the current is too small to be measured directly by the previous method. The integrated charge is a measurement of the total energy deposited in the detector over the integration time.

3.3.2 Individual quantum pulse mode

The photon counting method depends upon a detector coupled to a low noise charge-sensitive preamplifier. In this mode it is possible to detect each individual radiation quantum that has interacted in the detector volume. If the interacting particle deposits enough energy in the material such that the resultant voltage pulse is above a pre-set electronic *threshold*, then the information of the interaction is recorded. This threshold is usually placed at a position just above the inherent noise of the system.

Energy resolving detectors

Here the amplitude of the output voltage pulse from each individual interaction above the threshold is obtained. The magnitude of the pulse is proportional to the amount of energy deposited in the detector and is given by the following equation : $V = \frac{qE}{\epsilon C}$, where V is the magnitude of the output voltage pulse arising from the interaction of a particle of energy E, C is the detector capacitance, q the charge on the electron and ϵ is the mean energy per e-h pair. These individual pulses are then stored and displayed as a differential pulse height spectrum on a multichannel analyser. This method is employed in all spectroscopic detectors.

Photon counting

This technique is an alternative to the above method which has been used for imaging detectors. The pulse height is not recorded in this case, but a counter attached to the read-out electronics is incremented whenever the incident radiation created enough charge particles for the resultant pulse to be above

3.3 Detectors

the threshold. So only the fact that a particle, above a certain energy, has interacted in the detector is obtained. The position of the threshold in effect defines what energy an individual photon has to deposit to register a “hit”, so for low energy photon detection the noise of the system is crucial. The advantages of this type of detector configuration are speed of read-out (and so high rate capabilities) and the reduced complexity of the read-out electronics (and so a potentially smaller pixel size). An example of a pixel detector operating in this manner is the MEDIPIX system [26].

3.3.3 Metal semiconductor contacts

The extraction of charges from a semiconducting material is accomplished by means of electrical contacts. These are typically fabricated on opposite ends of the detection material and a potential difference applied between them. This potential difference leads to an internal electric field which separates the charge carriers resulting in an induced charge on the electrodes. These contacts therefore play a pivotal role in the characteristics of the detector. They can be either of two types: Ohmic or Schottky.

When a metal is brought into contact with a semiconductor the Fermi level of the two materials must align into an equilibrium state. This is illustrated in figure 3.7 where a metal of work function ϕ_m is brought into contact with an n-type semiconductor of work function, ϕ_s and electron affinity χ . The resultant band bending determines the contact characteristics.

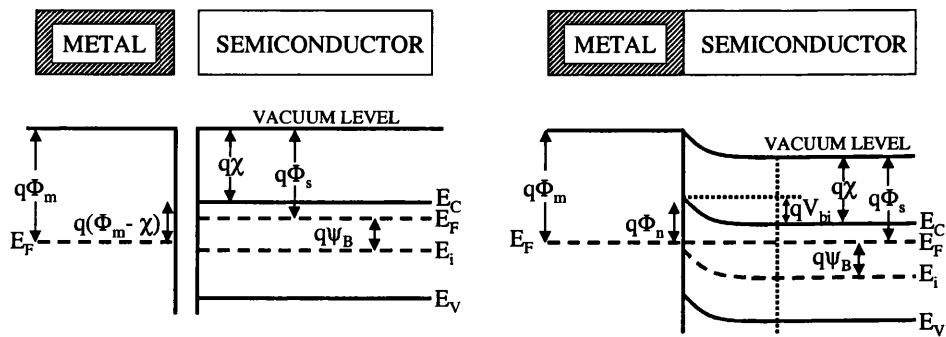


Figure 3.7: The metal semiconductor junction

The Schottky contact

A Schottky contact is formed because of the differences of work function between the metal and semiconductor. The work function of a material is defined as the difference between the vacuum level (the point at which a free electron can exist) and the Fermi level. In an n-type semiconductor the alignment of the Fermi levels is attained by the flow of electrons from the semiconductor to the metal. This leaves a region of space charge in the semiconductor adjacent to the semiconductor-metal interface. This positive space charge, composed of ionised donors, causes the band bending shown in figure 3.7 and sets up the potential barrier at the interface. For electrons to flow out of the semiconductor they now have to surmount a barrier, giving the contact useful current rectifying properties.

Conversely when a p-type semiconductor, with a work function greater than that of the metal, is brought into contact with this metal the resulting band bending is downwards. This forms a p-type Schottky contact which also possesses rectifying properties.

3.3 Detectors

The magnitude of the potential barrier is given by the following equation :

$$q\phi_b = q(\phi_m - \chi_s) \quad (3.5)$$

where ϕ_b is known as the barrier height of the contact.

The above statements hold for the idealised case, which often is not realised. More commonly there exists a high density of surface states which alter the properties of the contact. The surface states are trapped charge or defects that exist at the surface of the semiconductor. The equilibrium conditions, discussed above, are achieved in this case through charge transfer between the surface states and the metal. A small change in the Fermi level at the interface provides enough band bending to align the Fermi levels. This effect is known as the *pinning* of the semiconductor Fermi level at the surface due to these surface states. GaAs is a material whose Fermi level is thought to be pinned at the mid-gap point due to the presence of deep traps at the surface. The pinning of the Fermi level makes the alteration of the barrier height difficult and acquiring the desired contact properties becomes complex.

The Ohmic contact

The other type of contact is one which has a negligible resistance to current flow. It is therefore known as an injecting or ohmic contact. The contact resistance is low in comparison with the resistance of the bulk material. This means that there is no voltage drop across the contact and there is little or no power dissipated on the contact. Thermal equilibrium is maintained even when current is flowing across the electrode, resulting in no change in the free carrier density at the ohmic contact. For ohmic conditions to be met the work function of the metal must be less than the work function of the

semiconductor, for n-type material. The converse is true for p-type semiconductors.

Problems arise when fabricating such contacts onto room temperature semiconductors. The presence of high densities of surface states in these materials cause the Fermi level to be pinned, also the large band gaps mean that metals with small enough work functions are hard to come by. These difficulties mean that other steps are sometimes used to realise ohmic contacts on these materials. One method is by the shallow doping of the semiconductor, which creates a thin Schottky contact. If this layer is thin enough the carrier can tunnel directly through the barrier, forming what is known as a tunnelling ohmic contact.

3.3.4 Photoconductive detectors

This is perhaps the simplest method of forming a semiconductor detector. Ohmic contacts are formed on either side of a block of semiconducting material. A voltage difference is placed across the detector which creates a current of a magnitude defined by the resistivity of the material. The interaction of ionising radiation changes the free carrier concentration and so the current flowing through the detector is increased by an amount proportional to the deposited energy. For these detectors to be operated in individual quantum pulse mode the resistivity of the detection material must be sufficiently high to ensure that the leakage currents are low enough, such that the charge generated by an individual particle is observable above this leakage current. An additional stipulation is that the mobilities, and lifetimes, of the carriers must be high to allow efficient extraction. An example of such a detector is

3.3 Detectors

CdZnTe which will be discussed later in chapter 7.

These detectors can also be used in photoconductive gain mode, where the gain, G , is defined by the ratio of the photocurrent, I_p , to the primary photocurrent, I_{ph} e.g. $G = \frac{I_p}{I_{ph}}$. The gain occurs because the semiconductor has not returned to its equilibrium condition, by the time another photon interacts. The gain can therefore be expressed in terms of carrier lifetimes, τ , and transit times, t_r , and is simply the ratio of these two variables. Gains as high as 10^6 can be obtained from some photoconductors and typical response times range from 10^{-3} to 10^{-10} seconds. Detectors of this type are commonly used for infrared detection.

3.3.5 Diode detectors

A more complex detection method, in terms of fabrication, uses diode detectors. These can be realised by two methods. The first to be discussed will be the p-n junction diode, the alternative being the Schottky diode detector.

The p-n junction as a detector

The p-n junction plays a prominent role in a wide variety of detectors. In its simplest form it can still act as a detector of charged particles and electromagnetic radiation. More complex detectors can still be well understood from the basic principles of the abrupt p-n junction.

The concepts of n and p doping were introduced in chapter 2 section 2.4.1, and are relevant to the following discussion. When n-type and p-type semiconductors are brought into contact, the majority carriers will diffuse out into the areas of lower concentration. This means that the electrons will

diffuse into the p-type material and the holes will move into the n-type material. The areas which have been vacated by their mobile charge carriers are now areas of fixed space charge - positive donors in the n-type material and negative acceptors in the p-type material. This space charge sets up an electric field which further opposes the diffusion of the carriers through the drifting of the charges. The material quickly attains an equilibrium condition where a region depleted of mobile carriers exists at the interface between the two materials. This region is known as the *depletion region* and the resultant potential difference across this region is commonly called the built-in voltage (V_{bi}). The depleted volume will remain free of mobile carriers even though carriers are being excited over the band gap. This thermal process is slow, around 10^{-3} to 10^{-4} seconds, in comparison with the non-equilibrium charge extraction times, typically 1 to 10 ns. The equilibrium concentration of free carriers is suppressed approximately by the ratio of these two times. Short carrier lifetimes lead to increased thermal excitation in this region which could be problematic in some materials. This simple p-n junction forms a rectifying diode which minimises the injection of a leakage current, and allows good charge collection over the depletion region.

Poisson's equation (2.42) can be used to calculate the width, $W(V)$, of this depletion region for the special case of an abrupt junction where the dopants are fully ionised and uniform in distribution. The expression is shown in equation 3.6 :

$$W(V) = \sqrt{\frac{2\epsilon_s}{q} \left(\frac{N_a^- + N_d^+}{N_a^- N_d^+} \right) (V_{bi} - V)} \quad (3.6)$$

where ϵ_s is the dielectric constant of the material, N_a^- and N_d^+ are the ionised acceptor and donor concentrations respectively. V is the applied external

3.3 Detectors

voltage and can be used to increase (apply a positive voltage to the electrode in contact with the n-side, or negative to the p-side) or decrease (converse of previous case) the space charge region. The equation is simplified when one side of the junction has a doping concentration far in excess of the other side and becomes :

$$W(V) = \sqrt{\frac{2\epsilon_s}{q} \left(\frac{V_{bi} - V}{N_b} \right)} \quad (3.7)$$

where N_b is the ionised concentration of the lesser doped side. These two equations show that large depletion regions, which are desirable for particle detection, require either large bias voltages or low doping concentrations. This limits the applicability of p-n junctions to the detection of ionising radiation, since the high electric fields required to maximise the depletion region exceed the breakdown voltages discussed previously in chapter 2 subsection 2.6.3. This problem is circumvented by introducing a region of intrinsic material between the p and n materials. The active area of the detector is increased and the operation voltages required for full depletion are lowered in the process. The intrinsic layer is more commonly n-type material with a low free carrier concentration, as it aids the processing steps. In figure 3.8 the cross-section of a typical silicon pixel (or strip) is shown, along with the band structure. This plot was obtained using the MEDICI simulation package where the doping densities were 10^{18} cm^{-3} for the n+ layer, 10^{19} cm^{-3} for the p+ and 10^{12} cm^{-3} for the n layer.

The Schottky diode

A Schottky diode is realised by applying to a semiconductor a contact of the type discussed in section 3.3.3. Since this contact is rectifying under reverse

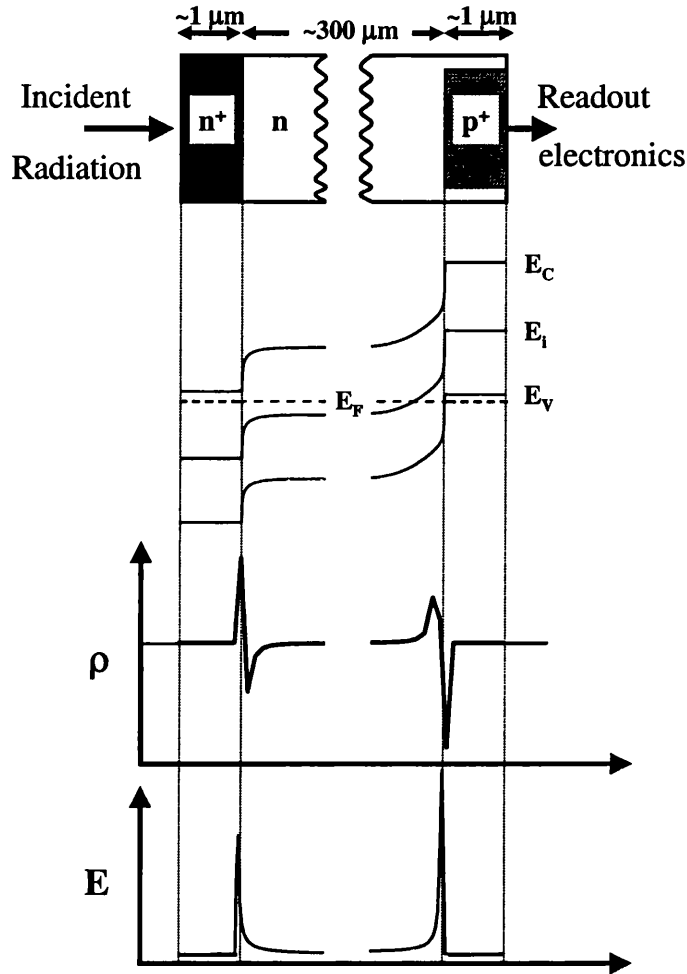


Figure 3.8: The properties of a diode detector in equilibrium.

bias, the contact blocks the flow of current across it. Ideally this results in a low leakage current. The depletion region which extends from the reverse biased Schottky contact is described by the following equation :

$$W(V) = \sqrt{\frac{2\epsilon_s}{qN_{dom}} \left(V_{bi} - V - \frac{kT}{q} \right)} \quad (3.8)$$

3.3 Detectors

where N_{dom} is the dominant dopant in the material and the $\frac{kT}{q}$ term accounts for the majority carrier distribution tail. The barrier height, which defines the characteristics of the junction, can be much lower for a Schottky diode than for a p-n junction diode, resulting in higher thermionic leakage currents. Surface states can also increase the leakage current by allowing tunnelling through to the conduction band. This method of fabricating detectors has the advantage of the comparative ease through which they are fabricated. They find use on materials which are difficult to process at the elevated temperatures required for dopant diffusion or implantation.

3.3.6 Materials

Many materials have been investigated for application as semiconductor radiation detectors, among them germanium, silicon, GaAs and Cd(Zn)Te, as well as more exotic alternatives such as SiC, GaN and InP. This short section will briefly outline the properties of the three materials (silicon, GaAs and CdZnTe) important to this thesis. The specifics of these materials will be covered in later chapters.

The motivation for moving from silicon, which is the dominant material in terms of semiconductor pixel detectors, can be seen in figure 3.9. Though silicon out performs the other materials when its charge transport properties are considered, its low atomic number leads to an absorption efficiency which drops off to 50% at 15 keV and is at the few percent level at 60 keV. For X-ray detection over this range it is desirable either to move to thick layers of silicon or to move to a material with a higher absorption coefficient. GaAs and CdZnTe are two such materials though they both suffer from defect related

charge transport problems. The thicknesses of the three materials shown in

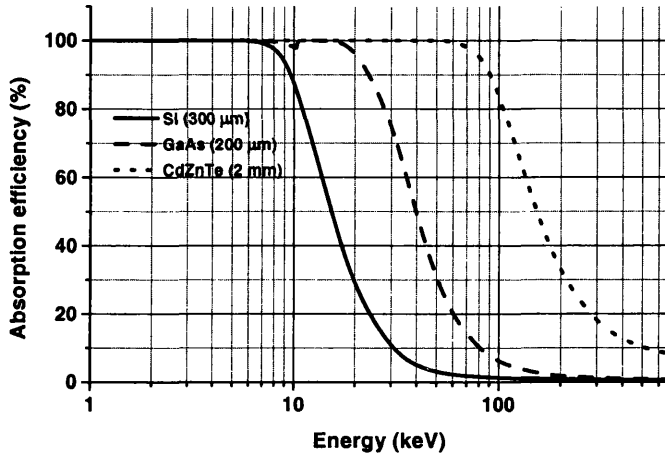


Figure 3.9: The absorption efficiencies of Si, GaAs and CdZnTe for common detector thicknesses.

figure 3.9 have been selected since they are the common thicknesses for these materials when used as radiation detectors. These absorption efficiencies have been calculated using the formula from subsection 3.2.1 and the absorption coefficients are taken from the NIST databases¹. The Monte-Carlo code MCNP uses the same cross-section databases as NIST database and so the figure 3.9 offers a accurate representation of how MCNP models these materials.

Silicon

For the applications discussed in this work silicon remains the benchmark detection material. Its technological development far exceeds the other ma-

¹Available from <http://physics.nist.gov/PhysRefData/>

3.3 Detectors

terials, and it has the advantage of being an intrinsic semiconductor. Appendix B covers the important properties of silicon. The major advantages of silicon are :

- The material is well understood and in common use.
- The fabrication processes are highly developed and widely available in industry.
- Full collection of generated carriers, at modest operating voltages, can be expected for the majority of applications.

The primary disadvantage of silicon is its low atomic number, as discussed previously.

Gallium Arsenide

GaAs is a material which, in theory, has all of the required semiconductor properties that are necessary for a room temperature semiconductor radiation detector. An optimum value for the band gap of such a detector exists due to the conflict between minimising the thermal generation of carriers and maximising the number of carriers created when a quantum of radiation is absorbed. This optimum value is around 1.4 - 1.5 eV, for which GaAs ($E_g=1.424$ eV) is well suited. An ideal material should have a high atomic number (to increase the γ -ray interaction probability) and GaAs, with $Z=32$ and 34, satisfies this criterion also. The high mobilities of the carriers in comparison with silicon are also an advantage. The reduced lifetime of the charge carriers, due to imperfections in the lattice structure, is where the

problems arise, in terms of detector performance. The reproducibility of detector response and the variations in material properties also cause significant problems. For a review of the status of GaAs as a detector medium, and the significant results over the last 40 years, see reference [27].

Epitaxial GaAs

These detectors were the first compound semiconductors to demonstrate good energy resolution at room temperature [28]. The material is commonly grown by liquid phase epitaxy (LPE) [29] or vapour phase epitaxy (VPE) [30]. These methods create relatively pure materials but are limited to thin detection layers - around 200 μm thick. Typically Schottky contacts are formed on one side of the detector with ohmic electrodes on the other side creating a diode detector. Detectors of this type have been shown to be effective X-ray imagers in the low energy X-ray regime [4], and have been proposed as a detection layer for dental imaging [31]. They also have a potential application for synchrotron radiation studies and some preliminary studies and are described in references [32] and [33]. The problems that exist here are the expense of both the detection layer and the read-out electronics. They are also currently available only as single chip detectors, with an active area of 1 cm^2 , though detector systems which allow the single chip elements to be arrayed are now planned [34]. Another difficulty is growing pure materials with low free carrier concentrations, such that they are fully depleted at reasonable operating voltages. This problem could be addressed by new detector designs, and one such design (first proposed by Sherwood Parker et. al. [35] for silicon detector operation in high radiation environments) is discussed in chapter 6.

3.3 Detectors

Semi-Insulating GaAs

Semi-insulating (SI) or bulk GaAs was proposed as an alternative to epitaxial detectors, since obtaining thick detection layers of this type of material is routinely performed in industry. This material however is not as pure as its epitaxially grown counterpart. The presence of high concentrations (10^{16} cm^{-3} [36]) of a deep donor level known as EL2, severely affects the charge transport properties. This defect has been attributed to an arsenic anti-site; an arsenic atom occupying a lattice site which should contain a gallium atom [37]. The defect is an electron trap and lies close to the midgap point. Bulk GaAs has also been reported to exhibit depletion properties which do not follow those expected from equation 3.6. This has been attributed to the field enhanced capture cross section of the EL2 trap [38]. Here it is postulated that as the electric field rises above 10^4 V/cm the capture cross section of the EL2 level increases. This means that the probability of the EL2 centre being occupied is high in the areas where the electric field is above this value. Since the EL2 is the dominant space charge in the material, the areas with $E > 10^4 \text{ V/cm}$ become compensated and the region exhibits the properties of an intrinsic semiconductor (the material has been observed to deplete at a constant rate of $\sim 1 \text{ V}/\mu\text{m}$). The areas with $E < 10^4 \text{ V/cm}$ still have the EL2 space charge and so as the detector depletes the space charge moves through the detector. This model has been supported by experimentally measured electric field profiles [39], though there are still concerns about the methods of measuring the internal electric field of the detector and the reproducibility of results. The implications of this model are that in order to deplete SI-GaAs the electric field has to rise above 10^4 V/cm . As it does so the probability of

trapping the generated charge increases, so large active volumes are associated with the reduced collection efficiency of the carriers. The reverse biased leakage current densities of bulk GaAs detectors range from 2.5 nA/mm² to 100 nA/mm² [36], [31] and [27].

Cadmium Zinc Telluride

Another bulk material that has found applications as a radiation detector is cadmium zinc telluride (CdZnTe). It is not commonly operated in diode form, but instead operates in photoconductive mode. The material properties and detector configurations are covered in detail in chapter 7. Its high average atomic number (average $Z=50$) has led to interest in the field of high energy gamma-ray detection. Detection layers are typically 2 mm thick with gold electrodes forming ohmic contacts. This material also suffers from purity problems and material uniformity. Energy resolutions of 2 % at 662 keV have been reported [40] in detectors which employ an interaction depth correction.

3.3.7 Aspects of charge transport

The signal from a detector arises not from the collection of charges but from the motion of charge. As soon as a charge packet is created by incident radiation, the positive and negative charges begin to separate. The result is an immediate pulse on the detection electrodes. This is known as the induced charge. There exists no delay in the rise of the current on the contact. When the last of the charges has been collected at the electrode then the induction process is at an end and the pulse is fully developed.

3.3 Detectors

Maxwell's equations and the Shockley-Ramo theorem

The weighting field and Ramo's Theorem

A general method to calculate the induced charge in a semiconductor detector is the Shockley-Ramo's theorem [41], [42], [43]. This theorem makes use of concepts such as the weighting field and the weighting potential. It states that the instantaneous current seen on an electrode is given by :

$$i = q\vec{v} \cdot \vec{E}_0 \quad (3.9)$$

where q is the charge on the carrier, \vec{v} is its velocity and \vec{E}_0 is the weighting field. A more intuitive way of representing this is to say that the induced charge is equal to the product of the charge on the carrier and the difference in the weighting potential, ϕ_0 , from the beginning of the charge carrier's path to its end, i.e.

$$Q = q\Delta\phi_0 \quad (3.10)$$

This simple equation can offer a deep insight into a detector's behaviour. The important parameter is clearly the weighting potential. This can be found by use of the following assumptions :

- The voltage on the detection electrode is set to unity
- All other electrodes are fixed at zero volts.
- Laplace's equation is used and so no fixed space charges (including trapped charges) are considered.

Solving for these conditions gives the weighting potential for a particular electrode. The weighting field is the negative gradient of this. These simplifications yield a useful method for determining the shape of the output

pulse due to the charge carriers. The weighting fields and potentials are not the actual electric equivalents, but instead serve as a convenience for this model. The validity of this approach in the context of semiconductor pixel detectors is shown in reference [44]. However to account fully for all aspects of semiconductor charge transport, the more advanced methods employed by device modelling packages are required.

The displacement current approach

Commercial modelling packages such as MEDICI solve Poisson's equation and so the electrical aspects of Maxwell's equations. To account for charge flow in this way it is necessary to introduce another current known as the displacement current. This was first postulated by Maxwell to account for discrepancies in Ampere's current law.

When a voltage is applied to a dielectric there will be an immediate, and small, movement of charge as the external electric field distorts the atoms of the material. The positive and negative bound charges of the atom move to opposite sides and the atom becomes *polarised*. This displacement of charge, which disappears on removal of the field, is known as polarisation, P . This movement of charge can be more broadly described as the displacement, D given as :

$$D = \epsilon_0 E + P \quad (3.11)$$

Since there is a motion of charge it will give rise to a current and this is known as the displacement current, I_d . The current is given by :

$$I_d = \frac{\delta D}{\delta t} = \epsilon \frac{\delta E}{\delta t} \quad (3.12)$$

3.3 Detectors

This current must be added to the conduction currents given previously in chapter 2 section 2.5.3 to account accurately for the total current in open loop circuits.

It is not just a voltage change that will cause this current induction, the creation of charges in the material will also disrupt the electrodynamics and so result in the flow of current. Figure 3.10 shows this process schematically. Here the effect that two identical charges will have on the atoms of a dielectric can be seen.

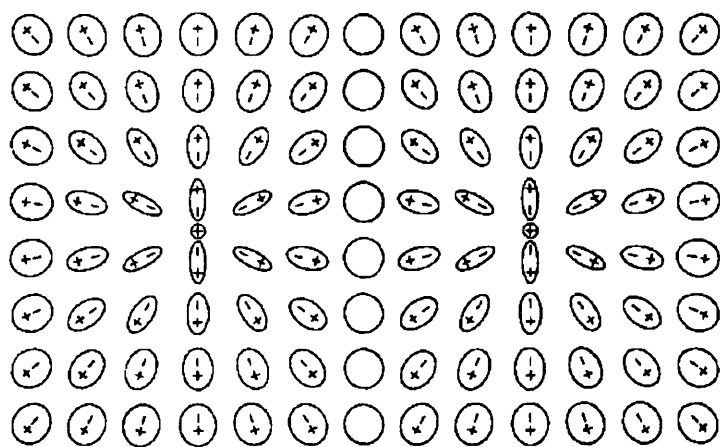


Figure 3.10: Polarisation of the atoms of a dielectric by a pair of equal positive charges (After Ramo, Whinnery, Van Duzer 1994, p. 7 Fig. 1.3c).

This approach to charge transport in semiconductors is more fundamental than the Shockley-Ramo approach. Additionally, since Poisson’s equation is solved rather than Laplace’s, the effects of trapped charge and surface states, which are thought to affect the charge transport significantly, can be accounted for. The specifics of the current and charge pulses from this

approach will be analysed later on in chapter 7.

3.3.8 Position sensitive semiconductor detectors

The focus of this thesis is on position sensitive semiconductor detectors and in particular pixel detectors. The theoretical framework outlined previously holds for detectors, however the following subsection will discuss more specific aspects of these detectors.

Pixel detectors

Hybrid pixel detectors

These systems consist of a 2 dimensional array of detection elements coupled to geometrically matching readout electronics, via a bump-bond interconnect. The readout electronics are processed on a separate wafer from the detector which allows both technologies to progress at their own rate of development. The readout electronics, for example, are commonly fabricated on silicon in standard industrial processes (to minimise the expense and ensure the readout array has a high operation yield), whereas a choice of detection medium can be selected to fit a specific application, for example a high atomic number material for higher energy X-rays.

Since each pixel element has its own dedicated front-end readout electronics, these detectors are ideally suited to operation in a high rate environment. This explains why detectors of this type were first developed for high energy physics applications. They may also find application as high rate imaging sensors, of the type needed for the new synchrotron sources (for example DIAMOND). Since the electronics can be fabricated in well understood, reli-

3.3 Detectors

able industrial processes the choice of detector medium may lend the detector system to biological and medical applications.

This type of pixel detector is, however, limited by potentially unreliable bump bonding and the high cost of fabrication. Furthermore the added bonus of choice of detector medium is somewhat negated by the problems with material quality discussed previously. Additionally the defining quantity of spatial resolution, related to the pixel size, is governed by several factors, primarily the complexity of the front end electronics, the size of the bump bond and to some extent the physical processes involved in particle detection.

CCDs

Charge coupled detectors, or CCDs, have been the benchmark detectors as far as the imaging of photons is concerned. These detectors have their limitations but, just as silicon has remained the dominant detector medium, CCDs have yet to be improved upon in terms of reliability and imaging resolution. They have found applications in many areas of science and medicine, such as vertex detection and X-ray imaging, and have been incorporated into commercial systems such as video cameras.

CCDs store any generated charge in potential wells within a space-charge region. The charge packets in these potential wells are then transferred sequentially by suitable clock pulses along the pixellated array toward the read-out electronics. These pockets of charge can fill up with thermally generated carriers, leading to some restrictions on the operating conditions of the devices (discussed later). Since the pockets of charge are conventionally read out to the bottom of their column and then to the end of their row, only one pre-amplifier is needed for the whole array. This leads to an extremely

low-noise performance when the pre-amplifier is integrated onto the detection wafer, but to a relatively slow (\sim msec) frame readout time.

Monolithic pixel detectors

In these detectors each pixel has its own readout electronics which are integrated onto the sensing element. This has the possibility of creating an extremely low noise device capable of 2-D imaging in high rate environments. The fact that the readout chain has to be fabricated on high resistivity detector grade material leads to the primary disadvantage of these detectors. The transistors and readout circuits have to be manufactured in non-standard technologies. This leads to a large increase in the cost of development and fabrication. However the potential advantages (low noise, less components and a very thin structure) are such that many groups have pursued their fabrication, for example [45]. Should standard CMOS fabrication techniques be possible for these detectors then in some situations they could offer a viable alternative to CCDs and hybrid pixel sensors.

Chapter 4

The detector systems - ERD1 and Dash-E

4.1 Introduction

This chapter will introduce the ERD1 detector and its successor the Dash-E detector. Both systems have undergone characterisation with the aim of understanding their behaviour, so that a successful comparison with the models developed in later chapters can be drawn.

The development of these detectors was funded, through the IMPACT (*Innovative Microelectronic Pixellated Sensors and Advanced CCD Technology*) collaboration [46], by the Department of Trade and Industry through PPARC. The detector systems were designed by Paul Seller and his colleagues in the Microelectronics group at the Rutherford Appleton Laboratories and have been described in [47], [5] and [48].

4.2 Description of devices

The Energy Resolving Detector 1 (ERD1) is a hybrid active pixel detector intended for X-ray spectroscopy over the energy range 1 keV to 25 keV. The detection system consists of a 16×16 array of preamplifiers each coupled, via a bump bond, to a pixellated silicon detector. The silicon pixel detector matches the readout in that it has square pixels on a pitch of $300 \mu\text{m}$. Two thicknesses of silicon were fabricated to couple to the readout electronics - 300 and $500 \mu\text{m}$. The results presented here are for the $300 \mu\text{m}$ thick detector only. Figure 4.1 shows the detector system with the detector and secondary read-out stage highlighted.

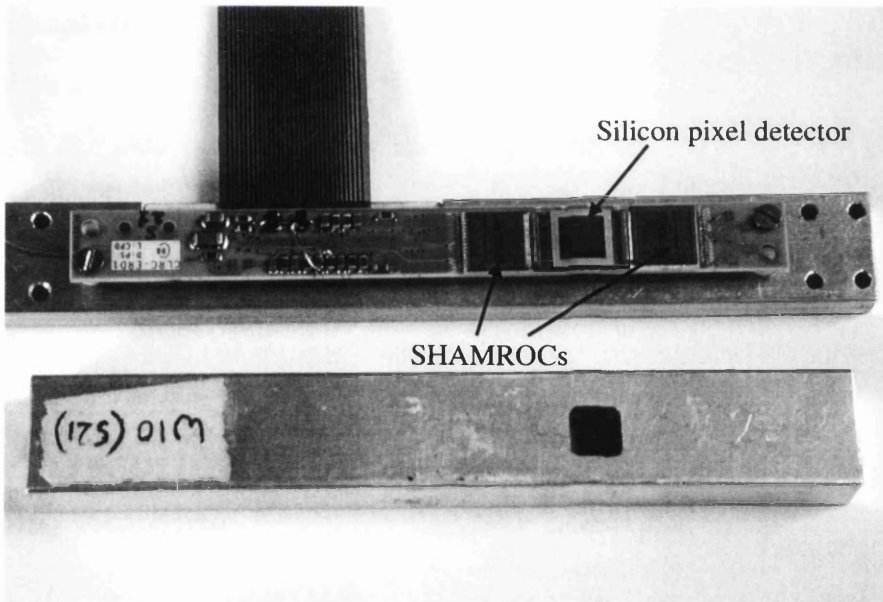


Figure 4.1: Photograph of the Energy Resolving Detector 1 with detector and read-out highlighted.

4.2 Description of devices

4.2.1 The detector

The ERD1 detector is a 16×16 matrix of square pixel elements of pitch $300 \mu\text{m}$. This gives an active area of $4.8 \text{ mm} \times 4.8 \text{ mm}$. The pixels were fabricated on 3-10 kohm-cm, n-type, 4 inch silicon wafers, with the silicon crystal lattice orientated in the $\langle 100 \rangle$ plane (the wafer plane is perpendicular to this axis). The fabrication was carried out at SINTEF [49] using double sided processing. The detector was been designed to be illuminated through the n^+ ($n^+ = 10^{18} \text{ cm}^{-3}$) ohmic contact. This layer is formed by ion-implanting phosphorus to a depth of $0.5 \mu\text{m}$, through a 200 nm thick oxide layer which remained for mechanical protection. A $0.5 \mu\text{m}$ thick coating of aluminium covers the edge of the active area to allow wire bonding out to the bias line. The p^+ boron implant ($280 \mu\text{m}$ square) on the bump bond side is covered with $1.5 \mu\text{m}$ aluminium and a polyimide passivation. A $170 \mu\text{m}$ square window is opened in the passivation to allow the bump bond to make electrical contact. The leakage current of the detectors is of the order of 0.3 pA per pixel (determined by I-V measurements) [47], with several guard ring structures to eliminate the effects of surface currents associated with irregularities on the sawn edges of the silicon [49].

4.2.2 Bump bonding

The detection elements are connected to readout electronics via a gold stud bump bond. The process starts by the PAC5 readout stage being sawn from its wafer into individual readout chips. The bump bonds are applied using a conventional gold bump bonder with the wire being broken at a controlled height above the ball. The result is a bond which is approximately

$50 \times 50 \mu\text{m}$ in size. The detector has zinc, nickel and gold layers applied to the aluminium covered p^+ side. These under bump metallisation layers protect the silicon detectors during the bonding process. The detector layer is then covered in a silver epoxy ($1 \mu\text{m}$ thick) aligned and placed upon the PAC5 chip. An insulating underfill is then inserted between the detector and preamplification chip to improve the mechanical strength. This method has the advantage of having close to 100 % bump bond yield, though the size of the bonds exceeds that required by many pixel detectors for imaging applications.

4.2.3 The read-out electronics

The readout electronics of the ERD1 is split into two parts : the preamplification stage performed by the PAC5 and the post-amplification stage performed by the SHAMROC chip.

Preamplifier chip (PAC5)

The PAC5 is an integrated circuit which has a 16×16 array of preamplifiers. These are geometrically matched to the detector pixels and coupled via the previously described bump bond process. The amplifier is of the charge sensitive type and utilises the folded cascode architecture. The schematic of the preamplifier is shown in figure 4.2 along with the line drivers. The input FET ($200 \mu\text{m} : 1.2 \mu\text{m}$) has a feedback capacitance of 100 fF and draws 100 μA . Adequate gain is achieved while pixel to pixel uniformity varies by 10 %. This non-uniformity has to be corrected by software and does not affect the energy resolution of the detector system [50]. The resets are transistor

4.2 Description of devices

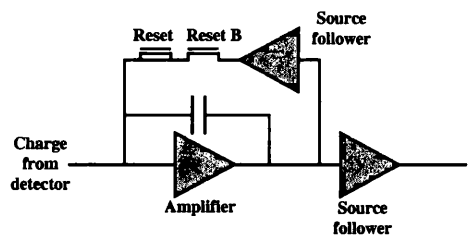


Figure 4.2

The preamplifier array chip (PAC5). The readout chain (left) is bump bonded to each individual pixel.

circuits with a 1Mohm stabilisation resistor. This requires the pre-amp to be reset every 100 ms and results in a 1 pA leakage current. Dummy transistors are used to cancel the reset charge injection.

The noise of the pre-amp has been designed to be 20 electrons RMS. This assumes a detector capacitance of 250 fF, a pad capacitance of 250 fF and a 10 pA leakage current when shaped by the 2 μ s shaper. All of the individual PAC5 pixels are routed to bond pads where they are wire bonded out to the secondary readout stage performed by the two SHAMROC chips. Both the PAC5 and the SHAMROC are fabricated in the Mietec 0.7 μ m CMOS process.

Secondary readout stage (SHAMROC)

The SHAMROC amplification stage consists of 128 CR-RC shapers, a peak-hold and comparator circuit. The schematic is shown in figure 4.3.

The PAC5 outputs a voltage signal to the SHAMROC where it is shaped by a 2 μ s CR-RC amplifier, which has a gain of around 40. This shaped pulse drives a circuit which holds the peak of the signal. If the peak is above a threshold (set by software) the comparator fires and provides a hit

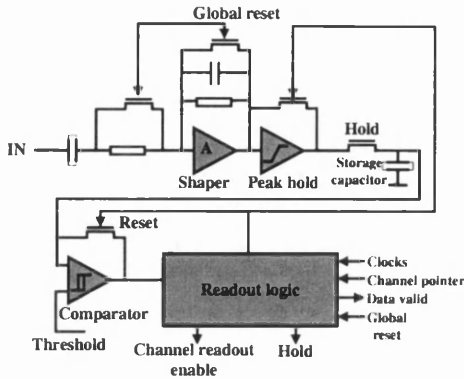


Figure 4.3

The secondary readout chain (SHAMROC) contains 128 channels. Two are wire bonded to each PAC5 chip.

signal to the readout logic. The minimum input voltage which will cause the comparator to fire is 5 mV. When a comparator fires, a flag is set in the readout logic. A clock is then enabled which applies a hold signal, after 3 clock counts, to the corresponding peak hold circuit to store the peak value. Only the ‘hit’ channel is affected by this procedure, which leaves the rest of the system free to continue taking data. The counter is clocked at 1 MHz so the readout signal is applied after 3 μ s. This hold signal will also raise a flag which traps a readout pointer when the channel is reached. When this happens the analogue multiplexer is enabled and the stored value is routed from the channel to the analogue output. The channel address and a ‘data valid’ signal are also output to indicate that the data is genuine.

The readout pointer scans through all 128 channels in the first SHAMROC before progressing to the second SHAMROC. The logic for the pointer is designed such that all channels with no data are skipped. A single channel readout cycle takes 1 μ s and the readout logic then applies a reset to the peak hold and comparator circuits of the channel and resets itself. The logic has to wait 20 μ s from the departure of the pointer to releasing the reset to the peak hold and comparators. This is to allow time for the tail of the shaped analogue signal to return to zero. Since the data are only available

4.3 Detector Characteristics

at the output while the pointer is present at the channel, the data acquisition system must sample the data in one cycle, i.e. $1\ \mu\text{s}$. This gives a channel readout rate of 1 MHz but if a channel is read out it then has a dead time of $20\ \mu\text{s}$.

The PAC5 and SHAMROCs are wire bonded to a ceramic board which can be seen in figure 4.1. The ceramic is double sided, is built with minimum features of $50\ \mu\text{m}$ wide copper tracks and contains some surface mounted filtering components. The detector and amplification stages are encased in a $10 \times 1 \times 1\ \text{cm}^3$ aluminium box, and the system is controlled under LabView by 2 PC interface cards.

4.3 Detector Characteristics

4.3.1 Linearity of Response

The linearity of the detector was tested by illumination with various characteristic X-ray line sources over the energy range 8 keV to 80 keV. A variable X-ray source [52] was used, in which an Am-241 source excites the characteristic X-rays from one of 6 different foil targets. The foils - Cu, Rb, Mo, Ag, Ba and Tb covered the 8 keV to 50 keV range, while the 60 keV and 80 keV lines from Am-241 and Ba-133 gamma sources, respectively, provided higher energy calibration points.

Figure 4.4 illustrates the good linearity observed over the whole energy range tested with the residuals, highlighting a significant deviation at higher energies. This is to be expected since the pre-amplifier settings are optimised over the 1 keV to 25 keV energy range. At energies below 8 keV complica-

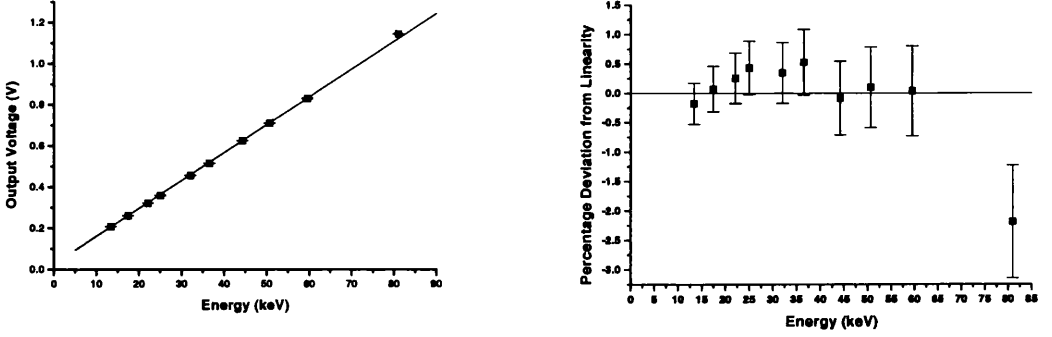


Figure 4.4: Linearity plots for ERD1 Detector

tions arise attributed to problems of charge injection from transistors in the PAC5 chip. This, as will be shown later in this chapter, has been corrected in the next generation of this detector module - the Dash-E.

4.3.2 Energy resolution

Since the ERD1 is a pixel detector it will have some imaging properties, though a pixel of $300\ \mu\text{m}$ side is too large for the majority of imaging purposes. Figure 4.5 shows the dual nature of the detector with an image of the silver source and the corresponding spectrum. The matrix illustrates the pixel to pixel variation across the detector, which is an offset variation in each pixel. Since it is an offset and not a gain variation it is relatively simple to correct for the pixel to pixel differences, as has been done in reference [50].

If a Gaussian pulse height distribution is assumed, then the observed FWHM W_T of a Si detector is given by the quadrature sum of a number of compo-

4.3 Detector Chacteristics

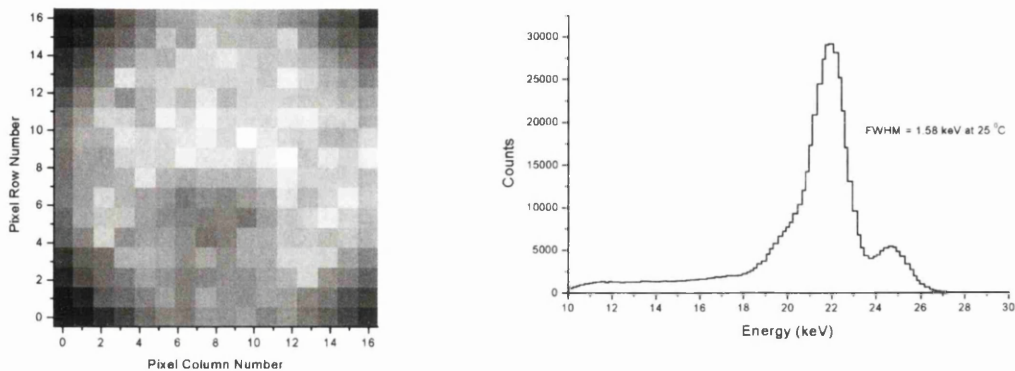


Figure 4.5: A spectrum from the ERD1 detector with the corresponding image

nents [22].

$$W_T^2 = W_E^2 + W_F^2 + W_X^2 \quad \text{where} \quad W_F^2 = 2.35^2 \epsilon F E \quad (4.1)$$

and

W_E is the FWHM due to the contribution from the electronics.

W_F is the FWHM attributed to the fact that the formation of each individual charge carrier is not independent and so is not described by Poisson statistics. F is the Fano factor, which corrects for this deviation, and is taken to be 0.12 here [19]. ϵ is the energy required on average to create an electron-hole pair in Si and E is the incident X-ray energy.

W_X is the FWHM characteristic of any leakage current or charge collection inefficiencies.

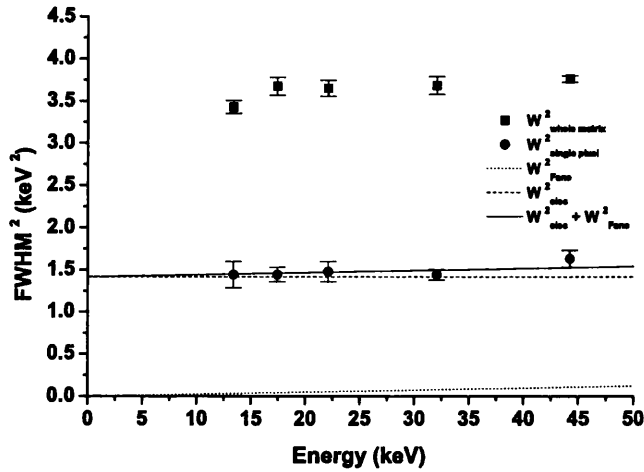


Figure 4.6: The variation of FWHM^2 with incident X-ray energy. The noise of the system is dominated by the electronic contribution.

The pulse height FWHM of this detector was expected to be dominated by the contribution from the Fano factor. However, due to the read-out problems, the electronic noise alone is of the order of 1.19 keV. This value was determined by lowering the threshold until the charge injected from the digital cross-talk was visible as a pulse height peak. The FWHM of this peak includes the contributions from the electronics and the leakage current and results from the combined effects of the W_E and W_X terms, from equation 4.1. The experimental variation of FWHM with energy is shown in figure 4.6. The plot includes both the single pixel response and the response from the whole matrix. The two sets of experimental points have the same gradient but are offset by a marked amount. This is due to the fact that the output of the detector array has yet to be corrected for pixel to pixel

4.4 The Dash-E detector

variations in gain. Also included in the plot is the observed contribution from the electronics and leakage current and the theoretical effect from the Fano factor. The combination of these terms, W_T , matches well the single pixel response, indicating that the electronic noise is the dominant term and that any other terms are negligible in comparison.

4.4 The Dash-E detector

This detector is the successor to the ERD1. The problems of high noise and charge injection, illustrated in the previous section, have been addressed with some additional features incorporated in the process. These alterations and improvements are three changes to the SHAMROC IC :

- an increased shaping time to 20 μ s
- a bipolar switch to allow electrons or holes to be collected at the readout electronics
- and a common mode which allows the whole detector to read out if one pixel records a hit.

The other main change comes on the PAC5 chip with the incorporation of an additional feedback capacitor in series allowing the capacitance of the front-end electronics to be switched to either 25 fF or 250 fF. This capability allows greater flexibility over the detector capacitance, which should be matched to the pre-amplifier capacitance for optimal noise performance.

4.4.1 Energy Resolution

The marked difference between the ERD1 and the Dash-E is the improvement in the energy resolution. Figure 4.7 illustrates the resolving power of the Dash-E detector. The pulse height spectra of fluorescent X-rays of Mn, Cu, Rb, Mo, Ag and Ba are shown on the same graph with the maximum count normalised to one. The K_α and K_β lines from each element are clearly visible, and for the case of the Ba lines the K_{β_1} and K_{β_2} lines are separated. This energy resolution is particularly impressive since all data were obtained with no on-chip cooling and at room temperature. It would appear that the detector noise is capacitance limited, since the resolution did not change as a function of temperature, from room temperature to $\sim 40^\circ\text{C}$.

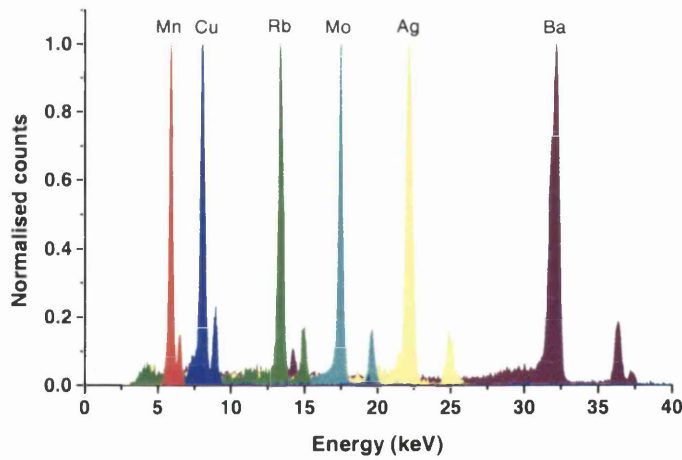


Figure 4.7: The Dash-E response to the characteristic X-rays of Mn-55, Cu, Rb, Mo, Ag and Ba.

4.4 The Dash-E detector

Noise

The energy resolution of the Dash-E detector is examined in this section. The noise of the system is sufficiently low that a determination of a value for the Fano factor is attempted. The Fano factor has not only a temperature dependence but also a dependence upon the energy of the interacting X-ray [51]. Due to the nature of this detector it is well placed to examine the Fano factor at room temperatures and over these hard X-rays. There exist very few reports of a value of the Fano factor measured at these energies and temperatures.

In order for the Fano factor to be determined the other components of the noise must be well characterised. The electronic noise of the system was tested by two methods to check for consistency. The first method required operation of the detector in “all” mode, where if a single pixel is hit all of the detection elements are read out. This means that the resultant spectrum contains not only the photopeaks of the incident spectrum but also a noise peak from the pixels that did not have an X-ray incident upon them. This Gaussian noise peak was examined for the case of Mo X-rays and a value of the FWHM at 230 ± 6.6 eV was obtained. The second method involved fitting the K_{α} peaks of the Mn, Cu, Rb, Mo, Ag and Ba spectra with Gaussian distributions. Their FWHM values squared are plotted against X-ray energy in figure 4.8. The extrapolation of this line back to zero energy should give the electronic noise of the detector, providing the preamplifiers are linear over this energy range. The FWHM of the noise peak is found to be 213 ± 63 eV using this method.

The linear extrapolation method gives a noise value which is consistent with

the fitting of the noise peak. Since fitting to the noise peak gives a lower error it is this value which is used, as the electronic noise, in the subsequent analysis. If this value of electronic noise is subtracted in quadrature from

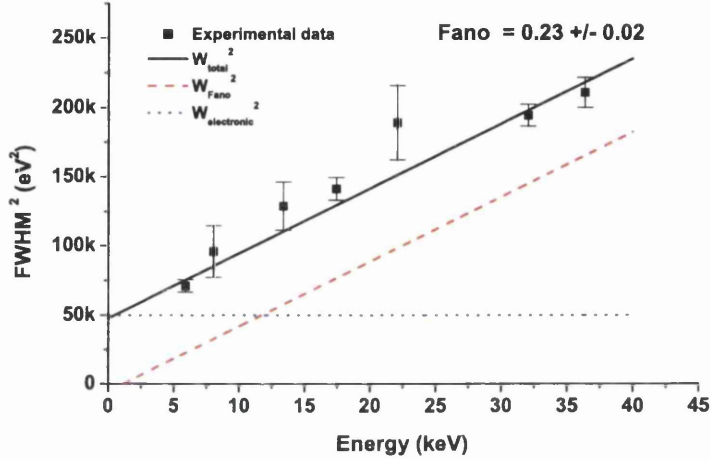


Figure 4.8: The variation of FWHM with incident X-ray energy. A Fano factor of 0.23 is required if no other effects contribute.

the total width, the residual contribution should be from the Fano factor - assuming full charge collection and no other noise effects. A linear fit was made to the data of figure 4.8 and the electronic noise contribution removed. The result gave a Fano factor of 0.23 ± 0.02 , which is substantially different from the commonly quoted value of 0.12 [19]. The various contributions can be seen in figure 4.8.

Conversely if a Fano factor value of 0.12 is assumed and the electronic noise is again taken to be 230 eV, then an additional term, W_X , is included in the analysis. How this term varies with incident X-ray energy can be seen

4.4 The Dash-E detector

in figure 4.9. This term is attributed to effects such as incomplete charge collection and contributions from the leakage current [22].

A marked difference between the observed Fano factor and the theoretical

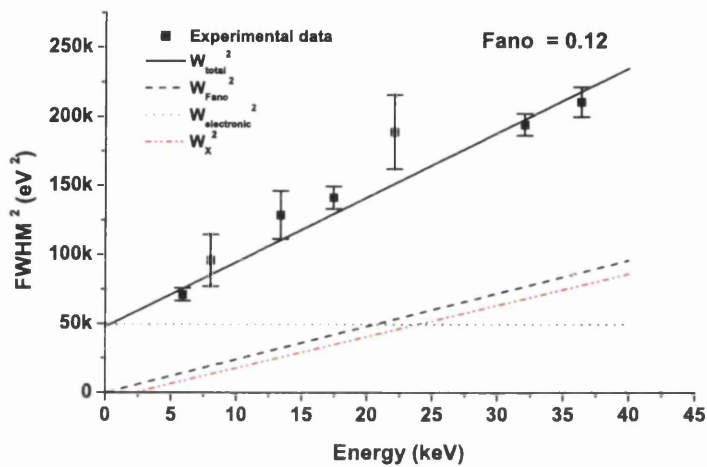


Figure 4.9: The variation of FWHM with incident X-ray energy. A Fano factor of 0.12 is assumed.

value is observed. Without further characterisation of the Dash-E detector it is difficult to say with confidence that the Fano factor shifts at these energies and temperatures to such a high value. However at the moment only one Dash-E detector has been built and further testing was not possible since it is located at the Rutherford Appleton Laboratories. The additional fact that the background continuum is much higher than expected (see over) also adds weight to the argument that an additional noise source is present within the detector system. However future experimental work with this detector could perhaps address these problems.

4.4.2 Background Continuum

The Dash-E system satisfies many of the requirements for high rate X-ray spectroscopy combined with low noise operation at room temperature. The noise of the detector is competitive with current spectrometers, and it would appear to be a viable detector for future X-ray detectors. However the large background extending from the photopeak downwards, evident in all of the spectra shown in figure 4.7, is a problem. Devices designed for applications such as this require a high peak to background ratio so that small amounts of trace elements can be detected in the presence of other X-rays. The peak to background ratio for the Dash-E detector is shown as a function of X-ray energy in figure 4.10. Only the four highest X-ray lines are considered since the threshold setting for the Mn and Cu lines was just below the photopeak and so no background was observed.

The peak to background was calculated by summing over the background from zero up to the start of the photopeak. The background was extrapolated to zero by taking the average of the background counts. It can be seen from figure 4.10 that the peak to background ratio degrades linearly with increasing energy. Possible explanations for this increase are charge sharing, where counts from the photopeak would be lost to the background if charge is shared between two pixels, or the increased effect of Compton interactions at higher energies. Absorption in the window side of the detector could also increase the likelihood of a high background and a lower than expected photopeak.

As will be shown later none of these effects can account fully for the poor

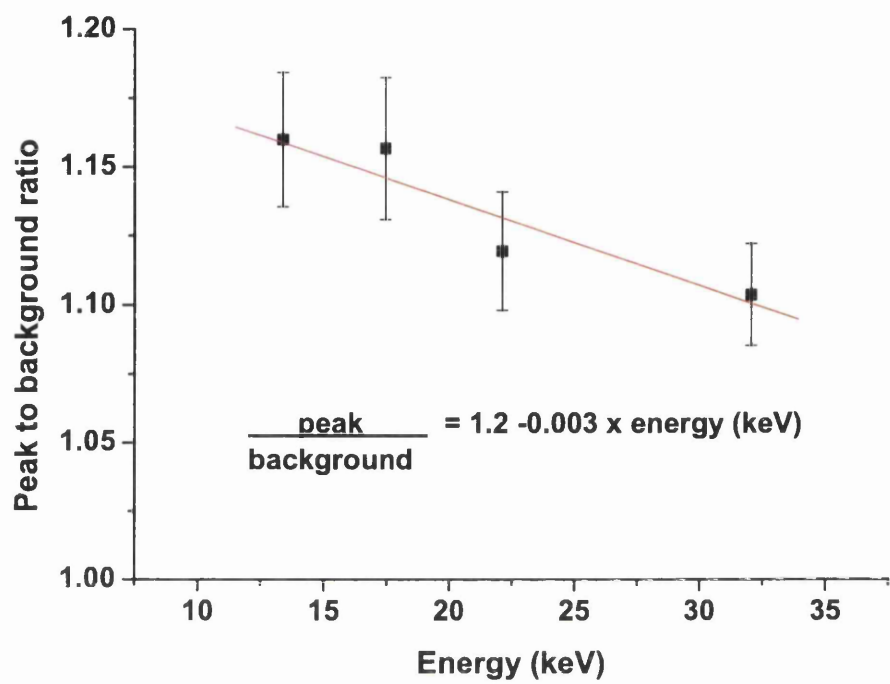


Figure 4.10: The peak to background ratio for the 4 highest energy sources Rb, Mo, Ag and Ba.

peak to background ratio, and perhaps the effect can be attributed to the read-out electronics. Further work is required to investigate this possibility in detail.

4.5 Discussion

Experimental evaluation of the ERD1 and Dash-E detector systems has been described with a view to building an understanding for later chapters, where the detectors will be used to comparisons will be made with the models

developed. Results from the ERD1 and the Dash-E detectors have been presented. The detectors exhibit good linearity over the energy range intended. Details of the noise performance of the systems has been highlighted, illustrating the impressive energy resolution of the Dash-E detector. Attention has been drawn to the lower than expected peak to background ratio, which is a potentially limiting factor.

Chapter 5

Comparison of experimental and simulated results

5.1 Introduction

In previous chapters theoretical models for the behaviour of pixellated devices have been proposed. However it is important to compare these simulations with experimental data in order to examine the accuracy of the models. In chapter 4 the Dash-E detector was introduced and it is this detector which has been used to obtain data with which the simulations will be compared. The Dash-E is a silicon detector and the models proposed up to now deal with other solid state materials, namely CdZnTe and GaAs. However verification of the Monte-Carlo code MCNP and the finite element package MEDICI, through the modelling of a silicon detector will add weight to the arguments proposed for these materials.

5.2 Comparison of MCNP and experiment

A detailed 3-D model of the Dash-E detector was created within the modelling package MCNP. It included the silicon detection element, the silicon readout electronics and the bump bond complete with the metallisation layers. This pixel was arrayed in a 16 by 16 matrix to form a complete model of the detector. MCNP requires the atomic number and the ratios of the constituent elements in addition to the geometry and source definitions. Figure 5.1 shows a 2-D cross-section of the pixel element which has been arrayed in a 16×16 matrix. A close-up of the central region is highlighted since artifacts of these materials will be discussed later. Table 5.1 shows the source information contained within an MCNP model.

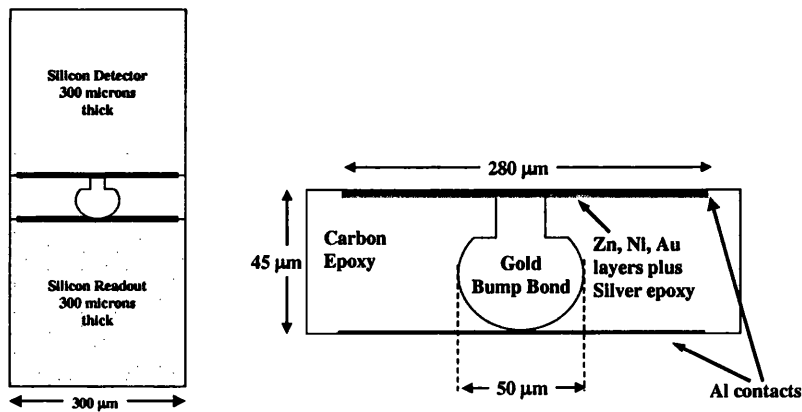


Figure 5.1: MCNP geometry of the Dash-E detector.

The geometry of the source-detector set-up is a point source emitting photons directed down a line through the centre of one of the pixels. The whole detection volume (a cube with $300 \mu\text{m}$ sides) is then 'tallied'. This

5.2 Comparison of MCNP and experiment

Table 5.1: Source definition data for barium

Decay line	Energy (keV)	Intensity (per 100)
K_{α_1}	32.194	46.7
K_{α_2}	31.817	25.6
K_{α_3}	31.452	0.00334
K_{β_1}	36.378	8.63
K_{β_2}	37.255	2.73
K_{β_3}	36.304	4.47
K_{β_4}	37.349	0.023
K_{β_5}	36.652	0.1
$O_{12,3}$	37.425	0.4

detector-source geometry emphasises the fluorescence contribution from the gold bump bond. The ideal situation would be to flood the whole pixel array with photons, but an unreasonable amount of computation time has to be used to obtain good statistics. To investigate whether this generalisation compromised the validity of the model, a point source was stepped across the pixel in 10 nm steps. The result showed no effect on any part of the spectrum except for the introduction of the gold series of K-shell fluorescent lines. These were evident over a small portion of the detector immediately above the bump-bond, and their contribution to a uniformly illuminated pixel was considered negligible. Other contributions, such as that from the contact layers, as we shall see, cannot be discounted since they cover the majority of the detector - unlike the bump-bond. When the likely applications of these devices are considered, the detection of trace elements, the effects of these

spectral contaminants can be important.

Figure 5.2 shows the comparison of a barium spectrum taken with the Dash-E detector and the output from the MCNP model. A feature of MCNP is the incorporation of a Gaussian energy broadening term which accounts for spectral broadening due to the noise of the system. Figure 4.9 in chapter 4 showed how the noise of the Dash-E varied with incident X-ray energy. It is a fit to these data points which act as an input to the model. The two most prominent differences between the model and experiment are the differences in the photopeak height and the background counts. The model and experiment have had the height of the K_{β_2} peaks fixed to equal values. This peak was chosen since the effect of the background on this peak will be small in comparison to the K_{α} peaks. The expected K_{α} photopeak has 13 % more counts than the experimental equivalent. Part of this discrepancy will be due to charge sharing between pixel elements, since the model (at this stage) does not take into account this phenomenon - later it will be shown that this alone cannot account for the loss of counts in the photopeak. There is also a lower energy tail just below the photopeak which is sometimes attributed to a slight charge collection inefficiency, perhaps through absorption in the entrance window (in this case the n+ layer). If part of the charge cloud is generated in the n+ layer it will recombine and be lost whilst the remaining charge carriers (generated outside the n+ layer) will be collected. This will result in a charge loss, however this should be small in this case since the dead area corresponds to only 1 or 2 μm .

An interesting point is the presence of the silver fluorescence peaks, the K_{α}

5.3 Comparison of MEDICI models

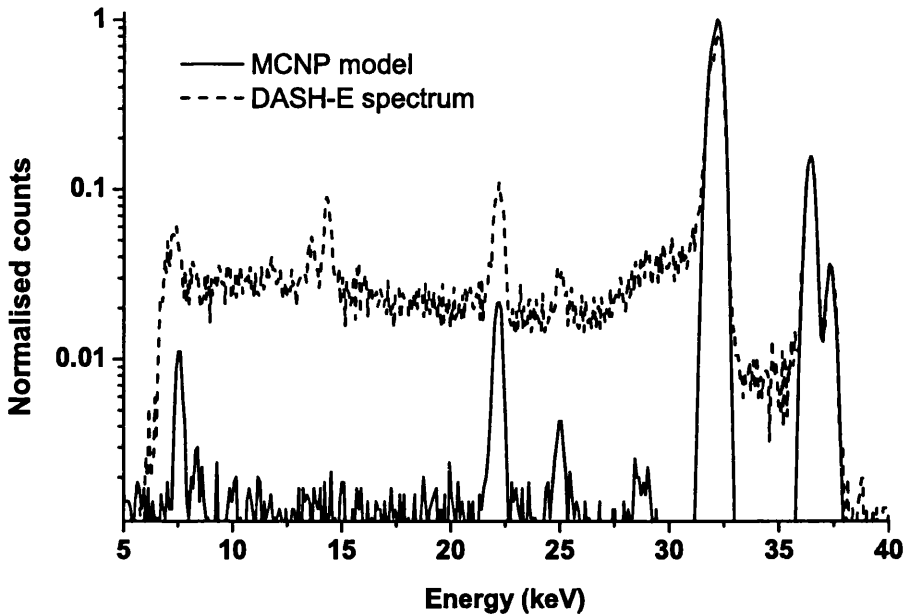


Figure 5.2: A comparison of a Barium spectrum from a modelled Dash-E detector and the experimental output.

and K_{β} lines being visible in both the modelled spectrum and the experimental data. This is due to the silver epoxy layer which is part of the detector - readout coupling process.

5.3 Comparison of MEDICI models

In this section the effects of charge sharing in the Dash-E detector are analysed and compared with modelled predictions using a combination of MCNP and MEDICI.

As has been discussed previously the sharing of charge between adjacent pixel

elements could lead to limitations for pixellated detectors. Here a value is placed on the amount of charge shared for the 300 μm square pixels of the Dash-E. This is then compared with the simulations which are then used to extrapolate to other pixel dimensions.

5.3.1 Experimental work

One of the additional features that the Dash-E has is the ability to read out all of the channels if one records a hit. This means that if a pixel is hit, the neighbouring pixels can also be examined.

Data of this format were taken for the the X-ray lines of Mn, Cu, Rb, Mo, Ag and Ba. The steps that follow are the analysis that each data set undergoes.

- The data set is read into a C-program where all of the pixel offsets are subtracted by the use of a calibrate file¹.
- The maximum value of each readout cycle is selected as the hit pixel.
- The 8 surrounding pixels and the hit pixel are then selected from each readout cycle.
- An upper energy threshold value is then set to a value of 1 keV above the K_β peak of the chosen spectrum. All hits above this value are discarded since here we only want to consider hits from the chosen spectrum. Hits which will be discarded will arise from the 60 keV Am-241 γ -rays.
- The charge shared from the surrounding pixels is expressed as a percentage of the total charge.

¹Calibrate file courtesy of Steven Passmore

5.3 Comparison of MEDICI models

- A threshold is set at low energy since every pixel will have an associated noise.
- The data are output to file for a scan of this lower threshold - from zero to the photopeak. The format of the data is the fraction of charge shared events as a function of threshold.

As a check to ensure that charge shared events are being considered and not spurious or coincident hits, the information selected from the Mo dataset is shown in figure 5.3. This shows the events that have been selected by the C-program alongside the resultant spectrum, where the signal from the neighbouring pixel with which charge is shared is added to that from the hit pixel. Here the spectrum is effectively being corrected for charge sharing. This illustrates firstly that charge sharing takes place and that it results in a reduction of the photopeak intensity and an increase in the background level. It can also be seen in the selected data that some counts have escaped the cuts since a K_{α} peak is visible in the data, this accounts for 10 % of the total counts.

Figure 5.4 shows the output of the data analysis - the percentage of charge shared as a function of threshold energy. As expected the charge shared goes to zero at half the energy of the principle photopeak, since a 50 % split is the maximum amount of charge that can be shared. At a threshold below 2 keV the noise from the system begins to enter into the charge shared events, so the graph below this point holds no real information. It can be seen that the amount of charge shared increases with energy over the range tested. For example if we consider an energy threshold of 4 keV we have 2.0 % charge

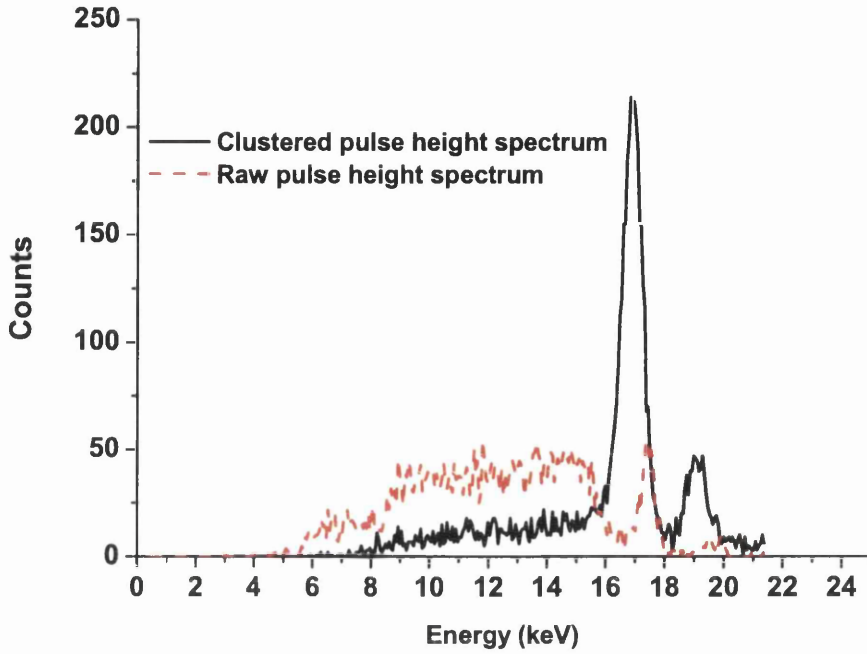


Figure 5.3: The charge shared data from the Mo dataset, showing the raw data and the spectrum adjusted for charge sharing (clustered). The raw data corresponds to data in which a charge shared event has occurred but no correction has been performed. The clustered data is the same data but this time the charge sharing correction has been included.

loss for Rb, rising to 3.4 % at Mo, 4.0 % for Ag and 4.5 % at Ba. This increase is to be expected, since the energy of the photoelectron increases with incident X-ray energy.

5.3 Comparison of MEDICI models

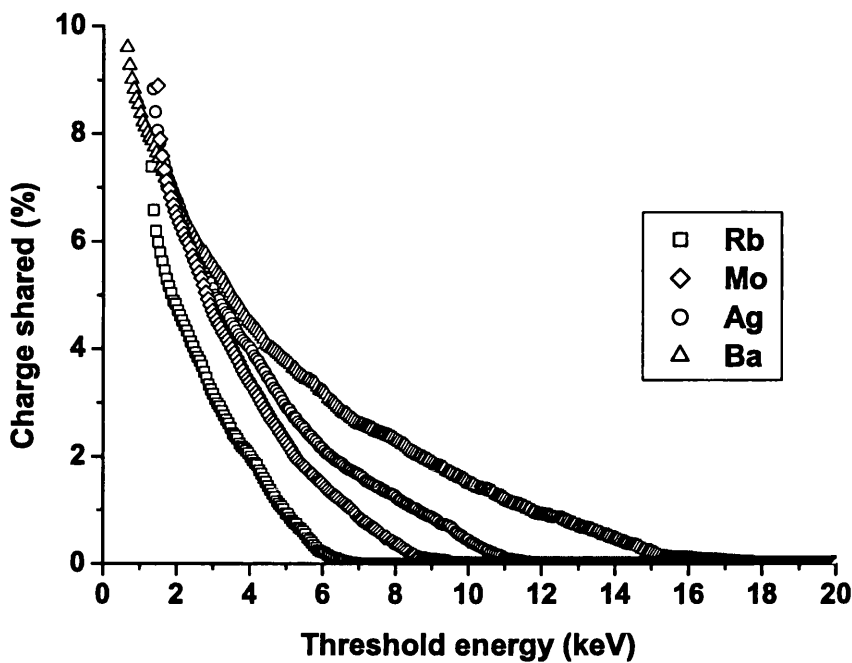


Figure 5.4: Charge shared as a function of threshold energy for the Dash-E detector

5.3.2 Modelling charge sharing with MEDICI

The method outlined in chapter 7, where the effects of charge sharing on the performance of a CdZnTe pixel detector are examined, is adapted here for the modelling of the Dash-E detector. The MCNP model is the detailed geometry described previously in this chapter and shown in figure 5.1. The interactions considered contain all of the spectral lines for the sources Rb, Mo, Ag and Ba (see appendix C) as part of the MCNP input. The output - needed as the input to MEDICI - is the energy deposition distribution in the detector material. These data describe the energy deposition for an av-

erage of many photons emitted from a point source, so their incorporation in to MEDICI means that the particles will be drifted through the detection medium all at once. For this to be valid the charge density of the carriers must be below that where carrier-carrier interactions become important. Experimentally this density has been observed to be far above that of the charge carrier density here [80]. Since MCNP is a 3-dimensional code and MEDICI is 2-dimensional, some manipulation of the data is required. As has been described previously the energy deposition from MCNP is extracted in a $1\text{ }\mu\text{m}$ slice through the detection material. This gives the energy density distribution in 2 dimensions. This profile is then created in MEDICI where the model has the same doping densities, implants and operating voltages as the experimental case (the Dash-E detector operating at 80 V reverse bias). Figure 5.5 shows a schematic of the $300\text{ }\mu\text{m}$ thick silicon detector, with the important input parameters of the model. A key aspect of the charge transport is ensuring that the width of the modelled semiconductor is such that no charge is reflected at the Neumann boundaries (where the E-field perpendicular to the surface goes to zero). This is the unalterable default setting for all surfaces not in contact with an electrode in MEDICI, and will change the charge distribution at the contact if not accounted for.

The charge distribution that is the result of the MEDICI simulation takes into account the following effects :

- The source characteristics - spectral lines and relative intensities
- The multiple scattering of the photoelectron and fluorescent contributions in $300\text{ }\mu\text{m}$ silicon (MCNP data).

5.3 Comparison of MEDICI models

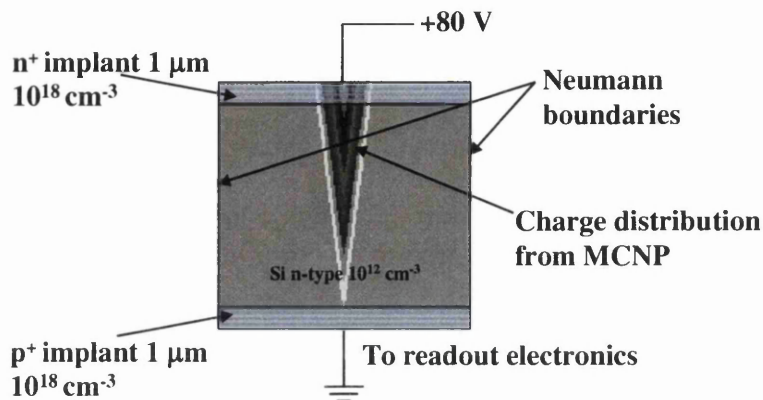


Figure 5.5: The modelled detector - the charge density should be below that where plasma effects are evident. The modelled width should be sufficiently wide so that no charge is reflected at the Neumann boundaries.

- The drift and diffusion of the carriers in the detector geometry (using Poisson’s equation - MEDICI data).
- The operating conditions of the Dash-E detector (80 V reverse bias at room temperature).

The profiles for the 4 sources tested is shown in figure 5.6 where the maximum of each curve is normalised to unity for comparison. It can be seen that the width of the charge profile, seen at the collecting electrode, increases with increasing photon energy as expected. The fit to the data in each case is a double Gaussian. The increase in FWHM is 3 μm - from 16.5 μm for Rb to 19.5 μm for Ba. The full width of the distributions at the 20 % level is more pronounced - 36.5 μm at Rb to 45.6 μm at Ba.

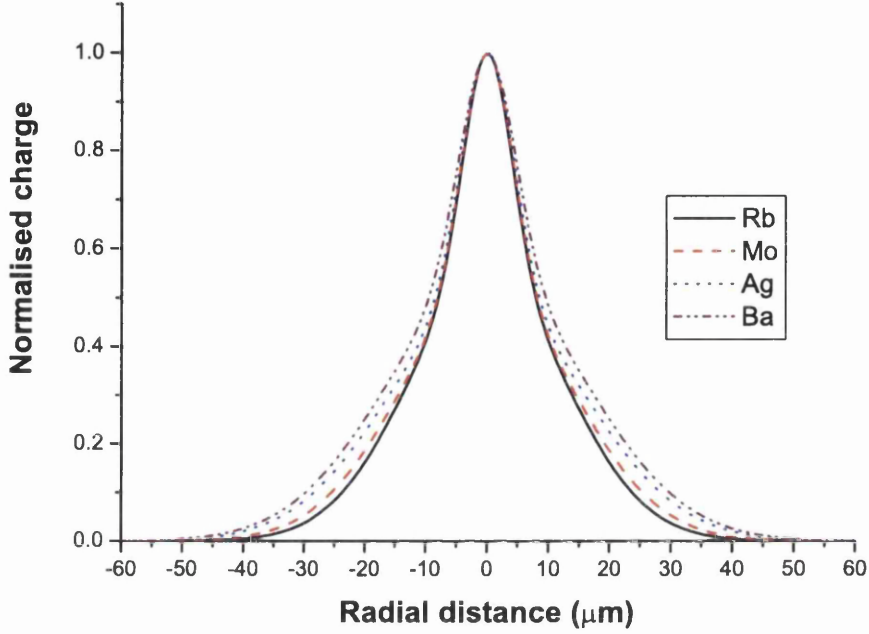


Figure 5.6: The normalised charge distributions for each source after transport through modelled Dash-E detector.

When these profiles are integrated over the $300\text{ }\mu\text{m}$ square pixel dimensions, whatever percentage of the total charge lies outside the pixel dimensions, is the maximum charge lost to the neighbouring pixel (an illustration of these distributions is shown in chapter 7 figure 7.12).

5.3.3 Comparing experiment with simulation

A comparison of the model with the experimental data presented above, will enable the validity of the models to be confirmed. If there is agreement then the simulations and analysis techniques can, justifiably, be used in a predic-

5.3 Comparison of MEDICI models

tive context.

Figure 5.4 shows experimentally how the amount of charge shared varies with the position of the minimum energy threshold. The amount of charge shared that is calculated by the modelling analysis just described gives one value for charge shared corresponding to a threshold of zero. In order to find how the modelled charge lost depends upon the threshold, the following method was used.

Figure 5.7 shows the method used. This is a 2-D cut through the charge distribution under a pixel with the y-axis corresponding to the amount of charge generated normalised to unity. For a uniform illumination the maximum amount of charge (Q_{max}) that can be collected below that pixel is the volume of the cuboid (height equal to unity, other sides equal to pixel pitch). The volume of the charge outside the pixel boundaries is the amount of charge lost (Q_{lost}) - this profile is obtained from integrating the curve of figure 5.6. The percentage of charge sharing is then the ratio $\frac{Q_{lost}}{Q_{max}} \times 100$, for a threshold of zero. However to compare with figure 5.4 a threshold dependence must be introduced. This can be accomplished by remembering that only a maximum of 50 % of the charge deposited by an interacting particle can be shared. The integration over the lost charge from this point corresponds to the zero threshold level and a fractional threshold value of 0.5. If the integration starts at a further out point along the curve of lost charge, the corresponding fractional threshold, denoted f , is linked to the threshold energy, $E_{threshold}$, by the equation $E_{threshold} = (\frac{1}{2} - f) \times E_{photon}$. When the fractional threshold reaches zero the threshold energy is equal to half the incident photon energy, since the maximum charge shared corresponds to a

50-50 split. The result are the lines shown in figure 5.8 where they are compared with the experimental data from the Dash-E detector.

As can be seen the simulations and the experimental data agree reason-

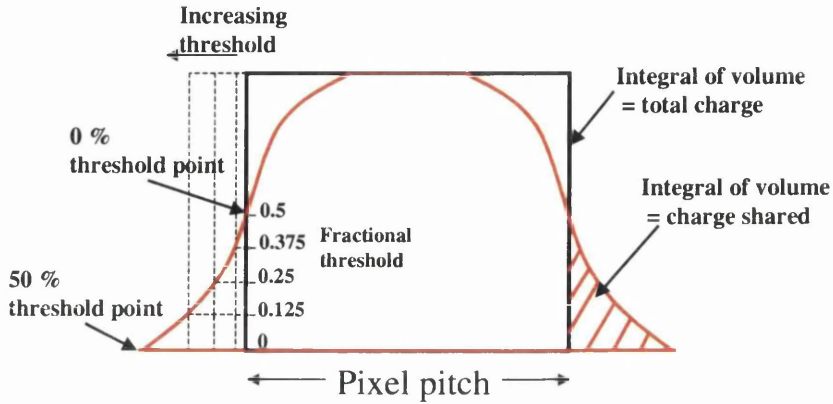


Figure 5.7: Illustration of method for the calculation of charge sharing

ably. Barium is the only set of X-ray lines which show a slight disagreement over the mid range of threshold values. The deviation at low threshold values in all of the X-rays examined is due to the noise of the Dash-E system. This leads to spurious charge shared events when the threshold is too low (observed here to be below 2 keV).

5.3.4 Predictions

Now that the models have been tested against experiment and observed to be in close agreement, they can be used to predict the behaviour of other pixellated detectors.

Firstly we can break down the charge sharing effects to analyse which of

5.3 Comparison of MEDICI models

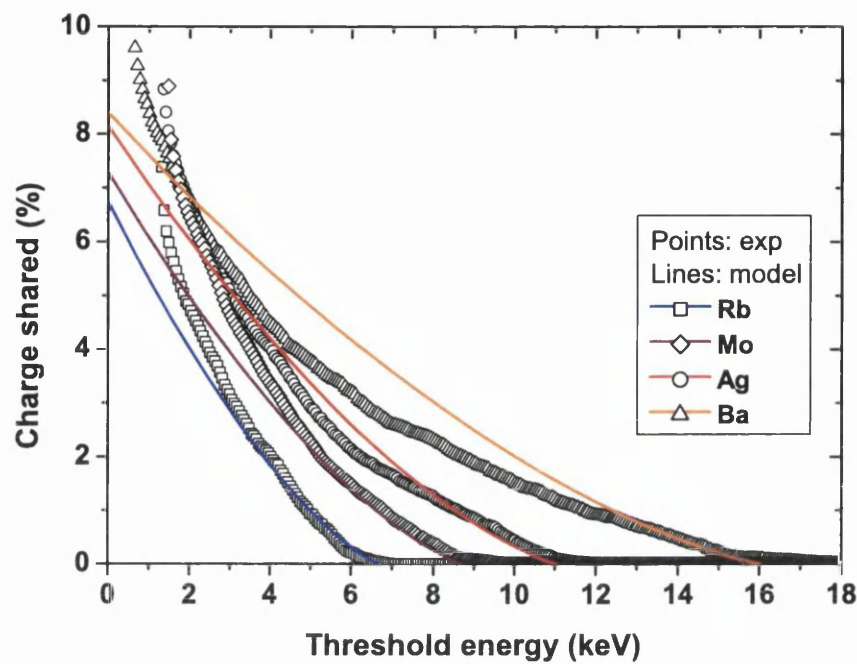


Figure 5.8: Comparison of simulated and experimental results of charge sharing, as a function of energy threshold, for the Dash-E detector.

the physical processes has the greatest effect - the particle interactions and subsequent generation of particles (photoelectron and fluorescent photons) or the electrical transport in the semiconductor (diffusion). To do this the procedure outlined above was repeated for the charge distribution profile before it went through the diffusion process (i.e. the MCNP output). This allows the analysis of charge sharing for the case of no diffusion and so we can attribute the amount of charge shared to each of the physical processes. Figure 5.9 shows how the charge shared for the Dash-E detector would vary

with threshold energy if there was no diffusion in the detector. This shows

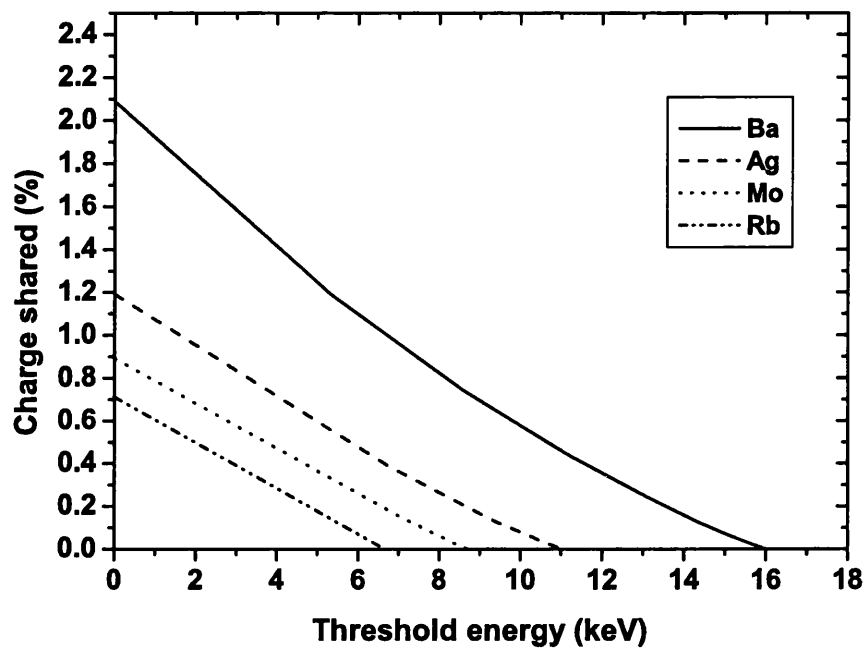


Figure 5.9: The amount of charge shared in a 300 μm thick Si detector, 80 V reverse bias, with 300 μm square pixels, neglecting the diffusion process.

that the multiple scattering of the photoelectron in the silicon, leads to an increase in the charge shared, as expected. It also enables the association of a certain percentage of charge shared events with this effect. With no threshold applied the amount of charge shared for no diffusion, diffusion and the difference is shown in table 5.2.

This table shows that over the energy range considered, the dominant effect

5.3 Comparison of MEDICI models

Table 5.2: A breakdown of charge sharing effects for the Dash-E detector for the case of no threshold.

Energy of K_{α} (keV)	No diffusion (%)	Diffusion included (%)	Difference (%)
13.34	0.72	6.7	5.98
17.44	0.9	7.3	6.35
22.1	1.2	8.1	6.9
32.06	2.1	8.4	6.3

in charge sharing is due to the diffusion process - approximately constant at $\sim 6\%$. It also shows that the difference in charge sharing over the X-ray energy range considered is due to the interaction process and not due to the diffusion process. This is significant since the higher the energy of the X-ray the higher the probability of the X-ray interacting at a deeper point in the semiconductor. The resultant charge cloud will therefore have more time to diffuse and lead to a wider profile and so more charge shared. However, for the data presented above, this effect is not significant. This is because all of the four X-ray energies considered have quite a low absorption efficiency in silicon. Thus all four will create some charge at the various depths throughout the material.

The models can also be extended to examine other detectors and used as a design tool to predict charge sharing effects in detectors not yet built. For example new highly pixellated silicon detectors are under design with a pixel pitch of $55\text{ }\mu\text{m}$ [34]. This detector will be a photon counting detector intended for imaging. When the models are applied to a detector of this type then a

substantial amount of charge sharing is predicted, see figure 5.10. If these detectors are looking at monoenergetic X-rays then a threshold could be placed at 50 % of the X-ray energy, and no charge shared events would be observed. The number of hits recorded would not be affected and there would be no blurring of the image. Unfortunately detectors such as these have potential medical imaging applications where commonly a bremsstrahlung continuum is used as the source. This means that the higher energy X-rays will be present and placing a threshold value will not eliminate the charge shared events from the high energy part of the bremsstrahlung spectrum.

If the limits of integration of the charge profile are changed then the dependence of charge sharing on pixel size can be investigated - as was done previously in chapter 7. This result is shown in figure 5.11.

5.4 Discussion

The chapter started with a comparison of a barium spectrum from the Dash-E detector with the output of an MCNP simulation. The agreement is close with the only disagreements being in a higher than expected experimental background and a lower than expected photopeak. The effect of the silver epoxy is predicted by the model and observed in the experimental data. This shows that the model can be used as a design tool for new detectors and effects such as the silver peaks can be analysed, and if necessary, steps can be taken to minimise their effects.

The effect of charge sharing was investigated experimentally using the Dash-E detector. The charge shared as a function of threshold energy was examined

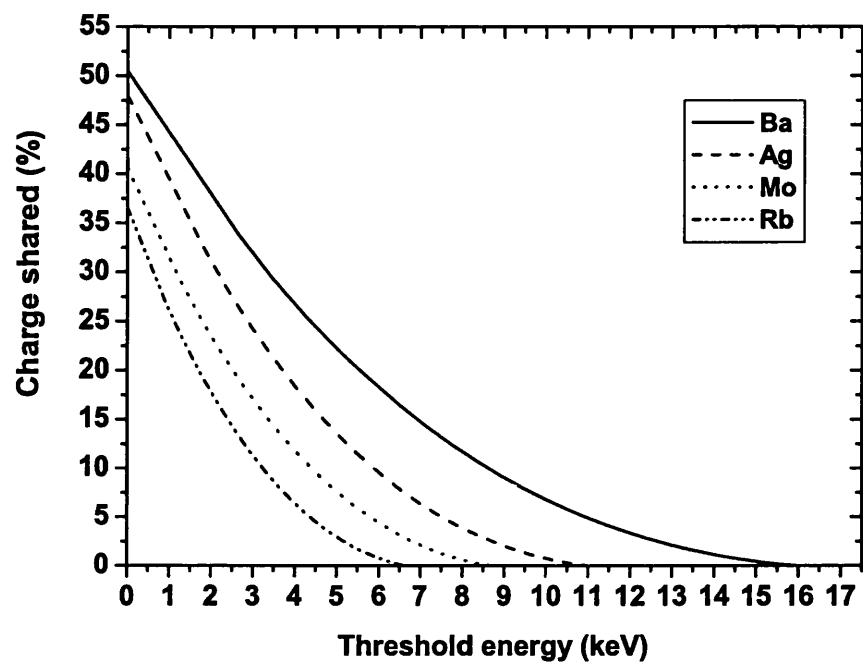


Figure 5.10: New imaging detectors plan to use 55 μm square pixels on 300 μm thick silicon. The models indicate a substantial amount of charge will be shared with neighbouring pixels.

and observed to vary from 2 % to 4.5 % over the energy range tested, at a threshold of 4 keV.

A combination of MCNP and MEDICI allowed a model, which contains all of the physical effects, to be developed. The model compares well with the experimental data especially in the lower energy X-ray regime (13 keV to 22 keV). There is an increased difference between the models prediction and experimental data for barium, though only at the 0.5 % level.

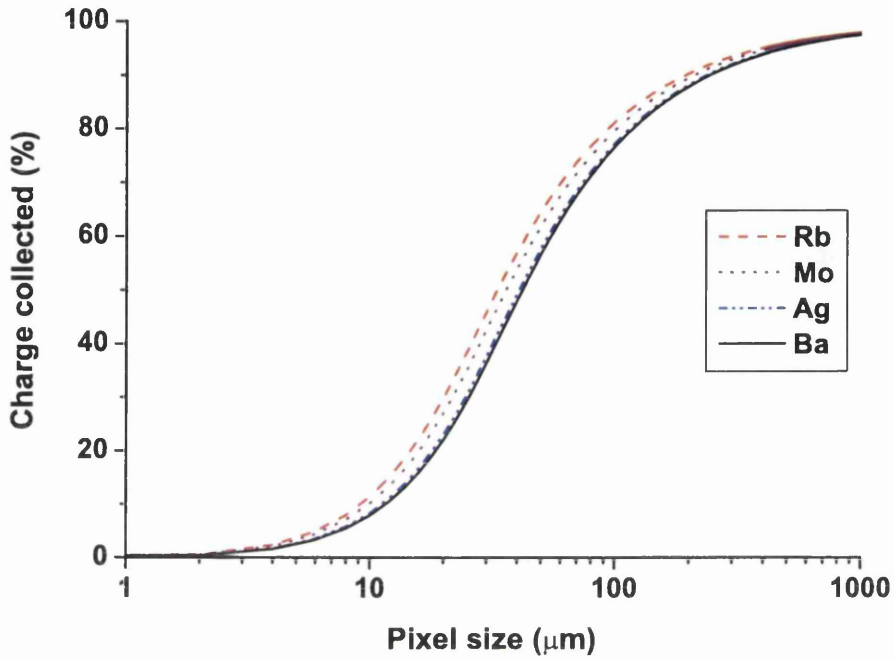


Figure 5.11: The dependence of charge sharing on pixel size for a 300 μm thick silicon detector operated at 80 V.

The two principal effects in charge sharing, the particle interactions and the subsequent charge transport, have been separately analysed. It is observed that the diffusion is constant over the energy range considered and that the variation in charge sharing with X-ray energy is attributable to the initial particle interactions and primarily the energy given to the photoelectron.

Chapter 6

3-D detector simulations

6.1 Introduction

In this chapter the performance of a novel architecture for pixel detectors is discussed. The 3-D structure has electrodes that penetrate the bulk of the detector medium allowing low-bias, high-speed operation along with improved charge collection efficiency. The modelling package MEDICI was used to simulate epitaxial gallium arsenide 3-D detectors. This included an analysis of charge transport and signal formation, with details of the expected charge collection efficiencies. The matrix of small diameter holes through the semiconductor required for these detectors may be fabricated by a number of means including dry etching. The effects of dry etch damage on detector performance is also modelled as this is potentially an important factor.

The Monte Carlo code MCNP has also been used to investigate what influence the metal electrodes, which fill the holes, have on the structure's performance as a radiation detector.

6.2 Motivation

Conventional planar technologies for semiconductor detectors are already established as the benchmark for pixellated devices. The most technologically advanced detection material is silicon, due mainly to its development in the electronics industry. However, the low absorption efficiency of silicon at photon energies above 10 keV limits its applicability to higher energy X-ray detection. Materials with greater absorption coefficients, such as GaAs, have been investigated [31] as alternatives. These detectors, however, suffer from incomplete charge collection resulting from imperfections in the crystal structure. This reduces the mean free drift lengths of the charge carriers in these materials and limits the thickness of the sensitive region. Additionally, problems with the growth of GaAs have led to a higher than desired effective carrier concentration and so increased operating voltages. This implies thin detection layers and, in some cases, the presence of an undepleted layer.

Recently, a novel design has been proposed in which the electrodes penetrate through the detection medium [35] (see figure 6.1). This structure has the potential to solve some of the current limitations of semiconductor detectors. The reduced collection distances mean that short drift lengths are no longer a limitation and low operating voltages can achieve full depletion. These properties make the detector structure attractive for many applications, not least as a radiation hard alternative to current high energy physics detectors. The suitability of this detector design as a high energy particle detector is investigated in references [35] and [55]. In addition to the previously mentioned advantages, this structure has further properties which are beneficial to high energy particle experiments, namely :

6.2 Motivation

- Future colliders will have beam crossings at intervals that are shorter than the collection times of the generated charge in planar detectors.
- Thin detectors are required to minimise absorption and scattering in the semiconductor tracker. However as planar detectors become thinner their capacitive noise increases and generated charge is reduced (signal to noise ratio reduced). Capacitance is reduced as detector thickness decreases in 3-D detectors.

One of the major disadvantages of this type of detector is the complexity of the fabrication steps needed to realise the device. In order to keep the dead area to a minimum, holes with a small radius must be formed. The holes should penetrate with a constant diameter right through the detector layer. Working detectors have been formed in silicon, by reactive ion etching of the holes [55], and in GaAs [56] by laser ablation. Electrochemical etching of silicon has also been suggested as an excellent aspect ratio - 200 μm deep holes with 1 μm radius - has been achieved in silicon [57]. However it has not yet been shown if this method can be used to fabricate the co-axial structure in GaAs. The laser drilling technique requires a femtosecond laser, and at present is a time consuming method of fabrication. The surface damage and low aspect ratio also cause limitations.

An alternative is to use ion bombardment via a dry-etch to create the desired structure. This technique is used routinely in the fabrication of small scale electronic devices, such as field effect transistors. Though it is anticipated that this technique will be able to create holes with the required dimensions, these etches are known to cause sidewall damage [58] under certain etch conditions. How these defects, so close to the collection electrodes, will affect

the charge collection efficiencies of the detectors is still uncertain and is investigated here via the device modelling package MEDICI.

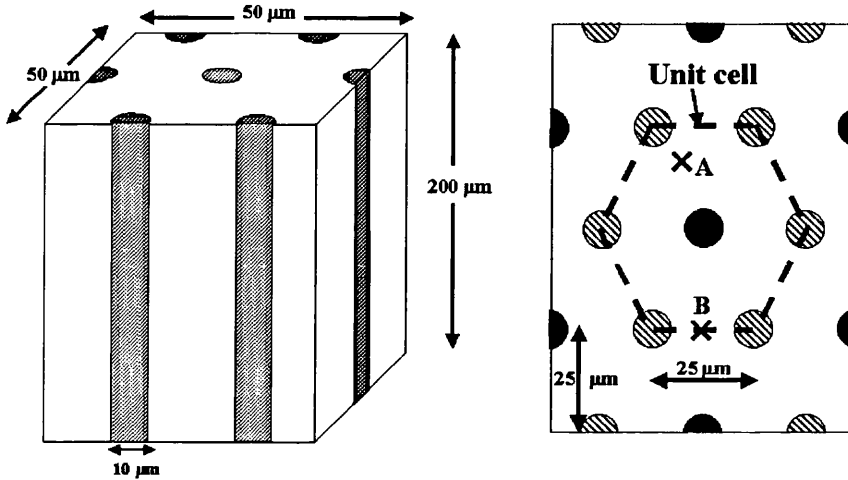


Figure 6.1: Pixel detectors with co-axial electrode structure. Left the unit cell and right the simulated cross section from MEDICI. The heavily shaded circular electrodes are held at a different potential than the lightly shaded electrodes. Points A and B are charge generation points discussed later in the text.

6.3 Detector Characteristics

As has been mentioned previously, it is anticipated that these detectors will find applications in the imaging, spectroscopic and particle detection fields.

6.3 Detector Characteristics

Silicon detectors of this type have already been fabricated [55] with impressive spectroscopic resolution observed at room temperature. In the silicon detectors it is anticipated that the electrodes will be filled by radially doped polysilicon. This will generate an electric field which, although low, is enough to sweep out any charge generated in the electrodes, so in this case it has been proposed that the detector has no dead area and that its imaging properties will not be substantially affected. It is proposed that for the GaAs detector structure, typical Ti:Pd:Au Schottky contacts would be fabricated as a first case. How these, predominantly gold filled, electrodes affect the spectroscopic and imaging properties has been investigated, as described below, by the Monte Carlo code MCNP [16].

6.3.1 Monte Carlo simulation

To examine whether the electrodes are in reality to be considered a dead volume, several MCNP simulations were run. In each simulation a point source of 60 keV photons illuminated a region of the detector, and the amount of energy deposited in the GaAs detection medium was calculated. Here the energy deposited inside the electrode region is considered to be lost. Since a constant potential exists in the electrodes there is no electric field and so no movement of charge. Therefore any energy lost in the electrodes will not contribute to the current signal on the contact and so the area is not sensitive to the interacting X-rays. The point source was stepped across the inter-electrode region, from the centre of one electrode to the centre of the adjacent electrode. The results can be seen in figure 6.2, where the point source is moved in 1 μm steps. The data have been normalised to the energy

deposited on average for 10^6 photons of energy 60 keV in 200 μm GaAs. The peaks at a point just inside the electrode correspond to the fact that all of the 60 keV is deposited in this area and a significant fraction escapes into the detection region in the form of lower energy fluorescence photons and photoelectrons. These, being of lower energy, are completely absorbed whereas the 60 keV photons incident on the middle of the detection region are not completely absorbed. The absorption efficiency of 200 μm thick GaAs is around 20% at this energy (see figure 3.9).

6.4 Electrical Simulation

The commercial modelling package MEDICI has been used to simulate a cross section of the 3-D detector structure (see figure 6.1). The material parameters used for this modelling complete with their values are shown in table 6.1. For the remainder of the variables the MEDICI manual [15] has a complete listing with references. The models included in the simulations are impact ionisation, the incomplete ionisation of donors and acceptors, Shockley Read Hall statistics and Auger recombination. A deep donor positioned 0.75 eV below the conduction band (corresponding to the EL2 trapping centre discussed in subsection 3.3.6) has been included in all of the subsequent simulations at a concentration of 10^{14} cm^{-3} [27].

These detectors deplete in the lateral direction, instead of the vertical direction of typical pixel detectors, leading to charge movement in this plane. The depletion regions for the simulated cross section are illustrated in figure 6.3. They are shown in 10 V steps from 0 to 40 V, after which the detector becomes fully depleted. This plot indicates that such a detector could be

6.4 Electrical Simulation

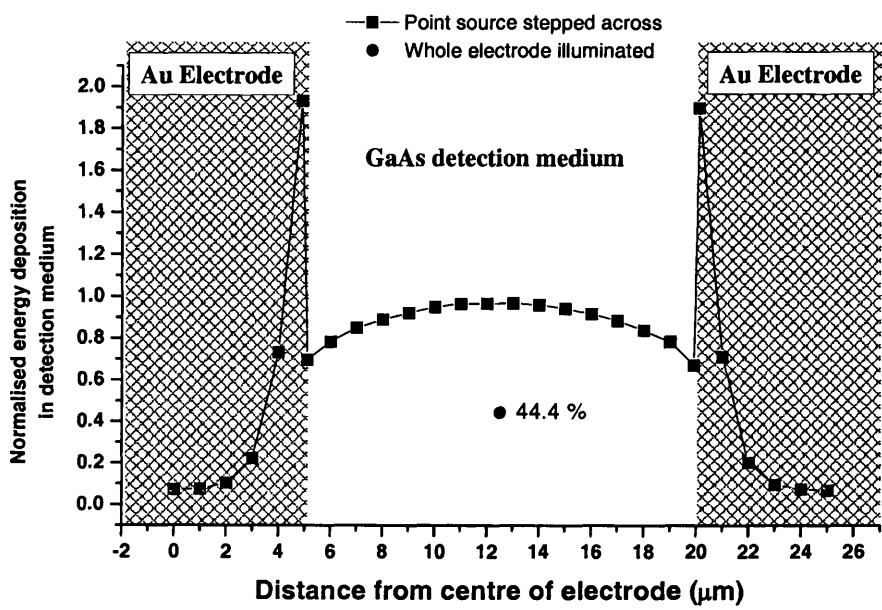


Figure 6.2: Point source of 60 keV photons scanned from electrode to electrode in 1 μm steps. The circular point is the energy deposited in the detection medium when a $5\mu\text{m}$ radius electrode is uniformly illuminated. All data are normalised to the average energy deposited in 200 μm GaAs for 60 keV photons.

operated at 50V, in comparison with the 300 V that a typical 200 μm thick GaAs pixel detector would require [26].

The potential profile for this operating voltage is shown in figure 6.4 alongside the case of 75 V bias. The 50 V case, although fully depleted, exhibits a low field region in the inter-electrode region highlighted in the plot. This will adversely affect the charge transport in the device, as will be shown in the

Parameter	Value	Reference
Density (g/cm ³)	5.317	[59]
Bandgap E_g (eV) at 300 K	1.424	[59]
Electron lifetime τ_n (s)	10^{-9}	[60]
Hole lifetime τ_p (s)	10^{-7}	[60]
Permittivity	13.1	[59]
Schottky contact workfunction (V)	4.79	[36]
Affinity (V)	4.07	[59]
Electron effective mass (m_o)	0.067	[59]
Hole effective mass (m_o)	0.5	[59]
Electron mobility (cm ² /Vs)	8500	[59]
Hole mobility (cm ² /Vs)	400	[59]
n-type doping conc. (cm ⁻³)	10^{14}	[63]

Table 6.1: The material parameters, with references, used in the simulation packages MEDICI and MCNP to model GaAs.

next section. For 75 V bias the potential gradient, and so E-field, is greater in this area and so less of an effect on the charge transport is observed.

The current-voltage characteristics are also of importance when considering the optimum operating voltage. Figure 6.5 shows the modelled I-V characteristics of such a device. The left ordinate axis shows the leakage current for a 200 μm thick detector with the right hand y-axis showing the leakage current density. For an operating voltage of 50 V a 200 μm thick detector would have a leakage current of 400 pA per pixel (pixel pitch of 50 μm). This

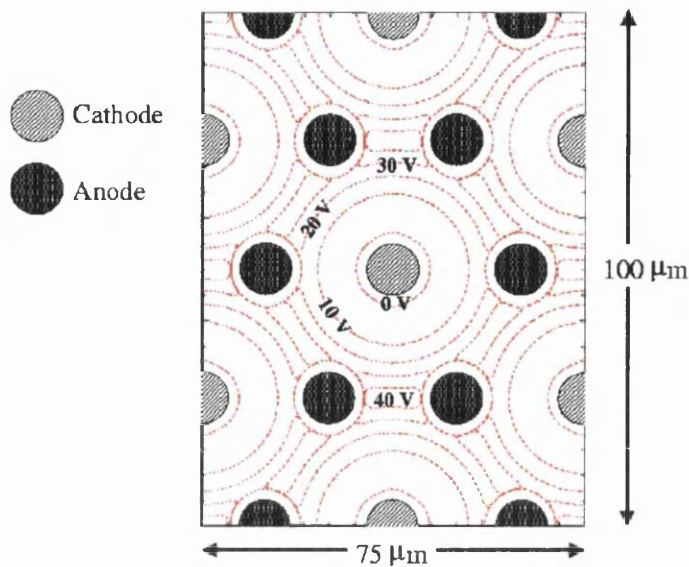


Figure 6.3: The simulated depletion regions in steps of 10 V, from 0 V to 40 V. Full depletion can be seen to occur at 50 V.

increases to 800 pA per pixel at a bias of 75 V.

6.5 Charge transport and signal formation in 3-D detectors

Charge transport in MEDICI takes into account all space charge effects including the trapping and de-trapping of charge carriers. The total current on an electrode (\vec{J}_t), is the sum of the electron (\vec{J}_e), hole (\vec{J}_h) and displacement (\vec{J}_d) currents. When electron and hole pairs are created in a detector they

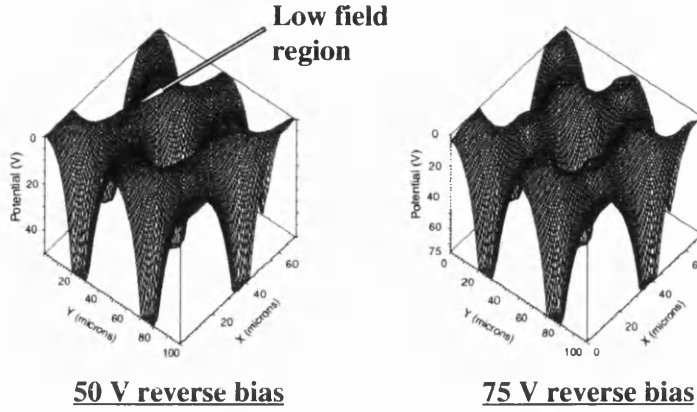


Figure 6.4: Potential profiles for 50 V and 75 V respectively.

The low E-field can be seen in the inter-electrode region.

cause a disruption of the electrostatics. This manifests itself as the displacement current and can be seen as image charge on the contact. Thus a current appears as soon as any charge is generated which leads to the sharp peak seen in figure 6.6. Ramo's theorem of image charges and weighting fields describes these currents. This is discussed in more detail in chapter 3 section 3.3.7 and supplemented in chapter 7.

The integral over time of the displacement current is zero which shows that the detection medium returns to its original state after all the charge has drifted out. The total charge, $\int \vec{J}_t \delta t$, is then equal to $\int \vec{J}_e \delta t$ or $\int \vec{J}_h \delta t$ depending upon which sign of carrier is collected at the electrode. For this case of full collection the displacement current only alters the shape of the current

6.5 Charge transport and signal formation in 3-D detectors

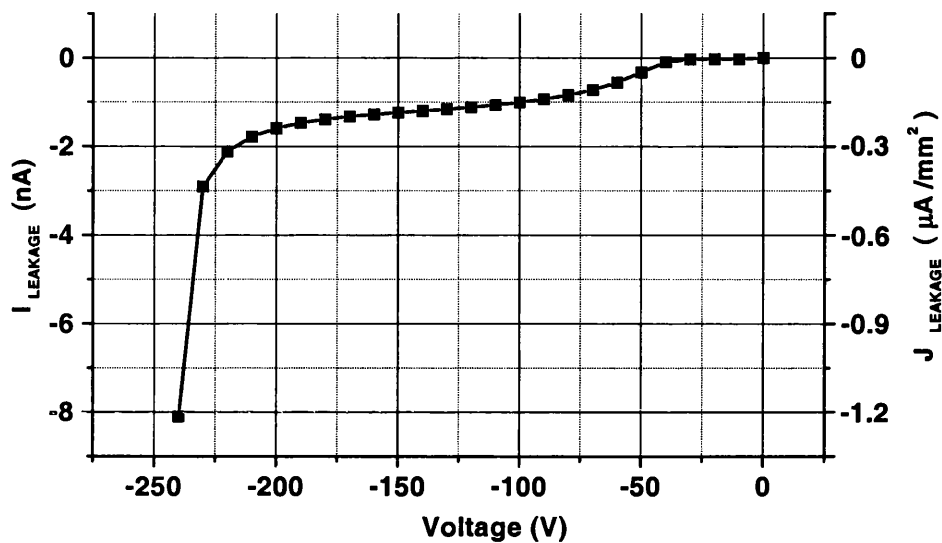


Figure 6.5: The modelled I-V characteristics for the 3-D detector structure. The reversed bias leakage current is approximately 1 nA per pixel and the device breaks down after an applied voltage of 230 V.

pulse and has no effect on the overall charge collected.

Figure 6.6 shows the current pulse resulting from 1000 e-h pairs, generated at time $t_o=1$ ns and created at point A (see figure 6.1) in a $1\text{ }\mu\text{m}^3$ volume. It illustrates that all carriers are drifted out in a time of just over 200 ps with an applied bias of 50 V. For comparison, 200 μm thick GaAs planar pixel detectors are typically operated at a bias of 300 V and collect the charge carriers in a time of the order of 10 ns.

The currents induce a charge on the electrode which can also be split into its component parts. Since in most cases semiconductor detectors are coupled

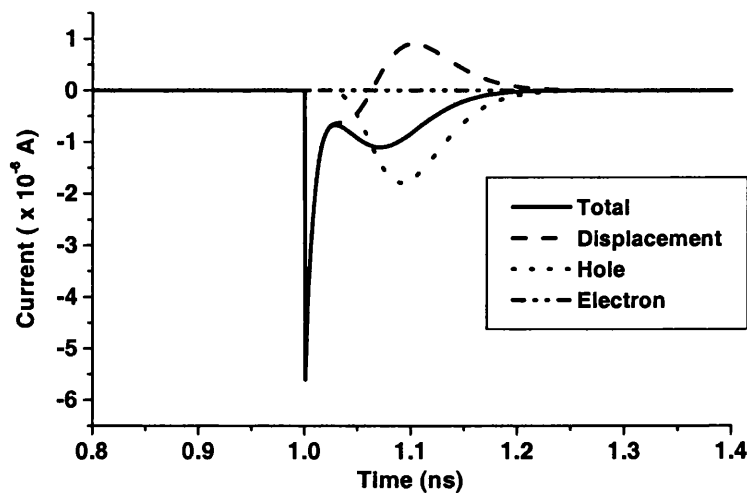


Figure 6.6: The total current pulse split into its 3 component parts.

to charge-sensitive preamplifiers (where the readout system integrates the current) the charge pulses are of particular relevance. The charge pulse corresponding to the previously shown currents can be seen in figure 6.7. Here the initial part of the pulse is due to the movement of the charge carriers and is represented by the displacement term, which starts to decrease as the carriers (in this case holes) begin to reach the contact - shown by the hole charge pulse.

6.5 Charge transport and signal formation in 3-D detectors

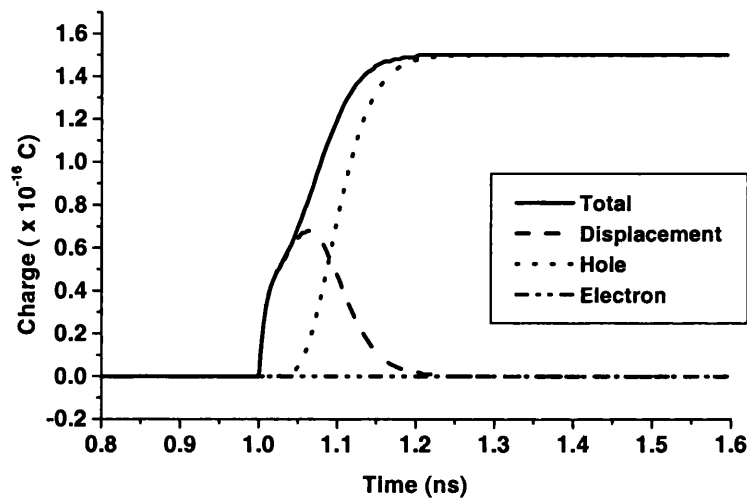


Figure 6.7: The total charge pulse split into its 3 component parts.

6.5.1 Charge transport in the low field region

In the 3-D detectors the central electrode is surrounded by six outer electrodes. These outer electrodes are all at the same bias and so the E-field between them is lower than in the rest of the device. This is a source of potential problems since the charge carriers in these regions have more time to recombine and/or be trapped. It would also lead to an increase in the time needed to collect fully the charge and so negate some of the positive aspects of these detectors. In an attempt to resolve some of these concerns 1000 electron hole pairs were generated at point B (shown in figure 6.1). The results can be seen in figure 6.8 with a comparison drawn with the previous case for

charge generation at point A (also shown in figure 6.1). It can be seen that

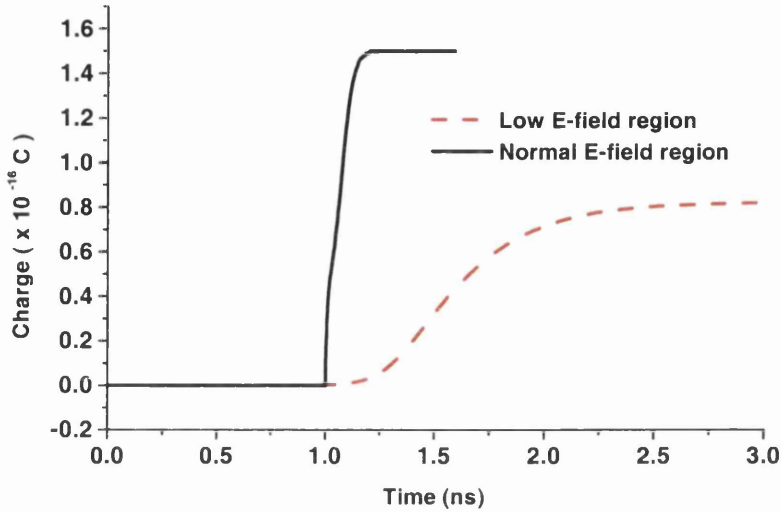


Figure 6.8: Comparison between charge pulses for the generation points A and B seen in figure 6.1.

50% of the generated charge has been collected at the electrode, due to the fact that the generation point is exactly on the pixel boundary and so the charge is shared equally between the two pixels. The charge pulse also takes considerably longer to fully develop - from 210 ps in the previous case to 2.8 ns in this case. This is as a result of the lower electric field, and is a ten fold increase in the collection time. However full collection in 2-3 ns, in a worst case, is still a factor of 4 to 5 improvement on present technologies and well within the shaping times of the proposed electronics. Furthermore, applying a higher bias voltage increases the E-field in these regions and so reduces the collection time for the carriers. This was investigated by increasing the bias

6.5 Charge transport and signal formation in 3-D detectors

voltage to 75 V and the collection time in this inter-pixel region was reduced to under a nanosecond.

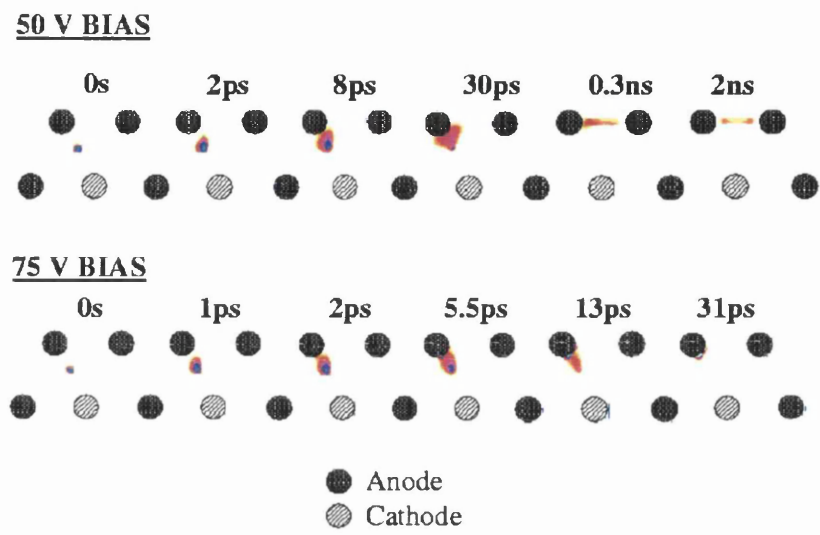


Figure 6.9: Contour plots of electron concentration for two different applied biases. For the 50 V bias case some charge can be seen to be trapped in the inter-electrode space. At an increased bias (75 V) the electrons can be seen to drift to their collection electrode and be fully collected within 31 ps.

An example of charge transport at these two operating voltages of 50 V and 75 V is shown in figure 6.9. Here the electron concentration has been logarithmically plotted as a 2-D contour plot and is shown to evolve in time (from left to right). The charge generation position is located at point A (see figure 6.1) in both cases. Each time frame shows how the electron concentration is

affected by the drift and diffusion of the generated charge carriers. For the 50 V bias condition the charge can be seen to diffuse into the low field region (see figure 6.4) resulting in a small amount of signal loss. This effect from the low field region can be seen to be minimised by over-depleting at 75 V, where all of the generated charge is collected after 31 ps. This plot indicates that it is not enough to just deplete these detectors, but that they should be over-depleted to ensure that all of the charge is fully collected.

6.6 Etch induced sidewall damage

The formation of the electrode holes is the key part in the fabrication of these detectors. Creating complex structures in GaAs has been routinely achieved using etching techniques. It is anticipated that dry etching will also have the capability to form electrodes with the high aspect ratio required. It is known, however, that these processes may damage the material by creating defects [58]. The distribution and nature of these defects has been studied and modelled with MEDICI [64], and also compared with experiment [61]. The defect profile of reference [62] has been altered to account for the radial distribution that would result in forming these holes. The distribution function is shown in equation 6.1 and has been incorporated into the MEDICI simulation of the 3D detector structures. The defect density, N_D (cm^{-3}), is given by :

$$N_D(r - r_i) = g_o \tau \left(\tau - \frac{z}{\nu} \right) \exp \left(- \frac{\sqrt{(x - x_i)^2 + (y - y_i)^2} - R}{\lambda} \right), \quad (6.1)$$

where $r = (x, y)$ and $r_i = (x_i, y_i)$. Here x_i and y_i are the central coordinates of an electrode, which has a radius of R , and z is the distance from the top

6.6 Etch induced sidewall damage

of an electrode to the depth at which the 2-D cross section is modelled, and is set at 20 μm to simulate a high damage region. This detection layer is assumed to be 200 μm thick. The etch rate, ν , is taken to be 1 $\mu\text{m}/\text{min}$, with the total etch time, τ set to 200 minutes. The term g_o is given by $\frac{J_i \alpha}{\lambda_c}$ where J_i ($= 10^{14}$ particles/ cm^2s) is the bombarding ion flux density, α ($=10^{-3}$) the probability of an incident ion being scattered into a channelled direction, and λ_c , the mean channelling distance, is $\sqrt{2}\lambda$, with $\lambda=18$ nm for the Cl^+ etch.

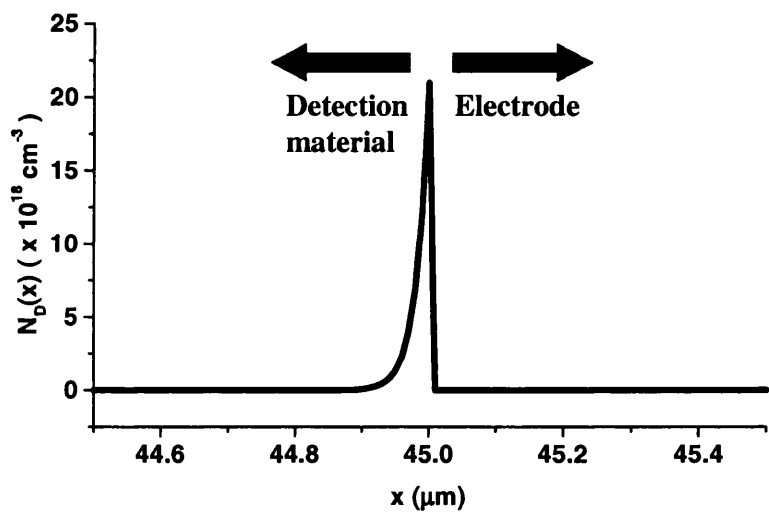


Figure 6.10: Distribution of defects caused by etching process.

The damage profile is shown in figure 6.10. It can be seen that the trap density is high very close to electrode and drops off quickly to zero within half a micron. This creates a cylinder of traps surrounding each electrode. For modelling purposes the damage is represented by one deep level donor

trap, located 0.75 eV below the conduction band. This is assumed to be the predominant recombination centre and is taken from Lootens et al [96] where they associate the trap as the EL2 level from DLTS measurements of SiCl₄ etched n-GaAs.

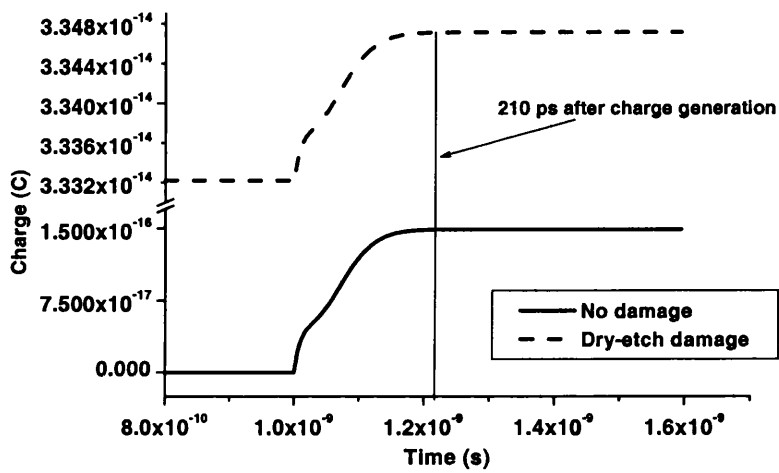


Figure 6.11: Comparison of charge pulses with (dashed line) and without (solid line) sidewall damage.

The effect this etch damage has on the charge transport in these detectors is illustrated in figure 6.11. Here the two cases of zero damage and dry-etch damage are compared. Figure 6.11 shows that the defects introduce a charge offset in the pulse, which is of the order of 3×10^{-14} Coulombs. This can be explained by the presence of a fixed space charge close to the electrode

6.7 Charge collection efficiencies (CCEs)

surface. When the defects trap an electron they become negatively charged. This means that there is a cylinder of negative space charge surrounding each electrode. This leads to a positive image charge on the electrode, resulting in the positive charge offset. The charge pulse still has exactly the same profile as previously and full charge collection is observed.

6.7 Charge collection efficiencies (CCEs)

An important parameter in any detector is its ability to collect fully all the charge that has been generated within the detection medium. Incomplete charge collection can be caused by a number of effects, such as poor material quality or radiation damage of the detection layer. The variable which must be optimised in these detectors is the mean free drift length, L . It is given by equation 6.2 and depends upon the mobility μ (cm^2/Vs) of the charge carrier, the carrier lifetime τ (s), and the electric field E (V/cm). For full collection ($> 99\%$), L should be almost 100 times larger than the distance a charge carrier has to travel from its generation point to its collection electrode.

$$L = \mu\tau E \tag{6.2}$$

In order to investigate how much improvement 3-D detectors can offer over conventional planar detectors, MEDICI simulations of both structures, which include the effects of bulk damage, were compared. This simulates the effects of operation within a harsh radiation environment. The 3-D detector geometry is as described previously. The planar detector structure is 200 μm thick and 50 μm wide. The contacts, and all material parameters are

as outlined in table 1 and are the same for both detector types. The planar detector is held at a bias of -600 V while the 3-D detector is biased to -50 V. A charge packet of 1000 electron hole pairs was generated half way between the two electrodes of differing bias for both detectors. Both structures also had a uniform distribution of deep level donors over the whole device. The lifetime of the carriers in this defect was altered in steps of 10 from 1 ps to 1 ns with an additional point at 1 μ s. For each of these simulations the CCE was calculated and the results are shown in figure 6.12.

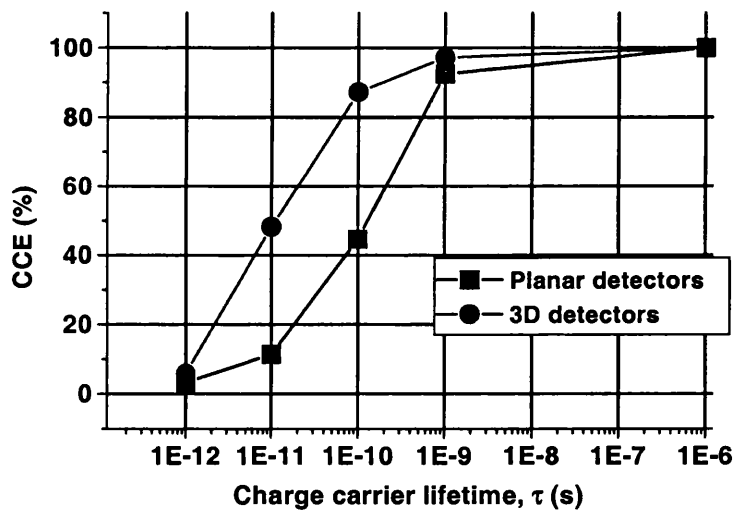


Figure 6.12: Comparison of charge collection efficiencies, as a function of charge carrier lifetime, in 3D detectors and a planar structure.

This figure shows that at high carrier lifetime (1 μ s) both detectors exhibit

6.8 Discussion

100% CCEs. However as the lifetime is reduced the CCE for the 3-D detector shows a marked improvement over the planar structure - a 43% increase at $\tau=0.1$ ns. As the lifetime is further reduced to 1 ps both detectors converge towards zero CCE since the charge carriers are trapped or recombine before they can induce significant amounts of charge.

The model for the planar detector with a charge carrier lifetime of 1 ns can be compared with the experimental results of reference [65]. Here the authors have a GaAs detector of 200 μm thickness, operated under 600 V reverse bias and with a quoted carrier lifetime of 1 ns. They report a charge collection efficiency of 96% which agrees closely with the simulated result quoted here of 93%.

6.8 Discussion

The effects of dead area, introduced by the electrodes, have been investigated by the Monte Carlo package MCNP. It was observed that for 50 μm pitch, 10 μm diameter electrodes filled with gold, 44% of the photon energy deposited in these electrodes will scatter out into the detection material. Since these electrodes cover 8% of the pixel area and each electrode can be considered 44% active the effective dead area is reduced from 8 to 4.5%. This has positive implications for charge integrating imaging detectors, but not for photon counting or spectroscopic devices.

The charge collection properties of these detectors have been investigated and full collection was observed after 200 ps in most cases. However in the lower field regions the time for all the charge to be collected is increased to 3 ns. How the charge transport is affected by dry-etch damage, resulting

from the fabrication of these structures, was examined. The trapping centres created by the etching process did not effect the charge collection but did introduce an offset in the charge pulse profile. This additional charge could introduce some noise problems if there are any temporal variations in its behaviour. The improved performance of the 3-D detectors over the planar structure, when the lifetime of the carriers is in the region 10 ps - 100 ps, gives an improvement in CCE of around 40%. This region is particularly interesting since materials with these lifetimes are currently available and radiation damage has been observed to limit the charge carrier lifetime to these values.

Chapter 7

Cadmium Zinc Telluride

7.1 Introduction

Cadmium zinc telluride (CdZnTe) is a material that offers some potential advantages over other semiconductors as a radiation detector. When compared with currently popular materials such as silicon, the effective atomic number of CdZnTe leads to an increased detection efficiency at higher gamma ray energies. Another advantage is the band gap of 1.572 eV which allows room temperature operation, as opposed to germanium which needs expensive cryogenic cooling to operate as a spectrometer.

In this chapter the commercial simulation package MEDICI has been used to analyse the charge transport behaviour of a pixellated device made from such a material. The Monte Carlo package MCNP is used to generate the charge cloud profile due to incident photons. This can be incorporated into MEDICI and allows a complete analysis of charge sharing - from the photon interaction to the subsequent charge transport.

7.2 Background

The commercial successes of cadmium telluride (CdTe), as a gamma ray spectrometer within the medical and industrial fields, has led to great interest in the related compound cadmium zinc telluride (CdZnTe). The zinc is added to increase the resistivity and so lower the leakage current. However CdZnTe suffers from the same problems found in many compound semiconductor detectors, namely high defect concentrations leading to short mean free paths and so incomplete charge collection. CdZnTe has a particularly low hole mobility (see table 7.1) which adversely affects its detector performance. This problem has in some cases been marginalised by the use of highly pixellated devices [66], but these bring their own problems such as complexity of design and charge sharing.

The most recent and most promising method of producing detector grade CdZnTe is the high pressure Bridgeman (HPB) technique. In this method a bulk crystal is grown from a melt of the constituent elements. The method was originally devised to produce better matched substrates for $\text{Hg}_{1-x}\text{Cd}_x\text{Te}$ epilayers used as infrared detectors. The melt is contained within a crucible and moved through an axial temperature gradient in a vertical or horizontal furnace. An alternative to moving the crucible or furnace is to alter the temperature profile to achieve the same effect. Defects can arise due to the difference in vapour points that exists between Cd and Te. To combat this the melt is usually enclosed in a crucible made from quartz, carbon coated quartz or graphite. The vapour point of Cd is significantly lower than that of Te, and one of the advantages that CdZnTe offers over CdTe is that the Zn settles into the Cd vacancies, maintaining the crystal structure. The

7.3 Material Simulations

HPB growth process is usually held under a pressure of around 100 atm to reduce the evaporation of Cd. The progress in producing detector grade CdZnTe material has been substantial over the last few years. The material has become commercially available through dedicated crystal manufacturers, such as eV Products. Some articles which cover the growth of these crystals in more detail are [74], [75], and [69].

7.3 Material Simulations

Cadmium zinc telluride is typically operated as a photoconductive detector. A detector in this form operates with injecting contacts on either side of the semiconducting material. The bias applied creates a uniform E-field across the device which has a measurable current defining the material resistivity. The most common contacts fabricated on CdZnTe are gold, which adheres well to CdZnTe and historically has also been used for the related compound CdTe. The processes are well developed and in common use [70]. The important material parameters for CdZnTe are outlined in Table 7.1. In terms of contact formation, the affinity and band gap are the important values. For charge transport, the carrier lifetimes and mobilities are the dominant terms.

The values shown in table 7.1 have been taken from reference [69] and are the numbers quoted for CdZnTe grown by the high pressure Bridgeman (HPB) technique, from the suppliers eV Products. The exception is the electron affinity of CdZnTe, which is from reference [70]. There is substantial literature quoting various values for these parameters; however, the crystal with which the model will be compared is of the same type and grown by

Table 7.1: The material values used to model CdZnTe.

Parameter	Value
Atomic numbers	48, 30 , 52
Density (g/cm ³)	5.78
Energy / electron-hole pair (eV)	4.64
Bandgap E_g (eV) at 300 K	1.572
Molar fraction	Cd _{0.9} Zn _{0.1} Te
Electron lifetime τ_n (s)	3×10^{-6}
Hole lifetime τ_p (s)	1×10^{-6}
Permittivity	10.9
Affinity (V)	4.3
Electron effective mass	0.09
Hole effective mass	0.65
Electron mobility (cm ² /Vs)	1000
Hole mobility (cm ² /Vs)	80

the same manufacturers.

7.3.1 Defects and trapping centres

The development of growth techniques that can produce low defect densities and high resistivity CdZnTe at large crystal dimensions is currently a major research area. As a result there is not a great deal of information on the defect states within CdZnTe. The work that has been done indicates that the parameters not only vary from crystal to crystal, but also from one

7.3 Material Simulations

area of a crystal to another [71]. It also indicates that there are many defect states distributed throughout the band gap in concentrations of around 10^{16}cm^{-3} . Some of these defects are native in origin, while others are impurity atoms such as Al, Cu, Fe and C. The compound material CdTe has been investigated more thoroughly [72] and it is expected that many of the native defects, such as vacancies and interstitials, will also be present in the related material CdZnTe. The crystals used for comparison are slightly n-type and exhibit properties typical of this material. The defect centres included in this model are detailed in table 7.2 where the energy level, concentration and an attempted assignment to known crystal defects are shown. There exists a great deal of variation, as well as debate, on the levels actually present in the material. The reasons for selecting these defect levels are threefold :

- they are referred to in much of the literature [73] [74] [75] [76],
- they allow the modelled material to be slightly n-type with a Fermi level pinned close to the mid-gap,
- they give the correct I-V characteristics as shown in figure 7.1.

The formation of grain boundaries, defect clusters and the presence of precipitates play a significant role in the material development of detector grade crystals. These effects, being on the macroscopic scale, are not included in the models below. The simulations describe the behaviour of a uniform material, which has been one of the goals of CdZnTe material development for many years. Also neglected is the presence of surface states which may play a role in the pinning of the Fermi level at the surface.

Table 7.2: Defect levels incorporated into simulations.

Energy (eV)	Concentration ($\times 10^{16} \text{ cm}^{-3}$)	State	Possible cause
$E_C-0.67$	0.9	Donor	Cd_i^{++}
$E_C-0.75$	0.9	Donor	Te_{Cd}
$E_C-0.86$	1	Donor	Metal impurity
$E_C-1.1$	1	Donor	V_{Te}^+
$E_V+0.35$	0.1	Acceptor	Zn related
$E_V+0.14$	0.1	Acceptor	$(\text{V}_{Cd--}, \text{X}^+)^-$

7.3.2 Experimental Comparison

The I-V plots in figure 7.1 are from a real $10 \text{ mm} \times 20 \text{ mm} \times 2 \text{ mm}$ crystal with gold contacts fabricated on each side of the $10 \text{ mm} \times 20 \text{ mm}$ plane¹. The commercial modelling package MEDICI [15] was used to simulate the electrical properties of a 2-D section (in the $10 \text{ mm} \times 2 \text{ mm}$ plane) of this structure. The defect levels of table 7.2 are included in this material simulation. The experimental and modelled I-V curves were matched by altering the defect concentrations, though these concentrations were kept close to the typical values of 10^{16} cm^{-3} [71]. These defect levels at these concentrations give approximately the correct currents for a given voltage, the slight alteration of the concentrations allows the match to be more accurate. The contact parameters also have an influence upon the I-V characteristics as will be discussed next.

¹Courtesy of K. Valpas of Metorex Int.

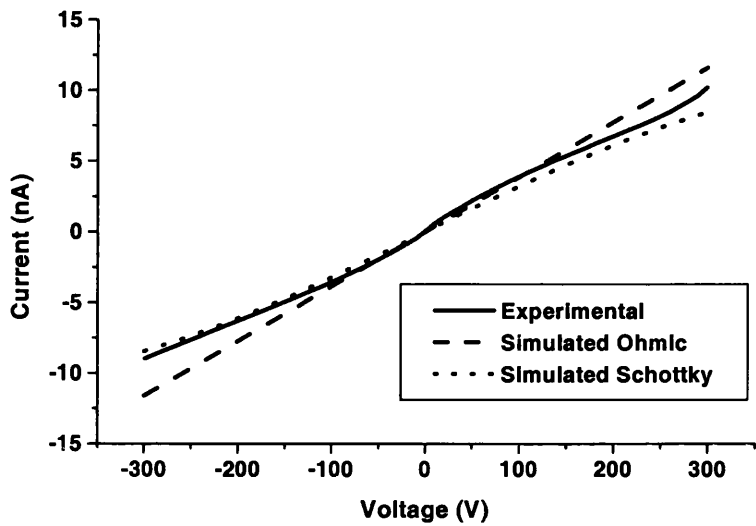


Figure 7.1: Comparison of experimental and simulated current-voltage characteristics with different contacts and the trap concentrations of table 7.2.

The first simulations included gold contacts by specifying the workfunction of the metal to be 5.1 eV [77]. This gave the dashed line shown in figure 7.1 (denoted simulated Schottky), which is in close agreement with the experimental data (solid line). Though this agrees well with experiment, it is important to look at the profile of the electric field through the depth of the detector. This is shown in figure 7.2 where it is compared with the pure ohmic case. The model with Au contacts clearly exhibits an electric field profile typical of slightly Schottky behaviour, though much of the literature supports the ohmic nature of such a contact [72]. This is due to the fact that the workfunction of the metal, ϕ_{metal} , is greater than the workfunction

of the semiconductor, ϕ_{semi} ($\phi_{metal} < \phi_{semi}$ is required for ohmic contacts on n-type materials).

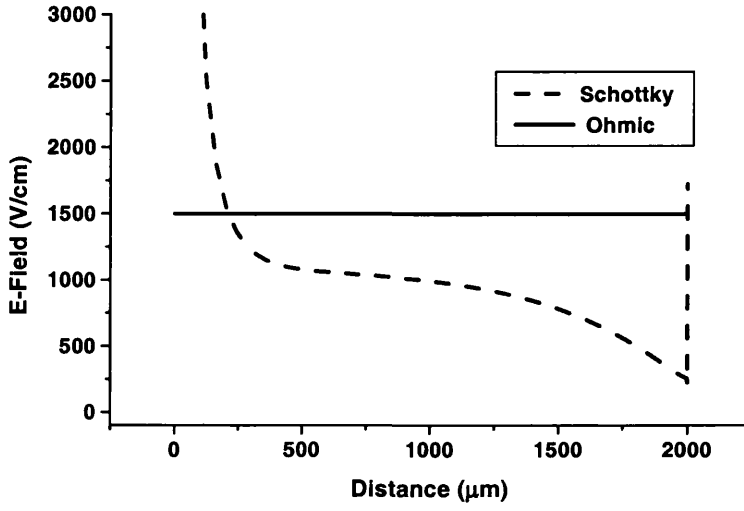


Figure 7.2: Electric field profiles for the two simulated contact conditions.

Since many articles report the ohmic properties of gold electrodes on CdZnTe, the model was altered to have injecting contacts. The resultant I-V curve is shown as simulated ohmic in figure 7.1. This plot also matches closely the experimental data, however the E-field plots (figure 7.2) show two substantially different profiles. This shows that from the simulated data it is not possible to determine the nature of the contacts by the linearity of the I-V curves, as is commonly done experimentally. The impact this will have on detector behaviour will be discussed later in this chapter.

7.4 Charge transport

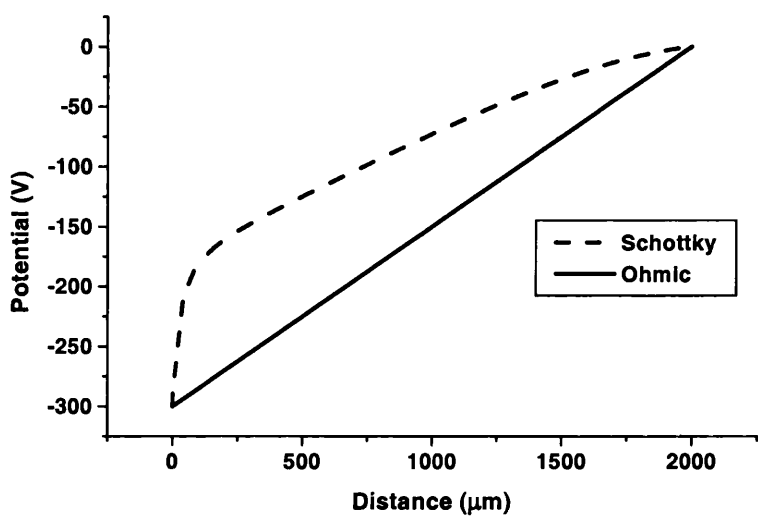


Figure 7.3: The simulated potential profiles for the two contact cases

7.4 Charge transport

The physical processes modelled in this section are signal generation, X- and γ -ray interactions, charge spreading and sharing and the effect that defects have on these phenomena. The first case that will be examined is the signal formation in terms of current and charge pulses.

7.4.1 Signal generation

CdZnTe spectrometers are commonly employed as high energy γ -ray detectors, usually above an energy of 100 keV, though lower energy X-ray detection is becoming possible through continued material improvements. The

thickness of the detection material is limited by charge transport. Typical thicknesses are 1 to 2 mm, this being a trade off between the absorption efficiency of the incident photons and the charge collection efficiency of the generated carriers. These carriers will have a large distance to travel, in comparison with conventional Si pixel detectors of thickness $300\text{ }\mu\text{m}$. The presence of the defects discussed earlier will lead to trapped charge and so incomplete charge collection. Hole transport will be affected, in particular. The low hole mobility leads to an increased trapping cross section and poorer spectral performance. Low energy tails are often seen in the photopeaks of spectra taken with CdZnTe detectors - corresponding to incomplete charge collection. Various methods have been employed to reduce this effect :

- the small pixel effect [66],
- corrections for interaction depths [40],
- pulse rise time discrimination [68]
- unipolar sensing [67].

The drawbacks of hole transport are evident in the following simulations. Charge was generated, in separate 2-D MEDICI simulations, at 3 points within the detection medium : $3\text{ }\mu\text{m}$ from the cathode, in the middle of the device and $3\text{ }\mu\text{m}$ from the anode (see figure 7.4). The material is of the type described previously in section 7.3 and the cross sectional dimensions of the device are 1 mm by 2 mm. 1000 e-h pairs were generated within a volume of $1\text{ }\mu\text{m}^3$. The ohmic contact case was chosen, with a voltage of -300 V applied to the cathode, since this E-field profile leads to less complicated current and charge pulses.

7.4 Charge transport

The motivation for these studies is to understand how the interaction depth affects the charge pulse and so the energy that the electronics detects.

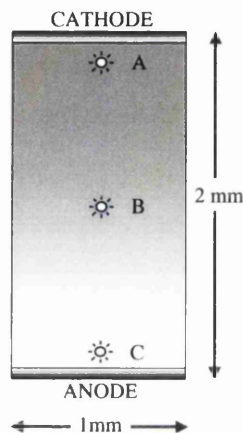
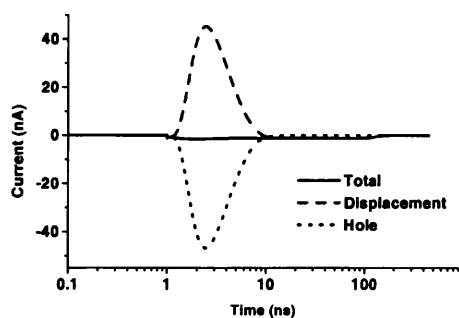


Figure 7.4
Positions of charge generation. Point A is $3\text{ }\mu\text{m}$ from the cathode, point B is exactly in the centre of the detector and point C is $3\text{ }\mu\text{m}$ from the anode.

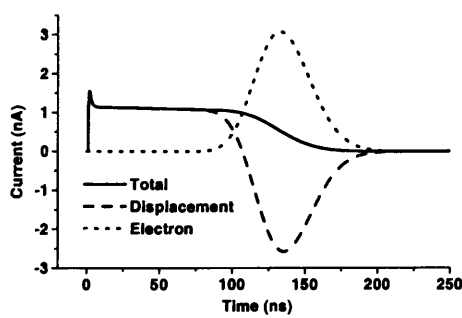
The current and charge pulse shapes can be analysed by splitting the total contribution into its constituent parts, thus allowing the time evolution of the charge carriers to be investigated more deeply. This has been done for the three cases outlined above.

Figure 7.5 shows the current and charge pulses for both contacts (the anode and the cathode) for the first case where the charge is generated $3\text{ }\mu\text{m}$ from the cathode. This could represent the interaction of a X-ray, where the photons are incident on the cathode and the carriers chosen to be collected at the read-out electronics are electrons. The definitions of these current and charge terms have already been discussed in chapter 3 section 3.3.7.

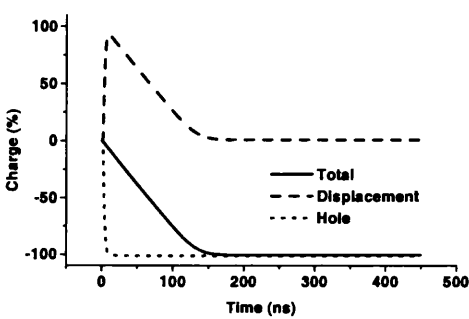
The total current on the cathode is due to two components - the hole conduction current (J_h) and the displacement current (J_d). The hole conduction current is simply the holes entering the contact. It begins almost immediately



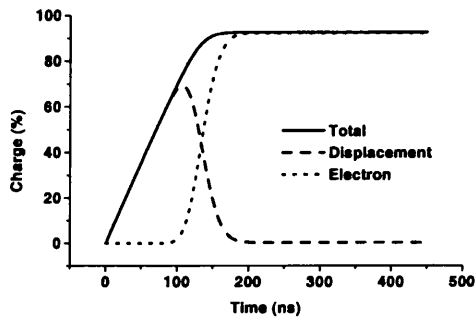
(a) Current pulse on cathode



(b) Current pulse on anode



(c) Charge pulse on cathode



(d) Charge pulse on anode

Figure 7.5: The total current and charge pulses, for both contacts, split into their component parts. Here the charge is generated $3\text{ }\mu\text{m}$ from the cathode.

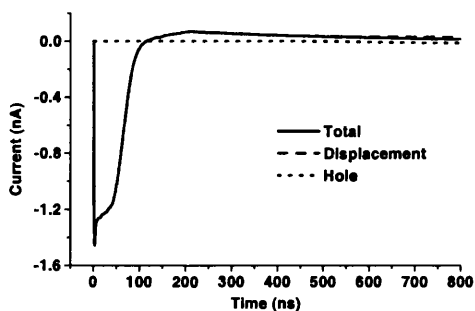
after the charge is generated and ends after 10 ns, when all of the generated holes are collected. The displacement current is more complex. The initial displacement current pulse consists wholly of displacement as no holes have yet arrived at the contact. The positive charge cloud creates a displacement on the cathode. J_d then changes sign since, as the holes leave, the electrons are still contained within the device. This then leads to a polarisation of

7.4 Charge transport

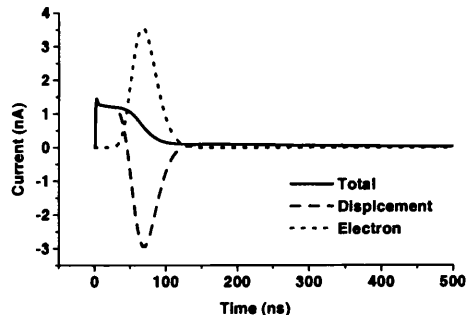
the detector medium, creating a displacement current that increases for every hole that leaves the device. So there is a hole conduction current being cancelled out by the displacement caused by the holes leaving the device. However there is also an electron displacement current (J_e) flowing in the opposite direction, leading to a net total current in the direction of J_h (since holes flowing in one direction and electrons flowing in the other give the same current). The effect these carrier dynamics have on the charge pulse can be seen in figure 7.5 (c). Here the charge pulse due to the conduction carriers (on this contact they are holes) is complete after 10 ns. However the resultant displacement current leads to a current in the other direction. This causes the charge pulse to increase slowly as the displacement, D , decreases. Finally D returns to zero when full collection is achieved (ie. when all the electrons also leave the device).

The electron current pulse of figure 7.5 (b) is more easily understood, since the holes have been collected long before the electrons start arriving at the anode. The electrons induce a current on the anode as they travel towards it. As the electrons are collected the displacement current is reduced, and as the displacement caused by these carriers begins to fall so J_d becomes negative. All currents fall to zero after the final electron has been collected. Figure 7.5 (d) shows the corresponding charge pulse for the anode.

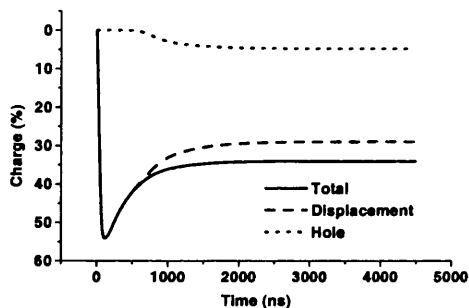
The next case, where charge is created in the middle of the device, leads to the plots shown in figure 7.6 which look very different but can be described by the same principles. In this case both carriers have the same distance to travel, 1 mm. As has been mentioned previously the carrier lifetime of



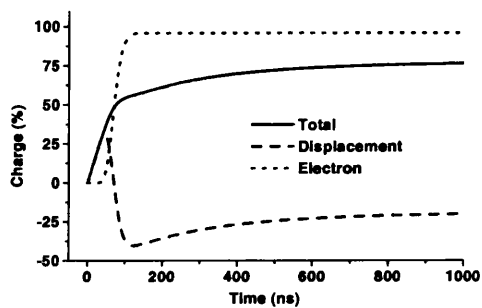
(a) Current pulse on cathode



(b) Current pulse on anode



(c) Charge pulse on cathode



(d) Charge pulse on anode

Figure 7.6: The total current and charge pulses, for both contacts, split into their component parts. Here the charge is generated in the middle of the detector.

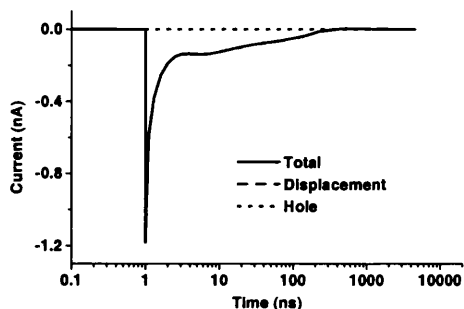
the holes is approximately three times less than that of the electrons, and the hole mobility is also more than a factor of ten less than the electrons. The lower mobility leads to the drift velocity of this carrier being lower and as a result the holes travel a shorter distance than the electrons, over the same time period. For example in 100 ns the holes travel 120 μm , from a simple calculation using $v_{drift} = \mu E$ with $v_{drift} = \frac{d_{drift}}{t_{drift}}$. The electrons will

7.4 Charge transport

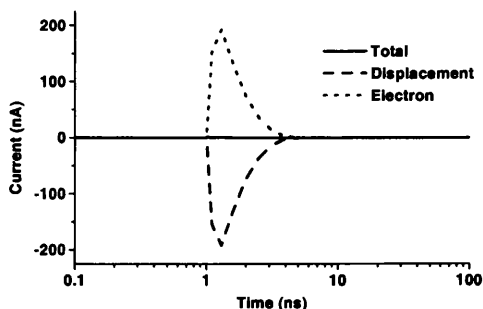
travel a corresponding distance of 1.5 mm in this time. So in 100 ns most of the electrons are collected (see electron conduction current in figure 7.6 (b)) whereas the holes have only travelled one tenth of their collection distance towards the cathode.

The result is the total current on the cathode being due to the displacement current (caused mainly by the movement of the electrons). However when the electrons have left the detector, the holes create a displacement current in the opposite direction. On the cathode this leads to a positive lobe on a previously negative current. On the anode the result is a negative displacement current on a previously positive current, which is being counteracted by the electron conduction current. The effect that this has on the charge pulses is different for both contacts. The cathode charge pulse (figure 7.6 (c)) increases initially to a collected charge of 55% before the electrons are fully collected and the displacement current changes sign. The charge is then drained off until all of the holes are either collected or trapped (no holes are moving). When the holes are trapped the result is a fixed charge in the bulk of the detector and so the displacement charge does not return to zero, indicating that the material has not returned to its initial state (i.e. the material is polarised). These holes will slowly de-trap creating a very small current over a long time. The result is a charge loss of 60% on the cathode after 1 μ s, while the charge pulse on the anode reaches 70% of full collection in a similar time (figure 7.6 (d)). This pulse shows clearly the fast rise in the pulse due to electrons and the slow component due to the motion of the holes detrimentally affecting the charge collection.

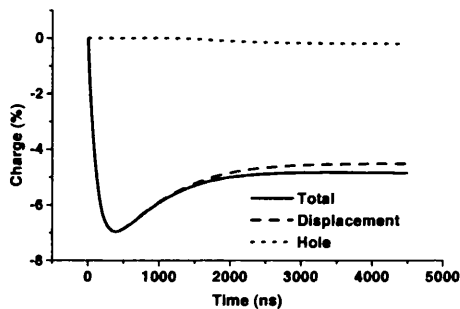
The final case of charge generation 3 μ m from the anode, is the worst case in



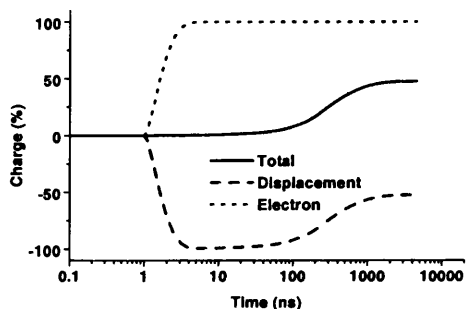
(a) Current pulse on cathode



(b) Current pulse on anode



(c) Charge pulse on cathode



(d) Charge pulse on anode

Figure 7.7: The total current and charge pulses, for both contacts, split into their component parts. Here the charge is generated $3 \mu\text{m}$ from the anode.

terms of charge collection. The carriers with smallest mean free drift length, the holes, are travelling the largest distance, while the electrons with their far greater charge collection properties are travelling only $3 \mu\text{m}$. The cathode current is due almost entirely to the displacement current with less than 1% of the holes actually being collected as a conduction carrier on the electrode. The current from the electrons is seen as a displacement current on the cath-

7.4 Charge transport

ode. These electrons are collected in 4 ns (see figure 7.6 (b)) after which the current on the cathode is due to the induced current from the movement of the holes. As the holes are moving very slowly and being trapped very quickly the current is small and continues to decrease. Once these holes are all trapped they set up a displacement charge within the detector, which is felt by the charge on the cathode. The current then flows back across the contact reducing the charge on the cathode and increasing the charge on the anode.

The results can be summarised by stating that the low mobility and lifetime of the holes in CdZnTe lead to a collected charge which is highly dependent upon the interaction point of incident radiation. These examples indicate that for charge generation close to the cathode full charge collection can be accomplished within 200 ns, for a 2mm thick CdZnTe detector of this type. This charge collection degrades to 70% seen on the anode after 1 μ s and 40 % on the cathode after the same time. The worst case is for charge generated close to the anode. The charge on the anode reaches 50% after 5 μ s with only 5.5% of the total charge generated being seen on the cathode after this time has elapsed.

7.4.2 Charge sharing

X-ray interactions

When an X-ray interacts in a semiconducting material it will create e-h pairs within a small volume - around 1 μ m³ - providing the energy of X-ray is tens of keV or less. If a 20 keV photon was incident in CdZnTe it would

liberate some 4000 e-h pairs in such a volume. To examine the response of a CdZnTe pixellated detector to incident X-rays, MEDICI was used to simulate a section through such a device. The material characteristics of the previous simulations were kept, so the time dependent charge trapping and de-trapping is included. Since photons in this energy range will not penetrate far into a semiconductor with such a high Z-number, the charge was created at a distance of $3\text{ }\mu\text{m}$ from the cathode of the modelled detector. The density of carriers was set to 1000 e-h pairs contained within a volume of $1\text{ }\mu\text{m}^3$. A schematic representation of the model is shown in figure 7.8.

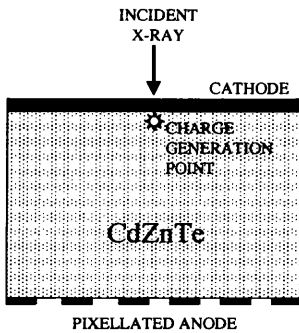


Figure 7.8

Schematic representation of method for determining the distribution of a charge cloud at the anode contact.

The charge packet is generated just below the cathode, which is biased at -300 V for the 2 mm thick CdZnTe detector. For the ohmic contacts this gives a constant electric field of 1500 V/cm across the whole device, as in figure 7.2. The anode side is pixellated with a pixel pitch of $40\text{ }\mu\text{m}$ and is held at ground. The electrons and holes will separate under these conditions, with the electrons drifting down to the anode while the holes drift towards the cathode. The pixellated side allows the spreading of the charge packet to be examined by taking the integral of the electron current on each pixel and subtracting off the leakage current contribution. This gives a Gaussian distribution centred around the point of charge generation. The

7.4 Charge transport

sigma of this Gaussian can be used to quantify the charge spreading as a function of distance for both the ohmic and Schottky contact cases. This was modelled for the case of 200 μm , 1 mm and 2 mm thick detectors, the Gaussian distributions of which can be seen in figure 7.9, for the case of the Schottky contacts. Similar profiles were obtained for the ohmic contacts,

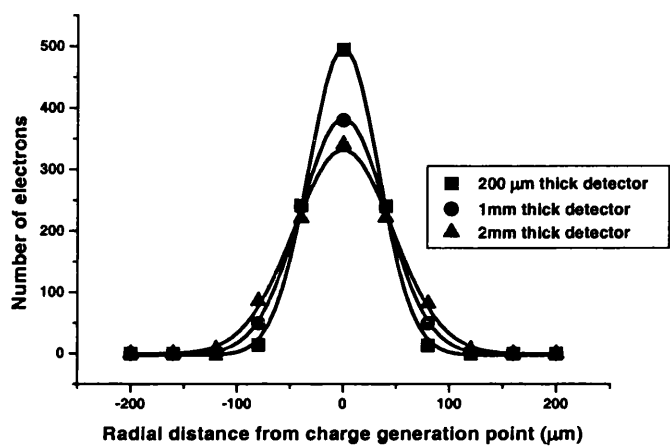


Figure 7.9: The Gaussian distributions for the Schottky contact case. Three thicknesses of detector are shown.

but these distributions are narrower than their Schottky counterparts. Since the electric field for the ohmic case is at higher value for most of depth through the CdZnTe detector the charge has less time to diffuse outwards and the result is a narrower Gaussian distribution. Figure 7.10 shows how the sigma value for the distributions changes with depth for the two electric field configurations. For the ohmic contacts the pixel size was reduced to 2 μm pitch, ensuring that enough points were obtained for an accurate Gaussian fit.

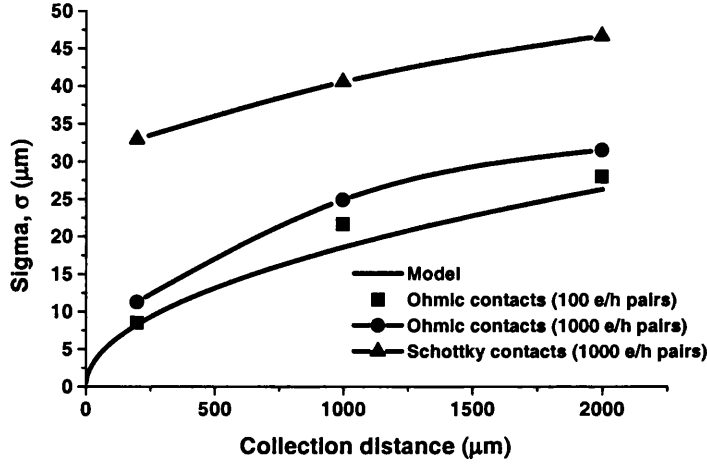


Figure 7.10: The sigma of the Gaussian distributions for the different charge generation points (see figure 7.4) and electric field conditions (see figure 7.2). The single line (denoted Model) corresponds to the variation of the sigma given by equation 7.1.

Also shown is a plot of a simple model which has been taken from reference [78], where the derivation and approximations are outlined. The model has been altered to consider the case of the constant E-field, E , observed in figure 7.2. The form of the equation can be seen in (7.1) and predicts the sigma, σ , of the Gaussian in as a function of the distance, d , travelled by the charge packet.

$$\sigma^2 = \frac{2kT}{q} \frac{d}{E} \quad (7.1)$$

It can be seen that there is poor agreement between the model and the simulation results when 1000 e-h pairs/ μm^3 are transported. This is attributed

7.4 Charge transport

to plasma effects due to Coulomb repulsion compounding the diffusion of the charges [78] and [79], leading to the increased width of the Gaussian distributions. To examine whether this simplified model can predict the shape of the charge cloud in the material modelled, the simulations of reference [79] - where the charge concentration is less and a good agreement is observed - were repeated. As can be seen in figure 7.10, the model and the simulation match extremely well when the distance travelled by the charge carriers is at its smallest ($200\text{ }\mu\text{m}$). At larger distances the agreement is not so close and this may be attributed to the increased effect that defects have as distance travelled to the collecting electrode increases. The value of the sigma after charge transport is the only parameter required, if a good Gaussian fit to the data is obtained, to allow charge sharing to be investigated.

If the Gaussian profile obtained is then rotated around 180 degrees, a cone will be formed which represents the charge profile of an X-ray interaction in 3 dimensions (see figure 7.11). This 3-D profile depends upon the value of the sigma and so is dependent also upon the contact technology and the distance travelled by the charge carriers. Such a profile was calculated for the ohmic and Schottky contacts for the 3 thicknesses of detector discussed previously.

To analyse charge sharing this new profile has to be integrated over the width and length of the pixel. Therefore, the contribution from point sources integrated over the pixel dimensions gives the response of a uniformly illuminated pixel. Since the pixel boundaries are known, any charge which is outside these boundaries is lost to the neighbouring pixels. A plot of this integration over

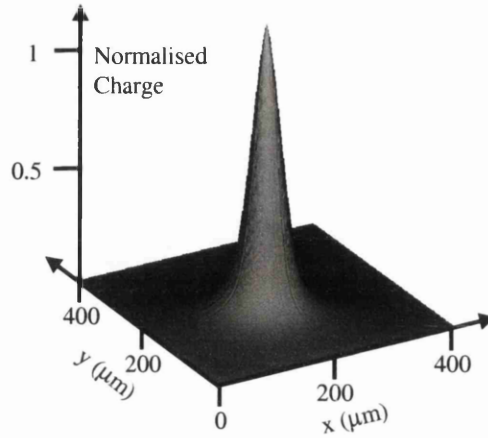


Figure 7.11: The radial distribution, after charge transport, rotated around the charge generation point.

pixel width and length, of the distribution of figure 7.11, for a square pixel of pitch $500\text{ }\mu\text{m}$ is shown in 7.12. This procedure can be repeated for a range of pixel sizes, which then allows a plot of pixel size against collected charge to be obtained. Graphs 7.13 and 7.14 show these results for X-rays interacting in three thickness of CdZnTe with differing contact properties.

Gamma ray interactions

The interaction of higher energy γ -rays in CdZnTe is fundamentally different to that of the X-ray interaction just discussed. It involves the Compton effect and at even higher energies, pair production. The photoelectron will also travel much further, since it will be of significantly higher energy. These differences mean that the interaction cannot be represented by the creation

7.4 Charge transport

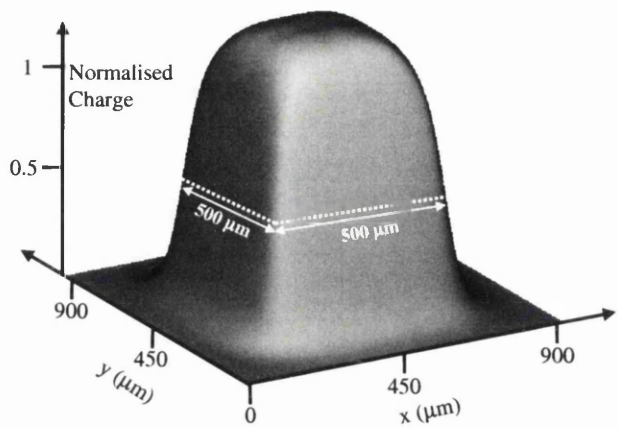


Figure 7.12: Integration of charge response over pixel width and length for a square pixel of 500μm side.

of charge carriers at a point, as was the case previously. To analyse the gamma ray interaction, use was made of the Monte-Carlo package MCNP [16]. The interaction which has been investigated here is that of the 662 keV gamma ray that results from the decay of Cs-137 to Ba-137. Caesium is a radioisotope that arises as a by product in the nuclear industry. The detection of the substance is vital in allowing nuclear decommissioning to occur safely. Current detectors utilise CsI scintillators with large collimators to allow spectral and positional information to be achieved. A CdZnTe pixel array could offer an attractive alternative, allowing little or no collimation and so offering a more portable device. The analysis discussed previously can be employed to see what effect charge sharing has in devices of this type. There are many motivations for the development of pixellated spectroscopic devices. They offer a reduced capacitance, and so noise, due to their smaller

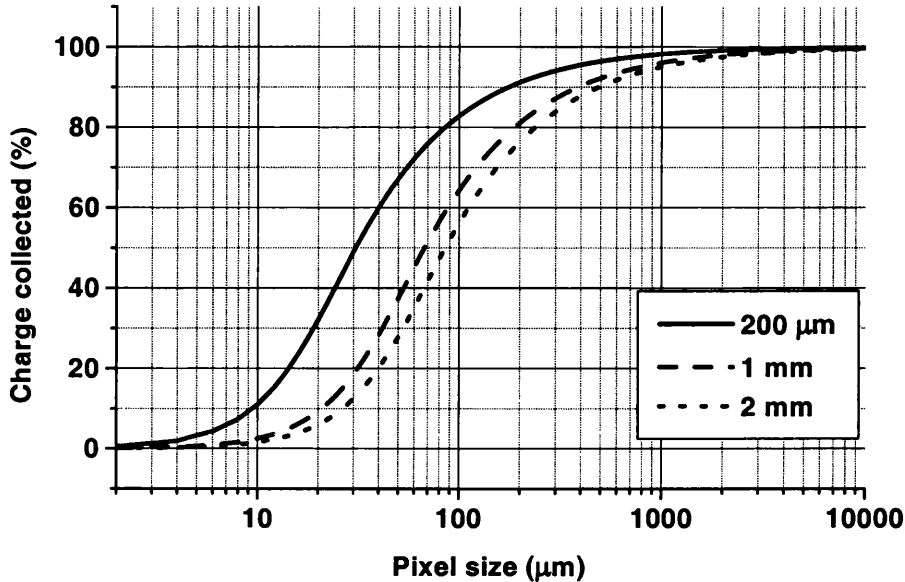


Figure 7.13: The charge collected at ohmic pixels as a function of the pixel size, for soft X-rays on CdZnTe.

electrode area. The leakage current is divided between the segmented electrodes and gain corrections can be applied to account for variations in material properties across the crystal. Each pixel will have its own read out chain leading to a corresponding increase in rate capabilities and imaging applications can be realised. Sharing of charge between pixel electrodes has implications on all of these.

The analysis of charge sharing at these energies (where the interaction cannot be considered point like) starts with the averaged charge cloud obtained from MCNP. If a point source of 662 keV photons is incident upon a block of CdZnTe, then the average energy deposition for many particles can be calculated by this Monte Carlo method. This shows where a 662 keV pho-

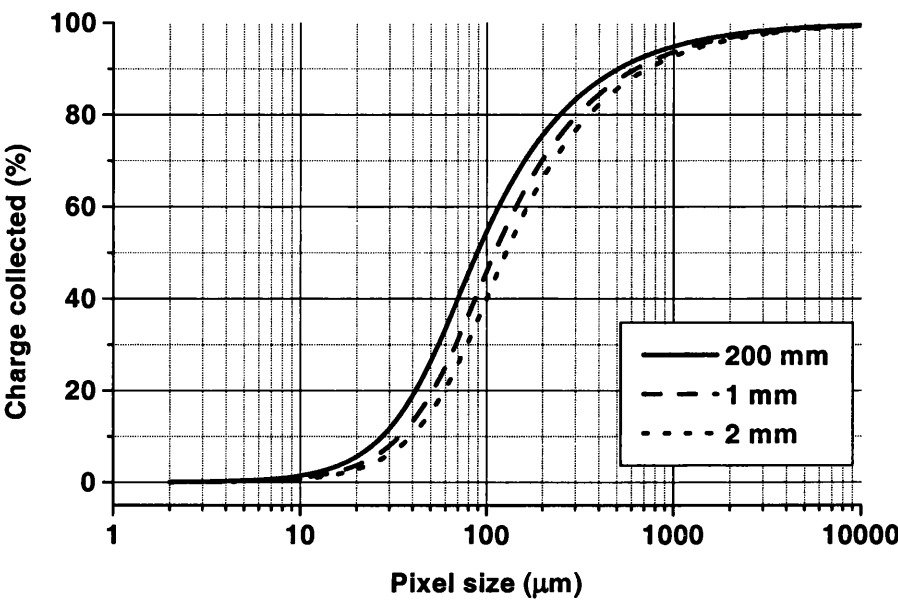


Figure 7.14: The charge collected at Schottky pixels as a function of the pixel size, for soft X-rays on CdZnTe.

ton will *on average* deposit its energy in the crystal. If a 1 μm slice (in the y-direction) is plotted it will give the profile shown in figure 7.15, where the energy deposited is shown as a function of penetration depth and radial distribution. This figure illustrates that the radial distribution of energy loss extends no further than approximately 100 μm from the interaction axis and that 95 % of this energy loss occurs within 10 μm of this axis.

This distribution can be incorporated into the MEDICI modelling package which allows an analysis of the charge transport contribution to the width of the charge cloud. It should be noted that this method is not the same as calculating the individual responses of each incident photon. The averaged response from MCNP was the result of 2 million particles, so the MEDICI

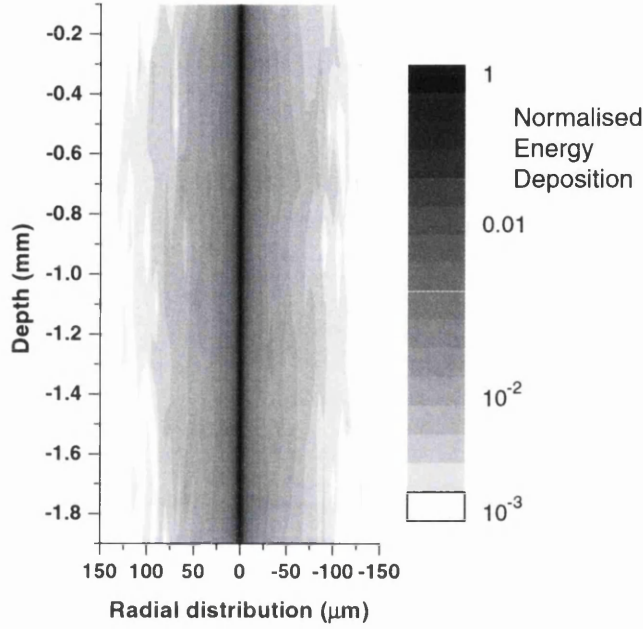


Figure 7.15: The averaged response of 2 million 662 keV photons in 2mm CdZnTe, from MCNP simulation.

simulation transports the charge generated from all of these particles in one simulation. However if the concentration of the electron-hole pairs is sufficiently low then there will be no interaction between the generated charge, as was seen for the case of 100 electron-hole pairs in $1 \mu\text{m}^3$. Therefore the charge density was kept below the $1 \times 10^{15} \text{ cm}^{-3}$, above which Coulomb interactions were observed, for the simulations of the charge cloud derived in MCNP. This is valid since a 662 keV γ -ray will create at most 1.42×10^5 electron-hole pairs in CdZnTe. Since the volume has increased to around $10 \mu\text{m}^3$, this leads to around 1.42×10^{14} carriers per cm^3 .

The modelled response of the detector to this charge does not contain any temporal information, but the relative magnitudes of the charge on the pixels

7.4 Charge transport

allows an analysis of charge sharing. Figure 7.16 shows the broadening effect

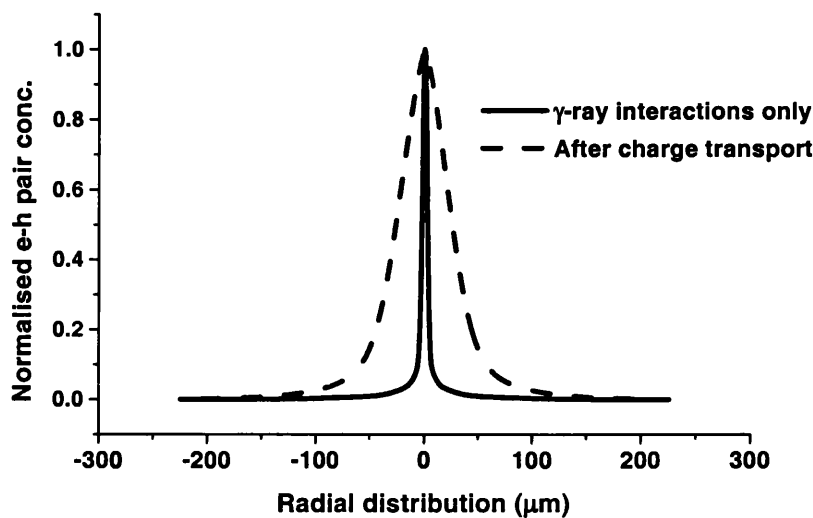


Figure 7.16: Radial distributions for the charge cloud generated by the γ -ray interaction before and after charge transport, for the case of ohmic contacts.

that the charge transport has on the distribution obtained from the gamma ray transport. The profile after charge transport gives the final width for a point source of 662 keV photons incident on 2 mm of CdZnTe. It can also be seen from this figure that, even at these high gamma ray energies, the diffusion of the charge cloud is the dominant effect in broadening the distribution. This profile can then undergo the same process as the Gaussian profiles for the X-ray interaction, allowing charge sharing to be analysed for this case also. The corresponding graph can be seen in figure 7.17.

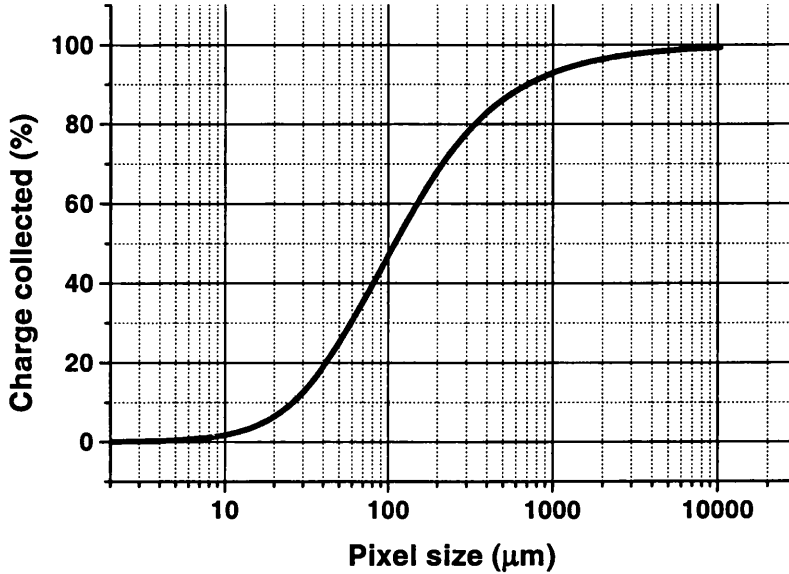


Figure 7.17: The charge collected at a pixel as a function of the pixel size, for 662 keV photons on 2 mm thick CdZnTe.

7.5 Summary

It has been shown by MEDICI modelling of CdZnTe detectors, that gold contacts can give both ohmic and Schottky contacts on the same material. Though the I-V characteristics of these contacts look very similar, their modelled electric field profiles are very different. A metal with a lower workfunction, such as indium, would eliminate any possibility of Schottky contacts forming, where ohmic contacts are desired.

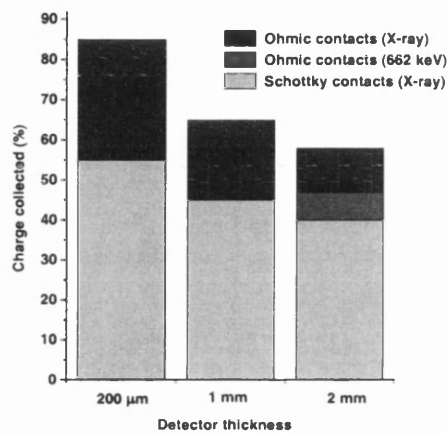
A simple diffusion model adapted from reference [78] is sufficient to predict accurately the charge cloud profile for low carrier densities at short collection times. At these short charge collection distances no effect from trapping

7.5 Summary

centres was observed at the quoted concentrations of table 7.2. At longer charge transit times a deviation from the simple model was observed, which was believed to be the result of increased scattering from the defects since there is more time for the charge cloud to be affected.

At higher charge densities Coulomb interactions cause the charge cloud to

Figure 7.18



The charge collected as a function of detector thickness for the various cases considered (square pixels, pitch is fixed at 100 μm). The term X-ray in the legend corresponds to the generation of 1000 e-h pairs in a volume of 1 μm^3 near the collecting electrode.

be wider than otherwise expected from the model, in agreement with the results of reference [79]. This means that the model of equation 7.1 is too simplistic and that, for the simulation of X- and γ -ray interactions, more advanced modelling is required .

The combination of MCNP and MEDICI allows these physical processes to be modelled in a complete manner - from the interaction processes to the charge transport. The output of these modelling packages has been used to analyse the increasingly more important process of charge sharing. The approximation of an X-ray strike to a point interaction was used as the starting

point to model charge sharing in CdZnTe detectors of varying thicknesses. This method was then developed further to encompass γ -ray interactions, using the example of 662 keV γ -rays incident on 2mm CdZnTe. The optimal pixel size for minimal charge sharing at this energy was observed to be ≈ 1 cm. The various cases are compared for a fixed pixel pitch of $100\ \mu\text{m}$ in figure 7.18. This figure highlights the importance of obtaining ohmic contacts for highly pixellated detectors. Figures 7.13, 7.14 and 7.17 can also be used as an indication of the threshold value in photon counting detectors. For example if a photon counting detector is required to be sensitive to energies of 5 keV (1078 e-h pairs), then for square pixels of pitch $50\ \mu\text{m}$ and a 1mm CdZnTe detection layer with ohmic contacts, only 410 e-h pairs, on average, would be detected. This places a limit upon the overall detector noise to be significantly lower than 400 electrons so that the threshold for counting can be placed at the appropriate point.

Chapter 8

Conclusions and summary

The work in this thesis centred upon the device modelling of semiconductor pixel detectors. The results of these simulations were used to understand experimental results, explore new designs and examine fundamental physical processes. These models were supported experimental results from the Dash-E detector.

The characteristics of this detector were presented in chapter 4 where the electronic noise was measured to have a FWHM of 230 ± 6.6 eV with the system observed to be close to the Fano limit at room temperature. The characteristic X-rays of Mn-55, Cu, Rb, Mo, Ag and Ba were used to examine the spectroscopic performance of the detectors. Good linearity over the required energy range 1 keV to 25 keV was observed. A higher than expected background was evident in all of the spectra taken - approximately a 1:1 correspondence in the peak counts to background counts.

The modelled performance of a 3-D GaAs detector was analysed in chapter 6. The effect of the metallic column-like electrode structure on the particle interactions was simulated via the Monte Carlo code MCNP. The effective

dead area due to these electrodes was reduced from 8 % to 4.5 % due to the secondary particle interactions. The modelled structure became depleted at 50 V with a slight over-depletion of 75 V necessary to minimise the inter-electrode low field regions. The principle benefit of these depletion voltages are that they remain constant for whatever detection thickness that fabrication allows. The charge transport in the devices was also examined, with the damage effects of dry-etching included. A more extensive investigation in to these damage effects was included in appendix D. Full charge collection, in these 3-D GaAs structures, was observed through modelling to be ~ 200 ps in most cases. The effect of reducing the charge carrier lifetime and examining the charge collection efficiency was used to explore how these detectors would respond in a harsh radiation environment. It is predicted that over critical carrier lifetimes (10 ps to 0.1 ns) an improvement of 40 %, over conventional detectors, can be expected. This also has positive implications for fabricating detectors, in this geometry, from materials which might otherwise be considered substandard.

An analysis of charge transport in CdZnTe pixel detectors was also performed. The analysis started with simulation studies into the formation of contacts and their influence on the internal electric field of planar detectors. The models include a number of well known defect states and these are balanced to give an agreement with a typical experimental I-V curve. The charge transport study then extended to the development of a method for studying the effect of charge sharing in highly pixellated detectors. The case of X-ray, as well as higher energy γ -ray, interactions were considered. The charge lost from the 'hit' pixel was studied for these interactions over a range

of pixel sizes ($1\mu\text{m}$ to 10 mm).

Close agreement, with experiment, for the MCNP models was observed and the combination of MCNP and MEDICI produced a complete picture of photon interactions in semiconducting materials. Experimental comparisons also agreed closely with the models, which predicted that the dominant term in the sharing of charge was due to diffusion and that the difference, over photon energy, was due to the energy given to the photoelectron.

The continued development of semiconductor pixel detectors will lead a need for more detector modelling. The recent advances in computer technology have had a significant effect on the simulation of semiconductor devices. Desktop PCs now have the CPU power and memory capabilities to permit advanced modelling programs to run in relatively short periods of time. This will hasten the move to 3-D modelling packages such as ISE [81] and DAVINCI [82]. Detectors such as new CCD designs, monolithic active pixel sensors and the 3-D detectors described here will benefit from this change. The modelling at Glasgow will now focus on 3-D device modelling using ISE and 3-D particle transport using MCNP 4C.

The development of new materials is also continuing with semiconductors such as SiC [83] and GaN being examined for radiation hardness. Materials such as TlBr with high atomic numbers are also being researched for potential application as γ -ray spectrometers [84].

The 3-D detector research has recently been funded as an EU Framework 5 project and detector fabrication is already underway. This 3D-RID (3D Radiation Imaging Detectors) project intends to investigate scintillator filled holes for the detection of X-rays and neutrons, in addition to the structure

detailed here.

The combination of new research tools, new materials, new applications and new detector designs ensures that solid state detector development will continue to be a rapidly expanding field.

Appendix A

Numerical Modelling

The purpose of this appendix is to briefly outline some of the methods used in the models of MCNP and MEDICI.

A.1 The Monte-Carlo method

The Monte Carlo method has its origins in Los Alamos where it was developed during World War II. The invention of this method is attributed to Fermi, von Neumann, Ulam, Metropolis and Richtmyer.

Monte Carlo is ideally suited to solving complex 3-D time dependent problems. Unlike deterministic modelling this method doesn't discretise the spatial domain, and so there is no averaging required in space, energy and time. Particle transport codes use Monte Carlo methods to duplicate a statistical process. This is done by sequentially simulating the individual probabilistic events that comprise a process. The probability distributions of the events are statistically sampled to describe the whole process. Random numbers are selected to determine what type of interaction occurred, where it occurred

and when it occurred. The rules are the physics of the situation, and the available transport data gives the probabilities. Since it is necessary to run a large number of trials to adequately describe the interactions, good computing power is required.

A.2 Finite element modelling

MEDICI is a finite element device modelling package. The primary objective of the software is to solve the partial differential equations represented by Poisson's equation and the continuity equations for electrons and holes. These have been introduced and discussed in chapter 2. For an in depth look at semiconductor device modelling see reference [21].

There are three main steps to be taken for solving these equations by a numerical approach for device modelling :

- The geometry, or domain, of the simulation must be defined and partitioned into a finite number of subdomains. The division of the geometry is to ensure that the solution can be approximated easily with a desired accuracy.
- The differential equations have to be approximated by a series of algebraic equations in each of these subdomains. These algebraic equations involve values, at discrete points within the subdomain, of the continuous dependent variables - where there is a knowledge of the structure of the chosen functions which approximate the dependent variables.
- Obtaining the solution via iterative techniques such as Newton's or Gummel's method.

Appendix B

Semiconductor parameters

Table B.1: Semiconductor parameters for Si, GaAs and CdZnTe

Parameter	Si	GaAs	CdZnTe
Atomic numbers	14	31, 33	48, 30 , 52
Density (g/cm ³)	2.32	5.32	5.78
Energy / electron-hole pair (eV)	3.2	3.64	4.64
Bandgap E_g (eV) at 300 K	1.12	1.424	1.572
Dielectric constant	11.9	13.1	10.9
Affinity (V)	4.05	4.07	4.3
Electron effective mass	0.98	0.067	0.09
Hole effective mass	0.49	0.45	0.65
Electron mobility (cm ² /Vs)	1500	8500	1000
Hole mobility (cm ² /Vs)	450	400	80
Intrinsic resistivity (Ω -cm)	2.3×10^5	10^8	10^{10}

Appendix C

Source information

A variety of sources have been used throughout this work and so the principle decay lines and probabilities are noted here. They are taken from the “Table of Isotopes” 8th edition [100].

Table C.1: Source definition data for Mn

Decay line	Energy (keV)	Intensity (per 100)
K_{α_1}	5.899	18.3
K_{α_2}	5.888	9.3
K_{β_1}	6.490	2.14
K_{β_3}	6.490	1.09

Table C.2: Source definition data for Cu

Decay line	Energy (keV)	Intensity (per 100)
K_{α_1}	8.048	26.0
K_{α_2}	8.028	13.3
K_{β_1}	8.905	3.1
K_{β_3}	8.905	1.59
K_{β_5}	8.977	0.00365

Table C.3: Source definition data for Rb

Decay line	Energy (keV)	Intensity (per 100)
K_{α_1}	13.395	38
K_{α_2}	13.336	19.7
K_{β_1}	14.961	5.39
K_{β_2}	15.185	0.85
K_{β_3}	14.952	2.78
K_{β_5}	15.089	0.0186
K_{β_4}	37.349	0.023
K_{β_5}	36.652	0.1

Table C.4: Source definition data for Mo

Decay line	Energy (keV)	Intensity (per 100)
K_{α_1}	17.479	42.6
K_{α_2}	17.374	22.4
K_{β_1}	19.607	6.61
K_{β_2}	19.965	1.45
K_{β_3}	19.59	3.41
K_{β_4}	19.998	0.0015
K_{β_5}	19.771	0.0341

Table C.5: Source definition data for Ag

Decay line	Energy (keV)	Intensity (per 100)
K_{α_1}	22.163	45.6
K_{α_2}	21.990	24.2
K_{α_3}	21.708	0.001
K_{β_1}	24.943	7.52
K_{β_2}	25.455	1.88
K_{β_3}	24.912	3.9
K_{β_4}	25.511	0.007
K_{β_5}	25.144	0.0547

Table C.6: Source definition data for Ba

Decay line	Energy (keV)	Intensity (per 100)
K_{α_1}	32.194	46.7
K_{α_2}	31.817	25.6
K_{α_3}	31.452	0.00334
K_{β_1}	36.378	8.63
K_{β_2}	37.255	2.73
K_{β_3}	36.304	4.47
K_{β_4}	37.349	0.023
K_{β_5}	36.652	0.1
$O_{12,3}$	37.425	0.4

Appendix D

Simulating electrical transport in dry-etched III-V devices

D.1 Introduction

Dry etching techniques have been used for some time now to fabricate complex patterns on to semiconductor materials. Lateral dimensions as small as 10 nm or less have made it a popular tool in the semiconductor industry. Here it is used to create recessed gate structures, tracks in integrated circuits and to etch active layers in semiconductor lasers, amongst other applications. The advantages that dry etching offers over the alternative wet etches are a high degree of selectivity, excellent anisotropy and good reproducibility. Unfortunately it is often the case that defects arising from the dry etching procedure results in the nanostructures being unsuitable for their application as an electronic device. Dry etch induced damage destroys the periodicity of the lattice thus creating scattering sites whereby reducing the lifetimes and mobilities of the charge carriers. This can adversely effect the charge

collection properties and noise performances of devices such as transistors. In III-V materials the compound nature and the lower melting temperature of the material excludes annealing, which is used to remove damage effects in silicon.

Many models of device behaviour have been simulated by a variety of methods - Monte Carlo [85], drift-diffusion and hydrodynamic [86] and also atomistic [87]. For a review of device modelling see Selberherr [21]. These models do not however encompass electrostatic, electrodynamic and advanced damage profiles into one simulation. The effect of dry etched induced damage on the electrostatics of a device is examined here. We then proceed to analyse the temporal behaviour of these effects in a variety of structures.

In the first section of this work the damage profile from the dry-etching of GaAs has been taken from previously published work [61] and [62] and incorporated into models of a 2-dimensional electron gas (2DEG). The next section details the performance of a high electron mobility transistor (HEMT). This structure has a recessed gate geometry sometimes required for the precision engineering of HEMTs [88].

D.2 Sidewall damage in III-V structures

During the dry-etching of nanostructures two types of damage can occur - sidewall and top surface damage. These are highlighted in figure D.1. The main difference is that surface damage is being continuously removed while sidewall damage is always accumulated. The propagation of crystal defects through the material has been observed experimentally to be over 100 nm for some high energy etch processes [89]. This is significantly higher than the

D.2 Sidewall damage in III-V structures

projected range of ions at these energies ($< 1\text{keV}$), which can be calculated by computer programs such as TRIM and is found to be a few nm at most [90]. It is now believed that the increased depth of the damage is due to channelling of the etching ions along the crystal axes. It was shown by Germann et al [91] that the depth distribution of the induced damage has a strong dependence upon the angle of the incident etching ion beam. Furthermore Stoffel [92] showed through Monte Carlo modelling that channelling in the $< 110 >$ plane is the predominant mechanism due to the large aperture size in this crystal axes. In reference [62] it was shown that the sidewall defect distribution from channelling of the etching ions along the $< 110 >$ crystal planes for III-V materials can be described well by the equations :

$$\begin{aligned} N_D &= N_d(x, y) + N_u(x, y), \\ N_d &= \frac{1}{2} \frac{\alpha_d J_i}{\lambda_c \nu} (\nu\tau - y + x) e^{-x/\lambda} \times \theta(y - x) \theta(x - y + \nu\tau), \\ N_u &= \frac{1}{2} \frac{\alpha_u J_i}{\lambda_c \nu} (\nu\tau - y - x) e^{-x/\lambda} \times \theta(y) \theta(x + y - \nu\tau). \end{aligned} \quad (\text{D.1})$$

where θ is the step function $\theta(y) = 0$ if $y < 0$ and $\theta(y) = 1$ if $y > 0$. Also N_D is the total defect density and comprises the sum of the contributions from the upward (N_u) and downward (N_d) channelling directions. The horizontal distance from the sidewall is x and the distance from the top surface is y . The probabilities of incident ions being scattered into upward or downward channels are α_u and α_d respectively, and both are taken to be 10^{-3} [92]. The bombarding ion flux density, J_i is taken as 10^{14} particles $\text{cm}^{-2}\text{s}^{-1}$ and the mean channelling distance λ_c is 18 nm for a Cl^+ ion with a mean incident energy of 50 eV [61]. These values are consistent with a fairly low damage dry etch process.

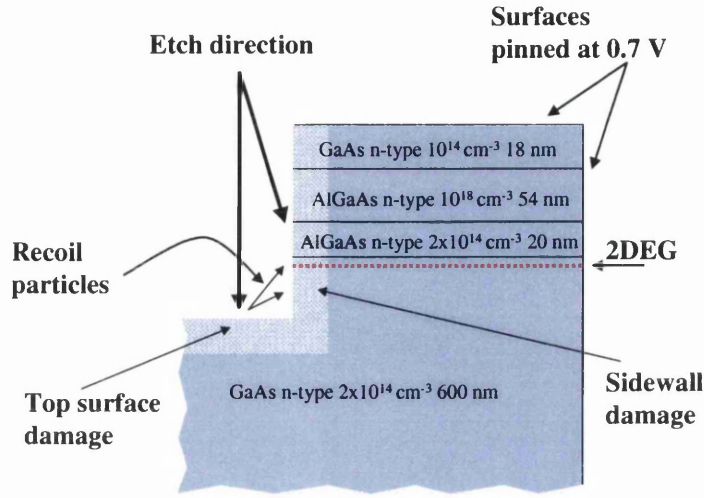


Figure D.1: Modelled 2DEG structure, highlighting the important aspects of the structure.

D.2.1 Model details

In reference [62] a two-dimensional gas (2DEG) of a GaAs/AlGaAs heterostructure was used to experimentally probe sidewall damage as a function of etch time. Furthermore a model was developed and this has been incorporated into the MEDICI simulations reported here. The structure modelled here is an exact representation of the experimental device and is used both to explain some of the experimental observations and examine the accuracy of the model.

The etched 2DEG structure is shown in cross-section in figure D.1. The properties of this structure were modelled using the 2-D simulator MEDICI [15]. The quantum mechanical effects at the 2DEG are approximated by

D.2 Sidewall damage in III-V structures

Van Dort's band-gap widening approach [93]. The screening of the charge carriers, carrier-carrier scattering and acceptor and donor scattering are accounted for by the Philip Unified mobility model [94] and [95]. The AlGaAs layers are taken to have an Al fraction of 0.3 and a band-gap of 1.8 eV.

All exposed surfaces have a Fermi level pinned at 0.7 V by the introduction of interface states, modelled as electron acceptors at a concentration of $3.5 \times 10^{12} \text{ cm}^{-2}$, between the semiconducting material and 0.1 nm of oxide. The etched surfaces contain the additional defect profiles of equation D.1. For modelling purposes the damage is represented by one deep level donor trap, located 0.75 eV below the conduction band. This is assumed to be the predominant recombination centre and is taken from Lootens et al [96] where they associate the trap as the EL2 level from DLTS measurements of SiCl_4 etched n-GaAs. The present and subsequent models account for concentration dependent recombination, Shockley-Read-Hall recombination, Auger recombination and an analytic mobility model which includes concentration dependent mobilities.

The electron concentration across the modelled 2DEG structure is shown in figure D.2. The 2DEG is clearly visible at the AlGaAs GaAs interface. This 2DEG is depleted from the etched sidewall both by surface states and by defects introduced by the etching process. The damage represents the case of a high damage etch so as to ensure any electrical effects are observed.

D.2.2 Damage Profile

The effect of channelling is illustrated graphically in figure D.3. Here the main graph shows the trap density at the 2DEG for an etch of 30 seconds.

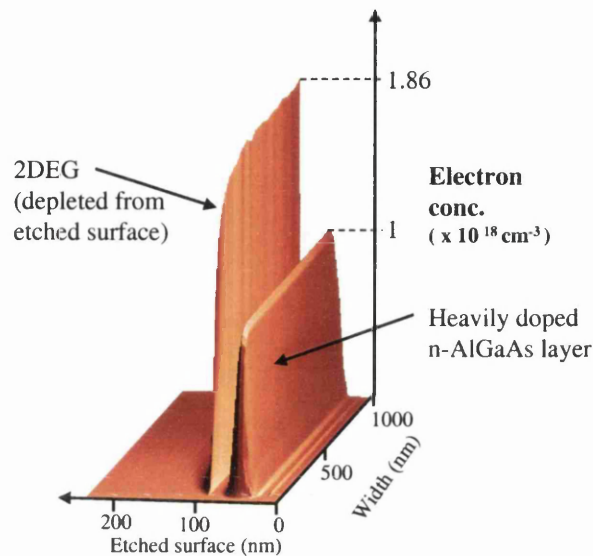


Figure D.2: The electron concentration over a section of the modelled 2DEG. The 2DEG can be seen to be depleted away from the etched surface.

The effects of two distributions are shown - one which incorporates channelling and the other which does not. The shading under the curves illustrates the occupied traps while the inset shows how the depletion depth of the 2DEG is affected by channelling. The damage penetration for the channelling case of around 100 nm agrees well with the experimental data of Chen et al [89].

The traps close to the sidewall are unoccupied since the pinning of the Fermi level at the surface depletes the 2DEG to a significant distance. This shows that the dominant electrostatic effect is due to the surface pinning and not to the damage induced defects. This is supported by the inset which

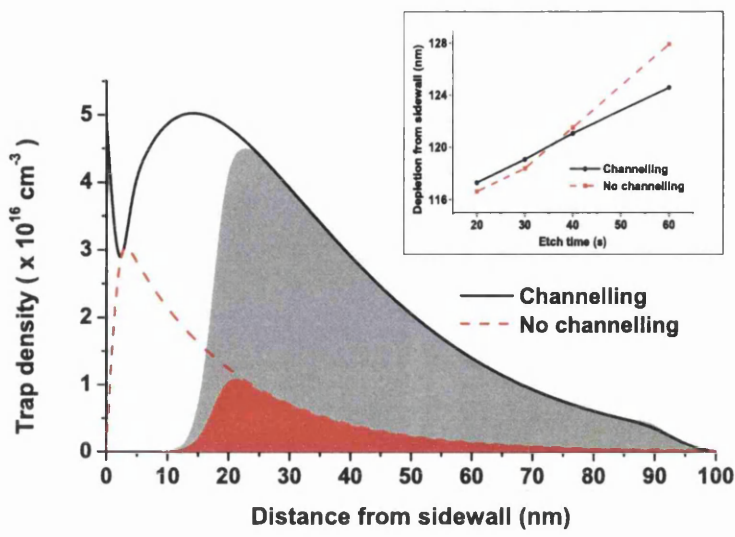


Figure D.3: The trap density as a function of distance from the etched sidewall. The solid curve shows the effect of channelling on the defect profile as a function of distance from the etched sidewall. The light grey shading indicates the filled traps. The dashed curve shows the reduced trap density when channelling effects are neglected. The darker grey shading indicates the filled traps for this no channelling distribution. The inset shows how the depletion distance of the 2DEG from the sidewall for both cases.

shows that the depletion depth varies by only ≈ 10 nm between etch times in the range 10 to 60 seconds (low to high damage). The channelling effect does however lead to a significant increase in the trap density at the 2DEG for an etch depth which is less than that of the 2DEG itself. The excess defects in this relatively high damage etch process have been observed in electron

scattering experiments described in detail in reference [64].

D.3 Gate recessing in HEMTs

High electron mobility transistors exploit 2DEG structures similar to the one already discussed. Here we simulate the output characteristics of a pseudomorphic HEMT, containing elements of strain at the electron conduction layer. HEMT gates are usually recessed to control the threshold characteristics. The recessing is typically done by wet etching, but for greater control may be done by dry-etching methods. The output characteristics of a transistor such as this are obtained experimentally and there is little knowledge of exactly how the defects affect the behaviour, since an etched III-V sample might potentially contain small amounts of damage.

D.3.1 Modelled structure

The structure is shown in figure D.4 along with the material type and doping density. The sidewalls are assumed to be vertical. The source and drain are modelled as ohmic contacts while the gate is a Schottky contact with a work-function of 5.17 V corresponding to a nickel electrode. The $\text{In}_{0.85}\text{Ga}_{0.15}\text{As}$ channel has a band-gap of 0.72 eV. At the $\text{InGaAs}/\text{AlGaAs}$ interface a Si δ -doped layer of concentration $2 \times 10^{12} \text{ cm}^{-2}$ is included. The model is adapted from a simulation detailed in reference [97].

D.3 Gate recessing in HEMTs

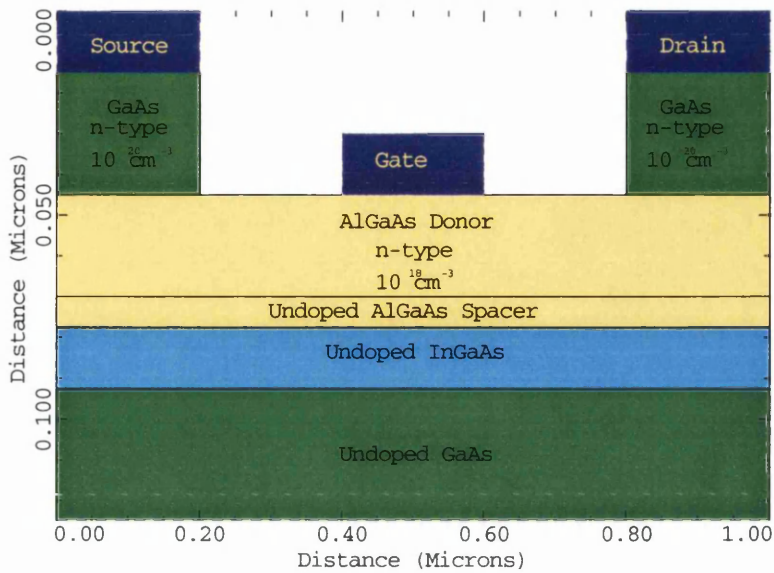


Figure D.4: The modelled HEMT structure.

D.3.2 Damage Profile

In the previous models the top surface damage had no relevance, since the etched surface was either removed completely or etched to such an extent that there was no influence at the sidewalls. Here the top surface damage must be included since charge transport in the channel of the HEMT will be affected by the resultant defects. A precise mathematical expression of this type of damage profile is reported by Ide et al [98] and equation D.2 shows the distribution incorporated into the MEDICI model:

$$N_T(x, y, \tau) = g_0 e^{-x/\lambda} \left(\tau - \frac{y}{\nu} \right), \quad y \leq \nu \tau, \tag{D.2}$$

where all of the variables have been defined previously in subsection D.1. Both the effects of sidewall and top surface damage (which had no bearing on the previous models) are included in this HEMT simulation. The model

includes the channelling effect discussed already. The top surface damage extends into the channel of the device while the sidewall damage will also affect the current flow, from source to gate, forcing the flowlines away from the edges of the recess trench.

D.3.3 Damage effects on gate characteristics

Gate characteristics of transistors offer a convenient way of determining the transconductance of the device - important for applications such as the amplification of signals. The dry-etch damage not only affects the switch on point of the device but also the point of maximum transconductance or amplification. This can be seen in figure D.5 where damage profiles for different times of etch are shown.

The gate voltage was stepped down from 0.6 V to -0.4 V and the drain current was monitored. This was performed for the case where no damage was present and also the cases where damage corresponding to 10, 20 and 30 second etches was included. It can be seen in figure D.5 that the maximum transconductance for the ideal case is at -0.1 V, while this point is at 0.1 V for all three damage cases. The increase in defect density, over these ranges, has a limited effect on further altering the gate characteristics.

D.3.4 Temporal response of HEMT

Another point of importance is how the trapping and later the emission of the charge carriers will affect the temporal performance of the device. These devices are designed to operate at microwave frequencies. If the defects have

D.3 Gate recessing in HEMTs

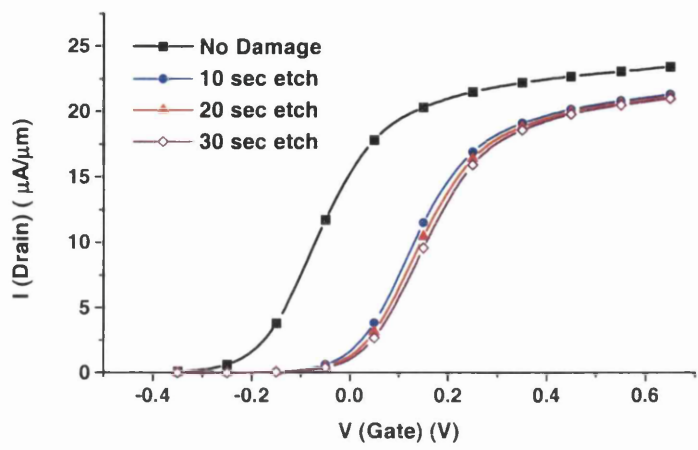


Figure D.5: Modelled gate characteristics of the HEMT illustrating the effect of dry-etch damage.

an effect on these characteristics then this could have implications for many applications.

In order to study these effects the gate voltage was set to the point of maximum transconductance, -0.1 V for the no damage case and 0.1 V for the damage cases. All other voltages were set to zero. The voltage on the drain was then pulsed with 0.5 V for a duration of 0.1 ns. The subsequent decay of the drain current with time was then studied for the various damage profiles. The results can be seen in figure D.6 where only a small effect is noticeable over a time range of 1 ps. All three damage profiles affect the drain current in the same way and the curves lie on top of each other.

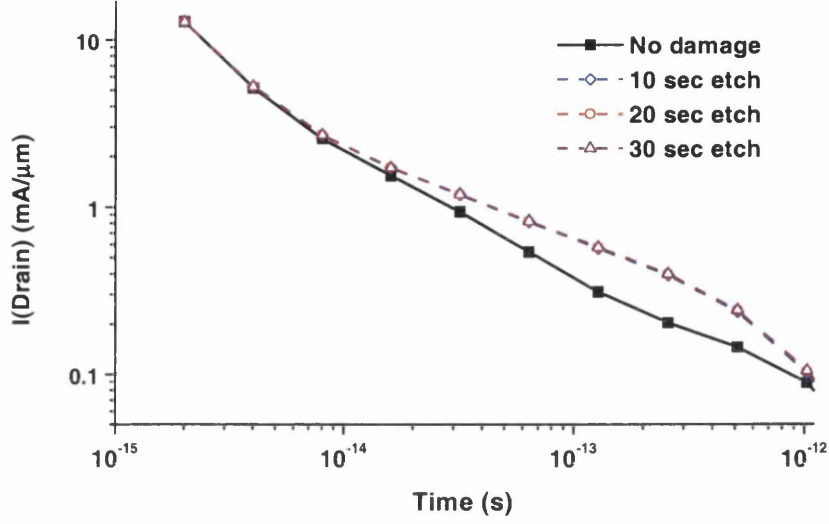


Figure D.6: The time response of the drain current after the drain voltage is pulsed with 0.5 V, for varying etch times. All etch curves lie on top of one another indicating no change in temporal response as a function of etch time.

D.4 Discussion

The effects of dry-etch damage on three III-V structures has been studied. The first structure was chosen to ensure the accuracy of the model, and the second since the long etch times may result in high concentrations of defects at critical points in the device. The final modelled device was chosen since it is a device which is commonly fabricated using dry etch methods, and analysis of device behaviour with damage profiles that include sidewall channelling and top surface damage have not been performed before. The damage profile of references [61] and [62] has been altered for one of these devices and the

D.4 Discussion

effects on each of these structures performance has been analysed. The HEMT structure on the other hand will exhibit an increase in the the turn-on voltage of the drain current. The peak transconductance of the device will also be moved to higher gate voltages. This has been simulated to increase slightly with increasing etch time, which effectively is the defect concentration. The temporal response of this device was also studied though the effects of dry-etch damage was observed to be insignificant over the concentrations studied. These results are consistent with experimental observations of HEMT characteristics at DC and RF frequencies [99].

Appendix E

Trapping and de-trapping in MEDICI

E.0.1 Model

A $75\mu\text{m} \times 75\mu\text{m}$ cross section of n-type GaAs doped with Si to a concentration of $1 \times 10^{14} \text{ cm}^{-3}$ has been simulated with MEDICI. The contacts are on the top and bottom and are both Schottky. The top electrode is held at 500 V with the bottom one earthed. 1000 e-h pairs have been generated at the point (32.5,70) in a volume of $1\mu\text{m}^3$.

E.0.2 Trapping and de-trapping

The trap statement in MEDICI requires the TIME.DEF parameter for the trapping and de-trapping to be modelled correctly. In this simulation a column of traps corresponding to the deep level EL2 have been placed in a row between $y=32.5$ and $y=42.5$. The trap concentration remains unaltered but the lifetimes have been changed from $1 \times 10^{-12}\text{s}$ (the left column) to $1 \times$

10^{-9} s (the right column) - see figure E.1. The decreased lifetime in this area can be seen to stretch out the charge cloud as the trapping and detrapping process takes place. The result will be, for a given shaping time, incomplete charge collection due to the prescence of deep level acceptors. When time dependent traps are modelled an additional differential equation is solved for each trap level. Equation E.1 shows the differential equation for the electron trapping case.

$$\frac{\delta(f_i N_{t_i})}{\delta t} = \frac{(1 - f_i)n - f_i n_{t_i}}{\tau n_i} - \frac{f_i p - (1 - f_i)p_{t_i}}{\tau p_i} \quad (\text{E.1})$$

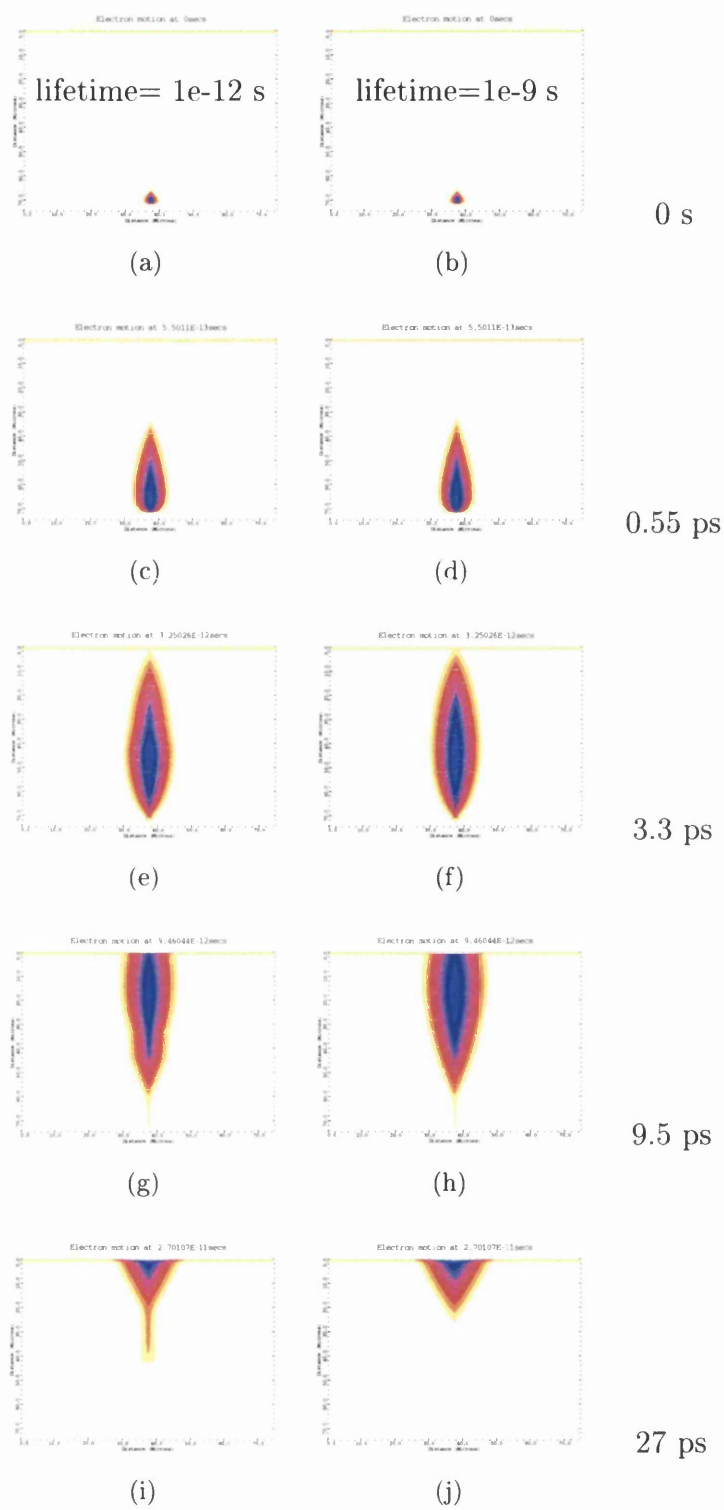


Figure E.1: Time evolution of electron clouds

Bibliography

- [1] Baltic Scientific Instruments, <http://www.bsi.mt.lv>
- [2] C.J.S. Damerell, “Charge-coupled devices as particle tracking detectors”, *Rev. Sci. Instr.*, **69(4)**, (1998) 1549.
- [3] G.K. McKay, *Phys. Rev.* **84**, (1951) 829.
- [4] R. Irsigler et al., “ 320×240 GaAs pixel detector with improved X-ray imaging quality”, *Nucl. Instr. and Meth A* **460(1)**(2001) 67.
- [5] P. Seller et al., “Two approaches to hybrid X-ray pixel array read-out”, *SPIE* **3774**, Detectors for Crystallography and Diffraction Studies at Synchrotron Sources, (1999).
- [6] G. Lindstrom, M. Moll, E. Fretwurst, “Radiation hardness of silicon detectors - A challenge from high energy physics”, *Nucl. Instr. and Meth A* **426**(1999) 1-15.
- [7] J.C. Bourgoin, “A new GaAs material for X-ray imaging”, *Nucl. Instr. and Meth A* **460(1)**(2001) 159-164.
- [8] K. B. Parnham, C. S. Szeles, “Semi-insulating CdZnTe crystals for x-ray and γ -ray detection applications”, *Proc. of the 2nd International*

- Workshop on Radiation Imaging Detectors*, To be published in Nucl. Instr. and Meth A.
- [9] C.J.S. Damerell, "Vertex detectors: The state of the art and future prospects", Rutherford Lab preprint RAL-P-95-008 (1995).
- [10] A.D. Holland, "X-ray spectroscopy using MOS CCDs", *Nucl. Instr. and Meth A* **337**(1996) 334-339.
- [11] C. DaVia, M. Campbell, E.H.M. Heijne, G. Stefanini "Imaging of visible photons using hybrid pixel detectors", *Nucl. Instr. and Meth A* **355**(1995) 414-419.
- [12] T.J. Brodbeck and A. Chilingarov, "Simulation of charge collection and sharing in microstrip detectors", *Nucl. Instr. Meth. A* **395**(1997) 29-34.
- [13] A. Cola et al., "Monte carlo simulation of the induced signal in semi-insulating GaAs", *Appl. Phys. Lett.* **73**(12) (1998) 1709-1711.
- [14] P. Sellin, "Modelling of the small pixel effect in gallium arsenide X-ray imaging detectors", *Nucl. Instr. Meth. A* **434**(1) (1999) 75-81.
- [15] MEDICI, 1998 4.1, AVANT! Corporation
- [16] Los Alamos Monte Carlo Group, "MCNP-B General Monte Carlo N-Particle Transport Code", *Los Alamos National Laboratories report LA-12625-M*, (1997).
- [17] S.M. Sze, "Physics of Semiconductor Devices", *John Wiley and Sons*, New York (1985).

BIBLIOGRAPHY

- [18] R.A. Smith, *Semiconductors*, 2nd ed., Cambridge University Press, London, 1979.
- [19] G. Lutz, "Semiconductor Radiation Detectors : Device Physics", *Springer-Verlag*, Berlin Heidelberg (1999).
- [20] W. Shockley, "Electrons and Holes in Semiconductors", *D. Van Nostrand Co. Inc.*, Princeton, New Jersey (1950).
- [21] S. Selberherr, "Analysis and Simulation of Semiconductor Devices", *Springer-Verlag* New York - Wien (1984).
- [22] G.F Knoll, "Radiation Detection and Measurement", *John Wiley and Sons*, New York (1979).
- [23] R. Fernow, "Introduction to experimental particle physics", *Cambridge University Press*, (1986).
- [24] T. Tabata, P. Andreo, K. Shinoda, "An analytic formula for the extrapolated range of electrons in condensed materials", *Nucl. Instr. and Meth. B* **119**(1996) 463-470.
- [25] H. Grady Hughes, "Treating electron transport in MCNP", Available from <http://www-xdiv.lanl.gov/XCI/PROJECTS/MCNP/doc.html>.
- [26] M.Campbell, E.H.M. Heijne, G. Meddeler, E. Pernigotti, W. Snoeys, "A readout chip for a 64×64 pixel matrix with 15-bit single photon counting", *IEEE Trans. Nucl. Sci.* **45**(3)(1998) 751-753.

- [27] D.S. McGregor, H. Hermon, "Room-temperature compound semiconductor radiation detectors", *Nucl. Instr. and Meth. A* **395**(1997) 101-124.
- [28] J.E. Eberhardt, R.D. Ryan, A.J. Tavendale, "High-resolution nuclear radiation detectors from epitaxial n-GaAs", *Appl. Phys. Lett.* (1970) 427-429.
- [29] T. Kobayashi, T. Sugita, "Gallium Arsenide surface barrier detectors", *Nucl. Instr. and Meth. A* (1972) 179-180.
- [30] K. Hesse, W. Gramann, D. Hoppner, "Room-temperature GaAs gamma-detectors", *Nucl. Instr. and Meth. A* (1972)**101(1)** 39-42.
- [31] S. Manolopoulos et. al., "Developments in GaAs Pixel Detectors for X-ray Imaging", *IEEE Trans. Nucl. Sci.*, **45(3)** (1998).
- [32] S. Manolopoulos et. al., "X-ray powder diffraction with hybrid semiconductor pixel detectors", *J. Synchrotron. Rad.*, **6** (1999).
- [33] J. Watt et. al., "Application of pixellated GaAs X-ray detectors in a synchrotron radiation beam", *Nucl. Instr. and Meth A* **460(1)**(2001) 185-190.
- [34] MEDIPIX collaboration, Information available from <http://medipix.web.cern.ch/MEDIPIX/>
- [35] S. Parker et al., "3D - A proposed new architecture for solid-state radiation detectors", *Nucl. Instr. and Meth A* **395**, (1997) 328-343.

BIBLIOGRAPHY

- [36] R. Bates, “GaAs radiation detectors for the ATLAS experiment” PhD thesis, University of Glasgow, G12 8QQ, Scotland (1997).
- [37] G.M. Martin, J.P. Farges, G. Jacob, J.P. Hallais, G. Poiblaud, “Compensation mechanisms in GaAs”, *J. Appl. Phys.* **51** (5), (1980) 2840-2852.
- [38] D.S. McGregor et. al. “Evidence for field enhanced electron capture by EL2 centers in semi-insulating GaAs and the effect on GaAs radiation detectors”, *J. Appl. Phys.* **75** (12), (1994) 7910-7915.
- [39] K. Berwick, M.R. Brozel, C.M. Buttar, M. Cowperthwaite, Y. Hou, *Mater. Res. Soc. Symp. Proc.* **302** (1993) 363.
- [40] Z. He et al., “Effects of charge sharing in 3-D position sensitive CdZnTe gamma-ray spectrometers”. *Nucl. Instr. Meth. A*, **439**, (2000) 619-624.
- [41] S. Ramo, “Currents induced by electron motion” *Proc. IRE* **27**: **584** (1939) 584.
- [42] M. Martini and G. Ottaviani, “Ramo’s theorem and the energy balance equations in evaluating the current pulse from semiconductor detectors”, *Nucl. Instr. and Meth* **67**(1969) 177-178.
- [43] G. Cavalleri, E. Gatti, G. Fabri, V. Svelto “Extension of Ramo’s theorem as applied to induced charge in semiconductor detectors”, *Nucl. Instr. Meth.* **92** (1971) 137-140.
- [44] O. Tousignant, L.A. Hamel, D. Vasilevski, “Weighting potentials in CdZnTe γ -ray detectors with segmented electrodes”, *IEEE Trans. Nucl. Sci.* **47**(6)(2000) 2084-2086.

- [45] C. Kenney, S. Parker, W. Snoeys, J. Plummer, G. Rosseel, C.H. Aw, "Performance of a monolithic pixel detector" *Nucl. Phys. B Proc. Suppl.* **32** (1993) 460-467.
- [46] IMPACT technical proposal.
- [47] P. Seller et al., "Silicon pixel detector for X-ray spectroscopy", *SPIE* **3445**, EUV, X-ray and Gamma-ray Instrumentation for Astronomy IX, (1998) 584.
- [48] S. Passmore and P. Seller et al., "Performance of an energy resolving X-ray pixel detector", *Proc. of the 5th International Conference on Position-Sensitive Detectors*, To be published in *Nucl. Instr. and Meth A*. (1999).
- [49] L. Evenson et al., "Guard ring design for high voltage operation of silicon detectors", *Nucl. Instr. and Meth A* **337**(1993) 44.
- [50] S. Passmore, "Pixel detectors" PhD thesis, University of Glasgow, G12 8QQ, Scotland (2001).
- [51] A. Owens, G.W. Fraser, A.F. Abbey, A. Holland, K. McCarthy, A. Keay, A. Wells, "The X-ray energy response of Silicon (B): Measurements", *Nucl. Instr. and Meth A* **382**(1996) 503.
- [52] Amersham Technical bulliten 79/3, Americium-241 variable energy X-ray source.
- [53] C. Fröjdh et al., "Performance criteria for X-ray imanging sensors", *Physica Medica* **XIV** (1998).

BIBLIOGRAPHY

- [54] EG&G ORTEC, "Experiments in Nuclear Science", **AN34** (1984) 53.
- [55] C. Kenney et al., "Silicon detectors with 3-D Electrode arrays : Fabrication and Initial test results", *IEEE Trans. Nucl. Sci.*, **46** (4) (1999) 1224-1236.
- [56] A. Meikle et al., "3-D detectors in GaAs", *Presented at 5th Conf. on Position Sensitive Detectors and submitted to Nucl. Instr. and Meth A* (1999).
- [57] F. Roozeboom, R. Elfrink, J. Verhoeven, J. Van den Meerakker, F. Holthuysen *Microelectron. Eng.* **53** (2000) 581.
- [58] M. Rahman et al., "Quantum electron beam probe of sidewall dry-etch damage", *Microelectron. Eng.* **53** (2000) 371.
- [59] J.S. Blakemore, "Semiconducting and Other Major Properties of GaAs", *Journal of Applied Physics*, **53** (10) (1982).
- [60] Eds. T.E Schlesinger, R.B. James "Semiconductors for Room Temperature Nuclear Detector Applications", *Semiconductors and Semimetals*, **43**, (1995) 470-471.
- [61] M. Rahman and K. Mathieson, "Topographic effects in low-energy radiation damage", *Appl. Phys. Lett.*, **77** (9) (2000).
- [62] M. Rahman et al., "Model for conductance in dry-etch damage n-GaAs structures", *Appl. Phys. Lett.*, **61** (1992) 2335.

- [63] A. Owens, M. Bazdaz, S. Kraft, A. Peacock, S. Nenonen, H. Andersson, "The hard X-ray response of epitaxial GaAs detectors", *Nucl. Instr. Meth. A* **442**(1) (2000) 360-363.
- [64] Rahman M 1997 *J. Appl. Phys.* **82** (5) 2215.
- [65] G. Bertuccio, C. Canali, G. De Geronimo, C. Lanzieri, A. Longoni, F. Nava, "Integration of front-end electronics with GaAs pixel detectors: experiment and feasibility analysis", *IEEE Trans, Nucl. Sci.*, **46** (4) (1999) 1209-1214.
- [66] H. Barrett, J. D. Eskin, and H. B. Barber "Charge transport in arrays of semiconductor gamma-ray detectors" *Phys. Rev. Lett.*, **75** (1), (1995) 156-159.
- [67] P.N. Luke, "Unipolar charge sensing with coplanar electrodes - application to semiconductor detectors." *IEEE Trans. Nucl. Sci.* **42** (4) (1995), 207-213.
- [68] V.T. Jordanov, J.A. Pantazis, A.C. Huber, "Compact circuit for pulse rise-time discrimination" *Nucl. Instr. Meth. A*, **380** (1) (1996) 353-357.
- [69] K. B. Parnham and C. Szeles, "Semi-insulating CdZnTe crystals for x-ray and γ -ray detection applications", *Nucl. Instr. Meth. A* submitted for publication.
- [70] A. Burger et al. , "Characterisation of metal contacts on and surfaces of cadmium zinc telluride". *Nucl. Instr. Meth. A*, **428** (1), (1999) 8-13.

BIBLIOGRAPHY

- [71] S. Sen and J. E. Stannard, "Improved quality of bulk II-VI substrates for HgCdTe and HgZnTe epitaxy". *Semiconductors for Room-Temperature Radiation Detector Applications*, **302**,(1993) 391-401.
- [72] M. Hage-Ali and P. Siffert, "Growth methods of CdTe nuclear detector materials". *Semiconductors for Room-Temperature Radiation Detector Applications*, **302**, (1995) 219.
- [73] C. P. Ye and J. H. Chen, "Studies of defects in n-type CdTe by charge transient spectroscopy". *J. Appl. Phys.*, **67** (5),(1990) 2475-2481.
- [74] M. Fiederle et al., "Modified compensation model of CdTe". *J. Appl. Phys.*, **84** (12) (1998) 6689-6692.
- [75] P. Fougères et al. , "CdTe and $\text{Cd}_{1-x}\text{Zn}_x\text{Te}$ for nuclear detectors: facts and fictions". *Nucl. Instr. Meth. A*, **428** (1) (1999) 38-44.
- [76] A. Castaldini et al., "Deep energy levels in CdTe and CdZnTe". *J. Appl. Phys.*, **83** (4) (1998) 2121-2126.
- [77] E. H. Rhoderick and R. H. Williams, "Metal-Semiconductor Contacts". Oxford Science Publications (1988).
- [78] R. F. Fowler et al., "Modelling CCDs for X-ray detectors using three-dimensional semiconductor device modelling software". *Nucl. Instr. Meth. A*, **450** (2000) 75-87.
- [79] R. F. Fowler et al., "Charge spreading from a point source in a depleted diode". RAL report-1998070, available from <http://www.dci.clrc.ac.uk>.

- [80] F. Nava et al., "Evidence for plasma effect on charge collection efficiency in proton irradiated GaAs detectors", *Nucl. Instr. and Meth A* **426**(1999) 185-191.
- [81] ISE - Integrated Systems Engineering, <http://www.ise.ch>.
- [82] Davinci 1998 4.1, AVANT! Corporation.
- [83] T. Dubbs et. al. "Development of radiation-hard materials for microstrip detectors" *IEEE Trans. Nucl. Sci.*, **46 (4)** (1999) 839-843.
- [84] A. Owens, H. Bavdas, I. Lisjutin, A. Peacock, H. Sipila, S. Zatoloka "On the development of compound semiconductor thallium bromide detectors for astrophysics", *Nucl. Instr. Meth. A* **458 (1)** (2001) 413-417.
- [85] Asenov A, Reid D, Barker J R, Cameron N, Beaumont S P *Simulation of Semiconductor Devices and Process*, 5, Eds. S. Selberherr, H. Stippel, and E. Strasser (1993) Springer-Verlag Wien 265.
- [86] Simlinger T, Deutschmann, Fischer C, Kosina H, Selberherr S *4th International Conference on Solid-State and Integrated Circuit Technology. Proceedings (Cat. No.95TH8143)*. IEEE (1995) 589.
- [87] Murthy C S, Posselt M, Feudel T J. *Vac. Sci. Technol. B* **16 (1)** (1998) 440.
- [88] Cameron N I, Murad S, McLelland H, Asenov A, Taylor M R S, Holland M C, Beaumont S P *Electronics Letters* **32 (8)** (1996) 770.

BIBLIOGRAPHY

- [89] Chen C, Green D L, Hu E L *J. Vac. Sci. Technol. B* **13** (6) (1995) 2355.
- [90] Hu E L, Chen C *Microelectron. Eng.* **35** (1997) 23.
- [91] Germann R, Forchel A, Bresch M *J. Vac. Sci. Technol. B* **7** (6) (1989) 1475.
- [92] Stoffel N G *J. Vac. Sci. Technol. B* **10** (2) (1992) 651.
- [93] Van Dort M J, Woerlee P H, Walker A J *Solid-State Electronics* **37** (1994) 411.
- [94] Klaassen D B M *Solid-State Electronics* **35** (1992) 953.
- [95] Klaassen D B M 1 *Solid-State Electronics* **35** (1992) 961.
- [96] Lootens D, Van Daele P, Demeester P, Clauws P *J. Appl. Phys.* **70** (1) (1991) 221.
- [97] Chao P C et al *IEEE Trans. Electron Devices* **36** (3) (1989) 461.
- [98] Ide Y, Takado N, Asakaw K *Gallium Arsenide and Related Compounds*, Ed. Ikoma T and Watanabe H (IOP Bristol 1989) 495.
- [99] Pearson J L, Holland M C, Stanley C R, Long A R, Skuras E, Asenov A, Davies J H *J. Cryst. Growth* **201/202** (1999) 757.
- [100] R.B. Firestone "Table of Isotopes 8th edition" *John Wiley and Sons*, New York (1999).

